ISSN 2186-7968

# ELPH ANNUAL REPORT

2016

TOHOKU UNIVERSITY

Editor

MURAMATSU, Norihito
KIKUNAGA, Hidetoshi
MUTO, Toshiya
TOKIYASU, Atsushi

Research Center for Electron Photon Science

Tohoku University

1-2-1 Mikamine, Taihaku, Sendai 982-0826

Japan

Phone: +81, 22-743-3400

Fax: +81, 22-743-3402

Web site: http://www.lns.tohoku.ac.jp/

982-0826 仙台市太白区三神峯1-2-1

東北大学電子光理学研究センター

電話 022-743-3400

Fax 022-743-3402

# Preface

We are pleased to issue the ELPH Annual Report 2016, which covers scientific and technical activities carried out at Research Center for Electron Photon Science (ELPH), Tohoku University in FY2016 (April, 2016 to March, 2017).

The ELPH has been a part of Joint Usage / Research Centers since FY2011. Joint Usage / Research Centers (JURC) system was engaged by the Ministry of Education, Culture, Sports, Science and Technology (MEXT) to encourage and promote collaborative research passing through the border of respective universities.

This year was the 50th anniversary of the laboratory established in 1966 as former Laboratory for Nuclear Science (LNS). Prof. Motoharu Kimura, the first director of the lab, was moved to Tohoku University from RIKEN around 1950, not much time passed since the World War II was over. At that time, the construction of large scale accelerators had started in USA or USSR, and then a 600 MeV electron linac (MARK-III) was just completed at Stanford University. Japan really laid waste by the war, Prof. Kimura had, however, proposed a new conception of laboratory for nuclear science and related fields to reconstruct Japanese scientific activity. A project of 300 MeV electron linac was approved in 1963, and it was completed in 1967. Nuclear physics using electron beam was activated immediately and solid state physics using neutrons as well. The pulsed neutron experiment employing particle accelerator in the world was initiated at LNS.

The ceremony celebrating 50th anniversary was performed on 17$^{th}$, November 2016. More than 200 former students in alumni and persons concerned got together and confabulated with memories of old days. This fantastic night made us a fresh resolve to open a new era of the laboratory for future human society with the science. We sincerely ask facility users and related scientific field communities for continuous supports and cooperation.

October, 2017
Director
Hiroyuki Hama

# ELPH Annual Report 2016

# Contents

# I. Topics

# The 50th Anniversary of Establishment of Research Center

F. Hinode and N. Muramatsu

*Research Center for Electron Photon Science, Tohoku University, Sendai, Miyagi 982-0826*

The year 2016 marked the 50th anniversary of the establishment of the Laboratory of Nuclear Science (LNS), the predecessor of the Research Center for Electron Photon Science (ELPH), Tohoku University. LNS started in 1966 as a shared facility affiliated to the Graduate School of Science. The 300 MeV LINAC constructed in 1967 provided a pulsed electron beam for the wide research fields of nuclear physics, material science, nuclear chemistry, etc. Simultaneously, the pulsed neutron generation by the high intensity LINAC was started for the first time in the world. This neutron facility leading the pioneering works on the neutron scattering and diffraction experiments had been operated until 1993. In 1981, the world's first pulse-stretcher ring was constructed to stretch the pulsed electron beam from the LINAC. This ring was used for the variety of nuclear experiments with a continuous electron beam, and was succeeded to 1.2 GeV stretcher-booster (STB) ring. Since 2009, LNS has been reorganized to ELPH as an individual research center in Tohoku University. The activities as a Joint Usage / Research Center have begun from 2011. Now tagged photon, electron, and positron beams are available at the 1.3 GeV booster-storage (BST) ring for nuclear / hadron experiments and various detector tests. The high intensity LINAC of 60 MeV electrons can be also operated together with the BST ring for nuclear chemistry and electron scattering experiments. The development of a coherent light source in the THz region has been carried out at the test accelerator facility "t-ACTS" since 2010. Table 1 shows the facility history for the 50 years. On 17 November, 2016, a ceremony was held celebrating the 50th anniversary of the establishment. More than 200 people attended to the ceremony, as shown in Fig. 1. The brief history of the facility including the state of the anniversary ceremony was reported in the reference [1].

## References

[1] F. Hinode, H. Hama, J. Particle Accelerator Society of Japan, Vol. 14, No. 2, (2017), 74 (in Japanese)

Table 1. Facility history for the 50 years

| | |
|---|---|
| 1966 | “Laboratory of Nuclear Science (LNS)” was established. |
| 1967 | 300 MeV Electron LINAC was completed. |
| 1971 | Pulsed neutron source was developed. |
| 1982 | 150 MeV pulse-stretcher ring was completed. |
| 1988 | World’s first observation of coherent radiation was carried out. |
| 1997 | 1.2 GeV Stretcher Booster Ring was completed. |
| 1998 | LNS was reorganized as an attached facility to Faculty of Science. |
| Jul 2002 | “GeV Gamma-ray Irradiation Building” was completed and hadron experiments began. |
| May 2006 | Operation of electron-positron test beam lines began. |
| Sep 2006 | Magnetic spectrometer “NKS2” was completed. |
| Feb 2008 | “Microwave Power Source Building” was completed. |
| Sep 2009 | Electromagnetic calorimeter “FOREST” was completed. |
| Dec 2009 | LNS was reorganized to “Research Center for Electron Photon Science”. |
| Mar 2010 | “Accelerator-based Light Source Building” was completed. |
| Mar 2011 | Operation suspended due to the Great East Japan Earthquake. |
| Apr 2011 | Approved as a Joint Usage/Research Center for Electron Photon Science. |
| Dec 2013 | Operation resumed after recovery from the Great East Japan Earthquake. |
| Jul 2014 | Research building was renovated and the “Mikamine Hall” was completed. |
| Apr 2015 | Collaborative research division “Condensed Matter Nuclear Reaction” was established. |
| 2016 | The 50th anniversary of the establishment. |


Fig.1. The 50th anniversary ceremony held on 17 Nov. (photograph: provided by Public Relations & Outreach Office, Faculty of Science, Tohoku University.)

# Public lecture on the $113^{th}$ element " Nihonium "

Toshimi Suda

*Research Center for Electron Photon Science, Tohoku University, Sendai, Miyagi 982-0826*

On December 10, 2016, a public lecture on the newly discovered $113^{th}$ element Nihonium was held at Multidisciplinary Research Building in the Kawauchi campus, Tohoku University. This lecture was the first one of "Public Science Lecture Series" newly established by Graduate School of Science, Tohoku University [1]. Since Professors T. Suda and H. Kikunaga of the Research Center for Electron Photon Science (ELPH) contributed to the discovery, ELPH hosted this event to make this scientific achievement widely known.

This public lecture was quite timely since it was right after an official announcement by IUPAC (International Pure and Applied Chemistry Association) [2], dated November 30, 2016, on the approval the name and symbol for the $113^{th}$ element to be "Nihonium" and "Nh", respectively. This historical event was taken up largely in the press; much public attention has been attracted.

Although the day of the public lecture was unfortunately very cold snowy day, there were more than 150 participants, including students of elementary to high schools, from not only Sendai area but also Aomori, Akita, Yamagata and Ibaraki prefectures.

The program was started by an introductory lecture on heavy elements such as Nihonium by Professor K. Hagino, Tohoku University, followed by the main lecture by Professor K. Morimoto, RIKEN, who was the main player of this achievement. He explained exciting stories about the discovery of the $113^{th}$ element Nihonium, and the participants were very enthusiastically listening to his talk. After each lecture, there were many questions from the participants, which clearly showed that everyone had very high interest. We were very happy that this public lecture was so successful.

## References

[1] http://www.sci.tohoku.ac.jp/mediaoffice/20161213-8808.html (in Japanese)

[2] https://iupac.org/iupac-announces-the-names-of-the-elements-113-115-117-and-118/


Fig.1. Event Poster

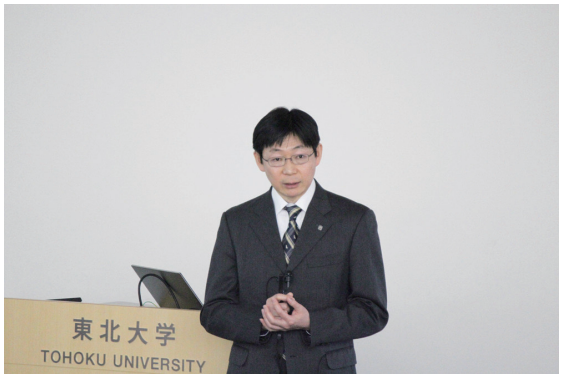


Fig.2. Professor K. Morimoto

# II. Papers

(ELPH Experiment : #2623, #2640, #2655, #2694, #2710)

# Study of the $I = 0$ dibaryon resonance $d^*(2380)$ via the $\gamma d \to \pi^0\pi^0 d$ reaction at incident energies below 0.9 GeV

T. Ishikawa[1], H. Fujimura[1], H. Fukasawa[1], R. Hashimoto[1], Q. He[1], Y. Honda[1], T. Iwata[2], S. Kaida[1], H. Kanda[3], J. Kasagi[1], A. Kawano[4], S. Kuwasaki[1], K. Maeda[3], S. Masumoto[5], M. Miyabe[1], F. Miyahara[1], K. Mochizuki[1], N. Muramatsu[1], A. Nakamura[1], K. Nawa[1], S. Ogushi[1], Y. Okada[1], K. Okamura[1], Y. Onodera[1], K. Ozawa[6], Y. Sakamoto[4], M. Sato[1], H. Shimizu[1], H. Sugai[1], K. Suzuki[1], Y. Tajima[2], Y. Taniguchi[1], Y. Tsuchikawa[1], H. Yamazaki[1], R. Yamazaki[1], and H.Y. Yoshida[2]

[1]*Research Center for Electron Photon Science (ELPH), Tohoku University, Sendai 982-0826, Japan*
[2]*Department of Physics, Yamagata University, Yamagata 990-8560, Japan*
[3]*Department of Physics, Tohoku University, Sendai 980-8578, Japan*
[4]*Department of Information Science, Tohoku Gakuin University, Sendai 981-3193, Japan*
[5]*Department of Physics, University of Tokyo, Tokyo 113-0033, Japan*
[6]*Institute of Particle and Nuclear Studies, High Energy Accelerator Research Organization (KEK), Tsukuba 305-0801, Japan*

The total cross section was measured for the $\gamma d \to \pi^0\pi^0 d$ reaction at incident energies below 0.92 GeV for the first time using the FOREST detector at ELPH. No clear resonance-like behavior was observed in the excitation function for $W_{\gamma d} = 2.38$–$2.61$ GeV, where the $d^*(2380)$ dibaryon resonance observed at CELSIUS and COSY was expected to appear. The measured excitation function was consistent with the existing theoretical calculation. The upper limit of the total cross section was found to be 0.034 $\mu$b for the dibaryon resonance at $W_{\gamma d} = 2.37$ GeV (90% confidence level). The details are described in a published paper: T. Ishikawa *et al.*, Phys. Lett. B **772**, 398 (2017).

## §1. Introduction

The search for non-strange dibaryon bound/resonance states has a long history. The dibaryon state is of interest, which can be a molecule consisting of two baryons or a spatially compact hexaquark object. The $d^*(2380)$ resonance observed in the $pn$-collision reactions by the CELESIUS/WASA and WASA-at-COSY collaborations [1, 2] may be attributed to an isoscalar $\Delta\Delta$ quasi-bound state $\mathcal{D}_{03}$, predicted by Dyson and Xuong [3]. The $s$-channel photoproduction $\gamma d \to \pi^+\pi^- d$ and $\gamma d \to \pi^0\pi^0 d$ reactions are expected to be of value to get a clue for the size of the $d^*(2380)$ resonance. The $\gamma d \to \pi^+\pi^- d$ reaction was studied by the JLAB/CLAS collaboration, and their preliminary result does not show a peak corresponding to the $d^*(2380)$ resonance [4]. We investigated the other $\gamma d \to \pi^0\pi^0 d$ reaction to study photoproduction of the $d^*(2380)$ resonance.

## §2. Summary

The $\gamma d \to \pi^0\pi^0 d$ reaction was experimentally investigated at the Research Center for Electron Photon Science (ELPH), Tohoku University, Japan. The incident photon beam ranged from from 0.57 to 0.88 GeV **??**. The $\gamma d$ center of mass energy $W_{\gamma d}$ corresponding the incident energy was covered from 2.38 to 2.61 GeV. The the target used in the experiments was 45.9-mm-thick liquid deuterium. The kinetic variables for all the final-state particles ($\gamma\gamma\gamma\gamma d$) were measured using the FOREST detector [7]. A kinematic fit with six constraints was applied for the event selection of the $\gamma d \to \pi^0\pi^0 d$ reaction. The required constraints were energy and three-momentum conservation between the initial and final states and two $\gamma\gamma$ invariant masses (the neutral-pion mass). Events in which the $\chi^2$ probability is higher than 0.4 are selected to prevent contamination from the background processes. Fig. 1 shows the total cross section $\sigma$ as a function of $W_{\gamma d}$. No clear resonance-like behavior was observed in the excitation function near $W_{\gamma d} = 2.38$ GeV, where the $d^*(2380)$ dibaryon resonance was expected to appear. The measured excitation function was consistent with the existing theoretical calculation for this reaction [8]. The details of the explanations and discussions are described in Ref. [9].

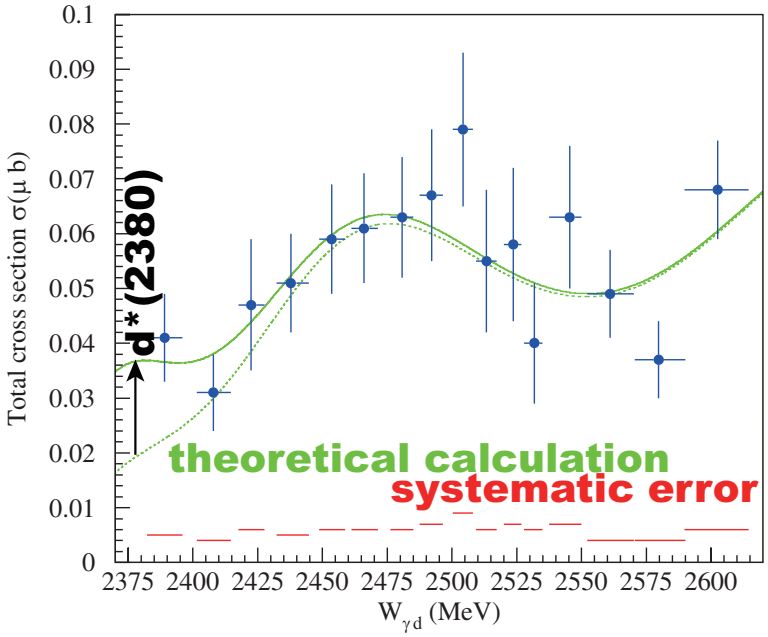


Fig.1. Total cross section $\sigma$ as a function of $W_{\gamma d}$ together with the theoretical calculation by Fix and Arenhövel [8].

## Acknowledgments

The authors express their gratitude to the ELPH accelerator staff for stable operation of the accelerators in the FOREST experiments. They also acknowledge Mr. K. Matsuda, Mr. K. Nanbu, and Mr. I. Nagasawa for their technical support. One of the authors (TI) thanks Prof. H. Clement and Dr. M. Bashkanov for fruitful discussions for event selection including the deuteron identification. This work was supported in part by the Ministry of Education, Culture, Sports, Science and Technology,

Japan through Grants-in-Aid for Scientific Research (B) No. 17340063, for Specially Promoted Research No. 19002003, for Scientific Research (A) No. 24244022, for Scientific Research (C) No. 26400287, and for Scientific Research (A) No. 16H02188.

## References

[1] M. Bashkanov *et al.* (CELSIUS/WASA collaboration): Phys. Rev. Lett. **102**, 052301 (2009).

[2] P. Adlarson *et al.* (WASA-at-COSY collaboration): Phys. Rev. Lett. **106**, 242302 (2011).

[3] F.J. Dyson and N.-H. Xuong: Phys. Rev. Lett. **13**, 815 (1964).

[4] R.A. Schumacher: talk at Meson in Nucleus 2016 (MIN16) (2016);
MIN16 website: ⟨http://www2.yukawa.kyoto-u.ac.jp/~min2016/⟩.

[5] T. Ishikawa *et al.*, Nucl. Instrum. Meth. A **622**, 1 (2010)

[6] T. Ishikawa *et al.*, Nucl. Instrum. Meth. A **811**, 124 (2016).

[7] T. Ishikawa *et al.*, Nucl. Instrum. Meth. A **832**, 108 (2016).

[8] A. Fix, H. Arenhövel: Eur. Phy. J. A **25** ,115 (2005).

[9] T. Ishikawa *et al.*: Phys. Lett. B **772**, 398 (2017).

(ELPH Experiment : #2761)

# Development of Electro-magnetic Calorimeter with Active Absorbers

Y.Fujita, Y. Hasegawa, H. Itoh, I.Kanzaki, K.Kotera, E. Naiki, H.Sato, T.Takeshita, and Y.Yamashita

Faculty of Science, Shinshu University, Matsumoto, Japan

An electro-magnetic calorimeter dedicated to measure the incident position and angle with active absorber is developed and tested with electron beams. The calorimeter consists of active absorber made of lead glass and scintillator strips with wave length shifting fibers is constructed. We tested its performance to the electrons at ELPH beam at Tohoku University. The performance and the results are presented.

## §1. Introduction

We are developing a fully active electromagnetic (EM) calorimeter at low energy, which consists of sandwich calorimeter of active absorber and fine segmented sensitive scintillator. The calorimeter could measure the photon and electron energy with as good as the lead glass calorimeter, say 5% of over square root E. Furthermore it can measure the incident angle of photon and electron with good position resolution. Such an EM calorimeter could be applied for many experiments with both energy resolution and position/angle resolutions are mandatory. The performances have been verified with the electron beam at ELPH, Tohoku University.

## §2. EM calorimeter and experimental setup

The active absorber EM calorimeter has been introduced in order to improve both energy resolution and position/angle resolution for photons. The calorimeter detector system is shown in Figure 1.

It is composed of sandwich structure of the lead glass absorber layer as an active heavy material and fine segmented scintillator strip layer [1]. The size of a lead glass block is $3\times3\times4$ cm$^3$ and read out the Cherenkov light by a MPPC of $3\times3$ mm$^2$ [2]. The lead glass unit has been tested by muons and resulted about 10 photo-electrons (p.e.) / 4 cm passing a lead glass block. We prepared there lead glass layers, each consist of $3\times3$ blocks. There are three scintillator strip layers of X-Y configuration with nine strips behind the lead glass layers. We set a large lead glass of $12\times12\times25$ cm$^3$ for a tail catcher. A long scintillator strip of 1 cm × 18 cm has been employed for the strip layer with WLSF (Wave Length Shifting Fiber) read out by a MPPC of $1\times1$ mm$^2$. The tail catcher has been read out by a $12\times12$ mm$^2$ MPPC. There is a pair of crossing trigger scintillator strips in front of the detector to define the beam timing which are also read by MPPCs.

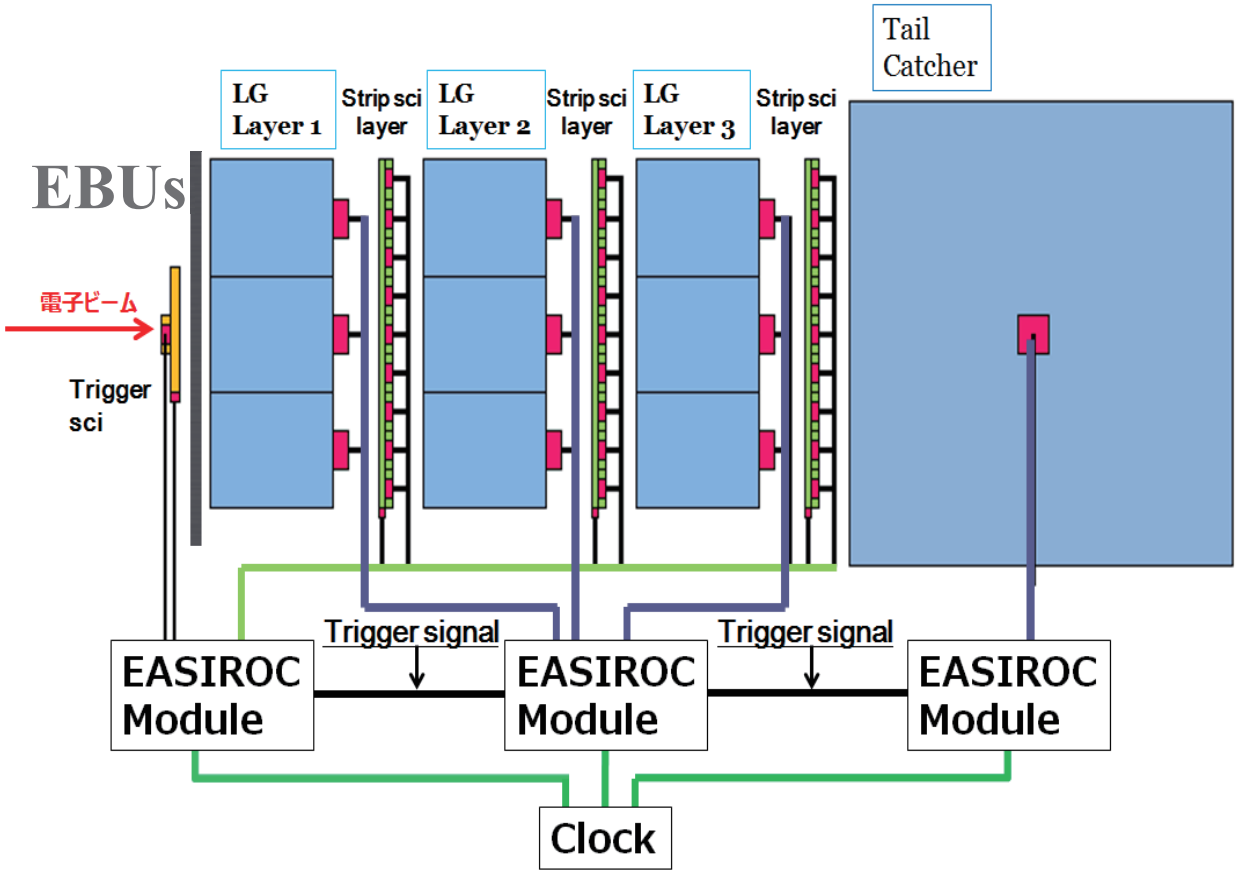


Figure 1: Schematic view of the active absorber EM calorimeter and its setup at ELPH electron beam. From left to right, trigger counters, three layers of lead glass active absorber and scintillator strip and a tail catcher. Each units had been attached a photo-sensor MPPC and read by EASIROC modules.

All the signals from MPPCs in total 83 channels are read by three EASIROC modules which had been developed for the MPPC read out through the ether-net [3].

## §3. Results

Here we show some results of the active absorber calorimeter tested at ELPH 2016.

(1) The EM shower position distributions are shown in Figure 2-a, with taking information from the scintillator strip layers and without it. Slight improvement to the position resolution is seen from 15 mm to 13 mm.

(2) The angle resolutions are shown in Figure 2-b with taking information from the scintillator strip layers and without it. The incident beam angles were changed from 0 to 5 degree. Slight improvement is seen from 9 degree to 8 degree.

Further analysis is going on.

## §4. Conclusion

A sandwich type EM calorimeter has been constructed and tested. A new feature for the detector is using active absorber with segmentation. The improvements for measurements of the EM shower position and angle were verified.

## Acknowledgement

The authors thank the ELPH accelerator staff for providing the primary electron beam with good quality. They are grateful to M. Miyabe for his technical support in preparation for the measurements.

## References

[1] SF6W lead glass employed at TOPAZ , Kawabata et. al. NIM A 270(1988) 11.

[2] MPPC trade mark of Hamamatsu Photonics CO.

[3] A master thesis by Naoki Ishijima, Osaka University, 2014.

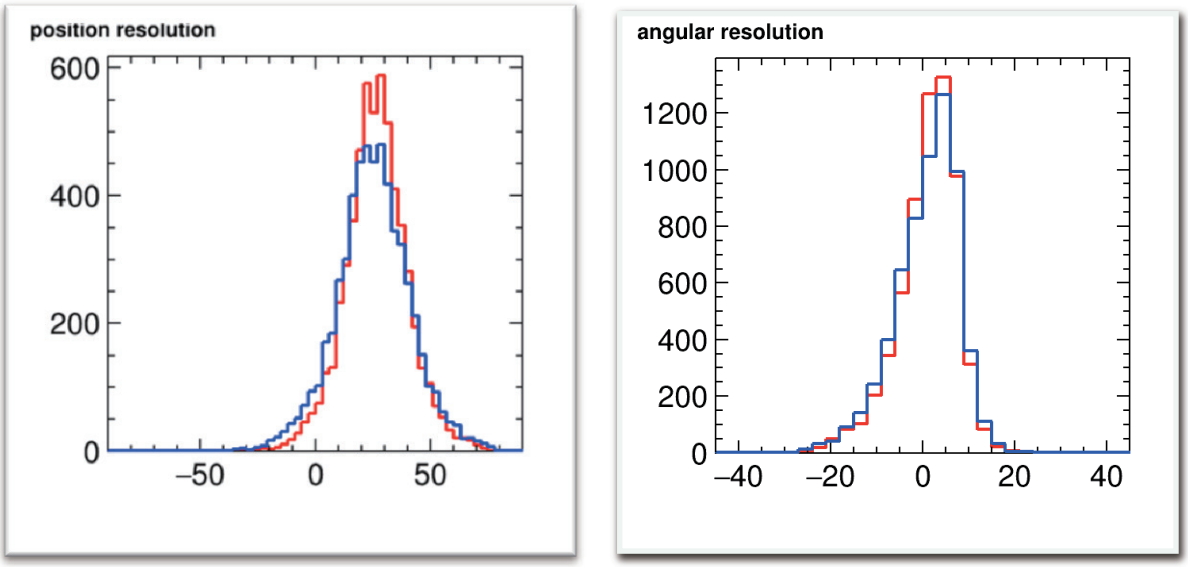


Figure 2-a (left) and Figure 2-b (right): Figure 2-a shows the EM shower position measurement with (red line) and without (blue line) strip information, where energy weighted mean of EM showers are considered. Figure 2-b shows the incident angle distribution measured with (red line) and without (blue line) strip information, where linear fitting of all position information were taken into account.

(ELPH Experiment : #2803, #2844)

# Current status of preparing the new FOREST experiments at ELPH

T. Ishikawa[1], K. Aoki[2], H. Fujioka[3], Y. Honda[1], T. Hotta[4], Y. Inoue[1], K. Itahashi[5], H. Kanda[4], H. Kawai[6], K. Maeda[7], Y. Matsumura[1], M. Miyabe[1], S. Miyata[8], N. Muramatsu[1], T. Nishi[5], H. Ohnishi[1], K. Ozawa[2], M. Sasagawa[1], H. Shimizu[1], R. Shirai[1], M. Tabata[6], A.O. Tokiyasu[1], Y. Tsuchikawa[9], and H. Yamazaki[1]

[1]*Research Center for Electron Photon Science (ELPH), Tohoku University, Sendai 982-0826, Japan*
[2]*Institute of Particle and Nuclear Studies, High Energy Accelerator Research Organization (KEK), Tsukuba 305-0801, Japan*
[3]*Department of Physics, Kyoto University, Kyoto 606-8502, Japan*
[4]*Research Center for Nuclear Physics (RCNP), Osaka University, Ibaraki 567-0047, Japan*
[5]*Nishina Center for Accelerator-Based Science, RIKEN, Wako 351-0198, Japan*
[6]*Department of Physics, Chiba University, Chiba 263-8522, Japan*
[7]*Department of Physics, Tohoku University, Sendai 980-8578, Japan*
[8]*Department of Physics, University of Tokyo, Tokyo 113-0033, Japan*
[9]*Department of Physics, Nagoya University, Nagoya 464-8602, Japan*

The next-generation FOREST experiments are planed to reveal the non-perturbative QCD phenomena. The main objective of the first experiment is to determine low-energy $S$-wave $\eta n$ scattering parameters using the $\gamma d \to p\eta n$ reaction. The photon beam with energies around 940 MeV can give the recoilless condition of $\eta$ mesons by detecting the protons at 0°. The effects of the the final-state $\eta n$ interaction must be enhanced due to the small relative momentum between the $\eta$ meson and the residual neutron. We placed a bending magnet, which was transported from KEK, behind the FOREST detector to measure the forward emitted protons. The $\Lambda n$ interaction can be studied using the $\gamma d \to K^+\Lambda n$ reaction detecting the $K^+$ mesons at 0° in the same experimental setup. And the similar experimental setup can be used for an experiment to search for $\eta$-mesic nuclei, which are good probes to explore the properties of a nucleon resonance $N(1535)S_{11}$ in the nuclear medium. It should be noted that the resonance is speculated to be the chiral partner of the nucleon.

We succeeded the excitation and ARCNET control of the bending magnet BLC for the forward spectrometer using the dedicated power supply QC1LE. The performance tests of the new detectors, two drift chambers, plastic-scintillator hodoscope, and SF5 lead-glass Cherenkov counters, for the forward spectrometer were made using the positron beams for testing detectors at ELPH. Commissioning of the forward spectrometer with these detectors was successfully made using the liquid hydrogen target from May 22 to May 31 in 2017. In this report, the preparation for the new FOREST experiment is presented.

## §1. Introduction

The interaction between hadrons is fundamental and important in the non-perturbative domain of quantum chromodynamics (QCD), which is the fundamental theory of the strong interaction. Although the interaction between hadrons is described in principle by quark and gluon dynamics, little is known for the QCD solutions due to the large running QCD coupling constant at low energies.

Among the two-body dynamics of hadron-hadron systems, the interaction between the $\eta$ meson and nucleon ($N$) is not well known [1] although the interaction is found to be attractive. This is because neither direct $\eta N$ scattering experiments nor $X$-ray measurements from $\eta$-mesic atoms can be performed due to the neutral and unstable nature of the $\eta$ meson. The low-energy $\eta N$ interaction is described using the scattering length $a_{\eta N}$ and effective range $r_{\eta N}$ in an effective-range expansion of the $S$-wave phase shift:

$$k \cot \delta(k) = \frac{1}{a_{\eta N}} + \frac{1}{2} r_{\eta N} k^2 + O(k^4). \tag{1}$$

It should be noted that positive and negative $a_{\eta N}$ values correspond to attractive and repulsive $\eta N$ interactions in this definition, respectively.

Although the imaginary part of $a_{\eta N}$ (Im$[a_{\eta N}]$) is found to be $\sim 0.26$ fm for different analyses, its real part (Re$[a_{\eta N}]$) is scattered in a wide range from 0.2 to 1.1 fm [2, 3]. Fig. 1 shows the summary of the obtained imaginary and real parts of $a_{\eta N}$ taken from Ref. [1]. The Re$[a_{\eta N}]$ value is important and sensitive to the pole position of the $N(1535)S_{11}$ resonance [4]. It is the lowest excited state of the nucleon with a spin of $1/2$ and negative parity, and speculated to be the chiral partner of the nucleon. The pole is known to be near the $\eta N$ threshold but its accurate position is still uncertain. The Re$[a_{\eta N}]$ value also affects the existence of exotic $\eta$-mesic nuclei [1], which reveal the properties of $N(1535)S_{11}$ in the nuclear medium since it strongly couples to $\eta N$. In addition, the Re$[a_{\eta N}]$ value is also related to the $\eta$-$\eta'$ mixing angle [5].

In many theoretical papers, the $a_{\eta N}$ values have been extracted using a combined analysis from the differential and total cross sections for the $\pi N \to \eta N$ transition and $\gamma N \to \eta N$ photoproduction reactions together with $\pi N \to \pi N$ scattering and $\gamma N \to \pi N$ photoproduction reactions. As a consequence of the optical theorem, similar Im$[a_{\eta N}]$ values have been obtained in the analyses. A large ambiguity exists in the determination of the Re$[a_{\eta N}]$ value because the reactions used in the $a_{\eta N}$ analyses do not enhance the effect of the $\eta N \to \eta N$ scattering amplitude so far. Thus we propose the $\gamma d \to \eta pn$ reaction to determine $a_{\eta N}$ at a certain kinematics, which enhances the $\eta N$ scattering effect.

A possibility of the precise determination of $a_{\eta N}$ from the $\gamma d \to \eta pn$ reaction was first investigated by Sibiritsev *et al.* [8] and followed by Fix and Arenhövel [9]. The opposite conclusions for the resolving power of the Re$[a_{\eta N}]$ value from the experimental data are shown in these works. However, the kinematics in these pioneering works is near the threshold ($E_\gamma < 0.7$ GeV). The contribution from the first-order $\eta N$ rescattering are not well-separated from the others. We will show the ideal condition to extract $a_{\eta N}$ from the $\gamma d \to \eta pn$ reaction in the next section.

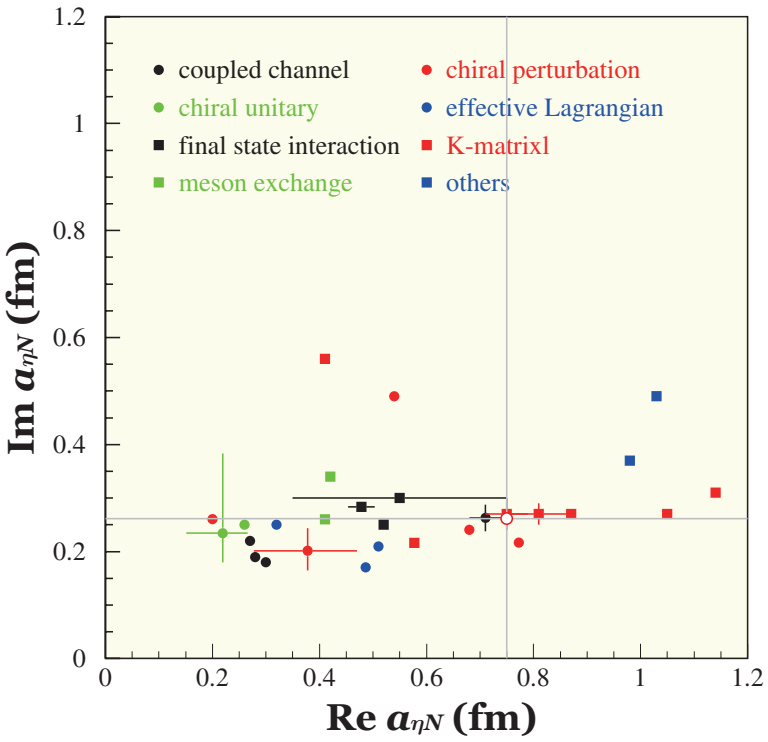


Fig.1. Imaginary and real parts of the $\eta N$ scattering length $a_{\eta N}$ [1]. The different markers indicate the different methods to provide the values. All the analyses seem to have a small effect of the $\eta N \to \eta N$ scattering amplitude.The open circle (red) represent the result from the dynamical coupled-channels analysis [6, 7].

## §2. Proposed $\gamma d \to p\eta n$ reaction

To determine $a_{\eta N}$, we plan to measure the differential cross sections for the $\gamma d \to p\eta n$ reaction [10] at the Research Center for Electron Photon Science (ELPH), Tohoku University, using the photon beam with energies around 0.94 GeV [11, 12] and detecting the protons at 0°. The bremsstrahlung photon beam at ELPH covers the energies from 0.82 to 1.26 GeV. Fig. 2 shows the expected diagram of the proposed reaction. The incident photon bombards the proton in the deuteron and produces a (virtual) $\eta$ meson with a very low momentum. The scattered proton from the reaction is detected at 0° having a large momentum close to that of the photon beam. At this kinematics, an $\eta$ meson is likely to be produced almost at rest with respect to the residual neutron, being expected to strongly interact with it. The forward-going proton has a large momentum, and little chance to interact with $\eta$ or neutron. The characteristics of this diagram are discussed below.

We will select the events in which the incident energy is approximately 0.94 GeV and the proton (with a momentum around 0.94 GeV/$c$) is detected at 0°. This kinematics satisfies the recoilless condition of the produced $\eta$ mesons. Fig. 3 shows the recoil momentum of $\eta$ mesons for the elementary $\gamma p \to \eta p$ reaction for the free proton target. The incident photon energy of 0.932 GeV can produce $\eta$ mesons at rest in the laboratory frame. The ideal low-energy $\eta n$ scattering is expected to take place at the incident photon energy around 0.94 GeV taking into account the binding energy of the deuteron.

The forward proton has a very large momentum, and the relative momentum between the proton

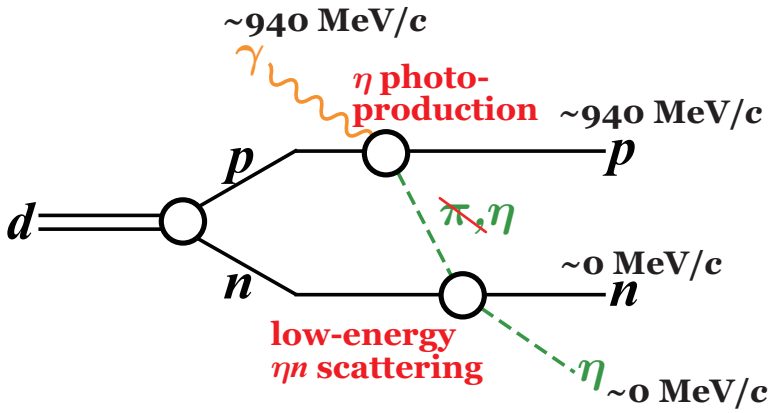


Fig.2. Expected diagram for the $\gamma d \to p\eta n$ reaction at the incident photon energy of 0.94 GeV and with the proton detection at 0°. The photon bombards the proton in the deuteron and produces an $\eta$ meson with a very low momentum. The ideal low-energy $\eta n$ scattering takes place where the $pn$ and $\eta p$ rescattering effects are suppressed due to their large relative momenta.

and residual neutron is also very large ($\sim 0.94$ GeV/$c$). This large relative momentum gives little chance to the interaction between the proton and residual neutron. The relative momentum between the proton and $\eta$ meson is also very large ($\sim 0.94$ GeV/$c$), leaving little chance to the interaction between the proton and produced $\eta$ meson. Thus the $pn$ and $\eta p$ rescattering effects are thought to be suppressed.

The candidates of the exchange particle are $\pi$ and $\eta$ mesons in view of quantum numbers. The mass of the exchange particle is close to the rest mass of the $\eta$ meson make the $\eta$ exchange enhanced together with the condition that the $\eta$ meson almost at rest is detected in the final state.

The sensitivity to $\eta n$ scattering length of the proposed reaction has been checked [13] using the dynamical coupled-channels (DCC) model [6, 7]. The DCC model solves the coupled-channel Lippmann-Schwinger equation for meson-baryon scattering, where the coupled-channel unitarity, on- and off-shell amplitudes are fully considered. The DCC model itself gives

$$\begin{cases} a_{\eta N} = +0.75 + i0.26 \text{ fm, and} \\ r_{\eta N} = -1.6 + i0.6 \text{ fm} \end{cases} \tag{2}$$

for the low-energy scattering parameters. The corresponding points are also presented in Fig. 1. Four kinds of diagrams as shown in Fig. 4 are taken into account in the treatment of the $\gamma d \to \eta pn$ reaction. Here, the $\gamma N \to \pi N$, $\gamma N \to \eta N$, and $\pi N \to \eta N$ amplitudes are given by the DCC model, and the amplitude for the $pn$ final-state interaction (FSI) and deuteron wave function are provided by the CD-Bonn [14], Nijmegen I [15], and Reid93 [15] potentials. The differential cross section $d\sigma/dM_{\eta n}/d\Omega$ are calculated as a function of the $\eta n$ invariant mass ($M_{\eta n}$). The contribution of each term shown in Fig. 4 can be obtained turning off the corresponding amplitude. The results of the calculation show

1. $\eta n$ rescattering effect is visible at the small $\eta n$ relative momentum (enhancement factor $\sim 1.2$),
2. $\pi n \to \eta n$ transition ($\pi$ exchange) effect is small, and
3. $pn$ rescattering effect is also small.

The $d\sigma/dM_{\eta n}/d\Omega$ values are calculated for different sets of Re$[a_{\eta n}]$, and sensitivity of Re$[a_{\eta n}]$ is

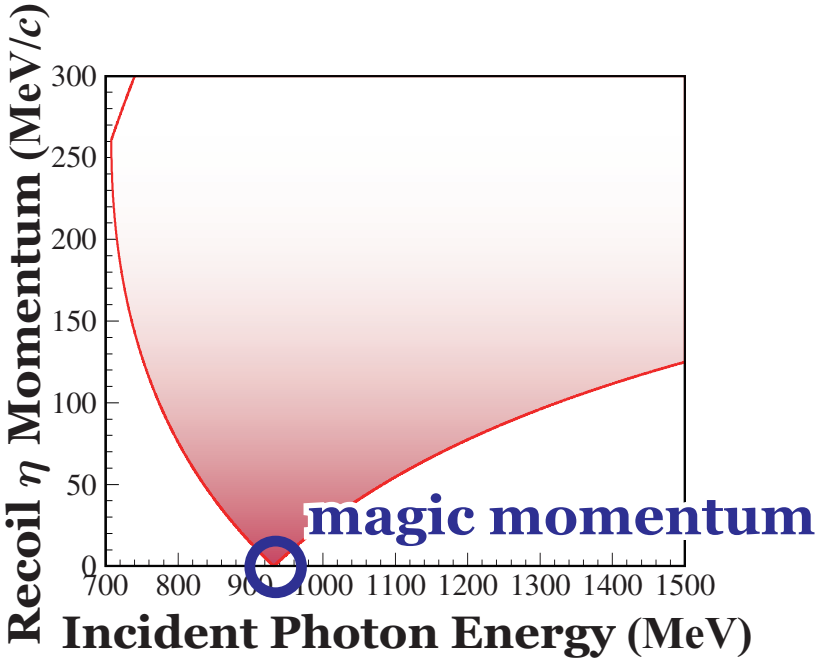


Fig.3. Recoil momentum of $\eta$ mesons for the $\gamma p \to \eta p$ reaction for the free proton target. The incident photon energy of 0.932 GeV can produce $\eta$ mesons at rest.

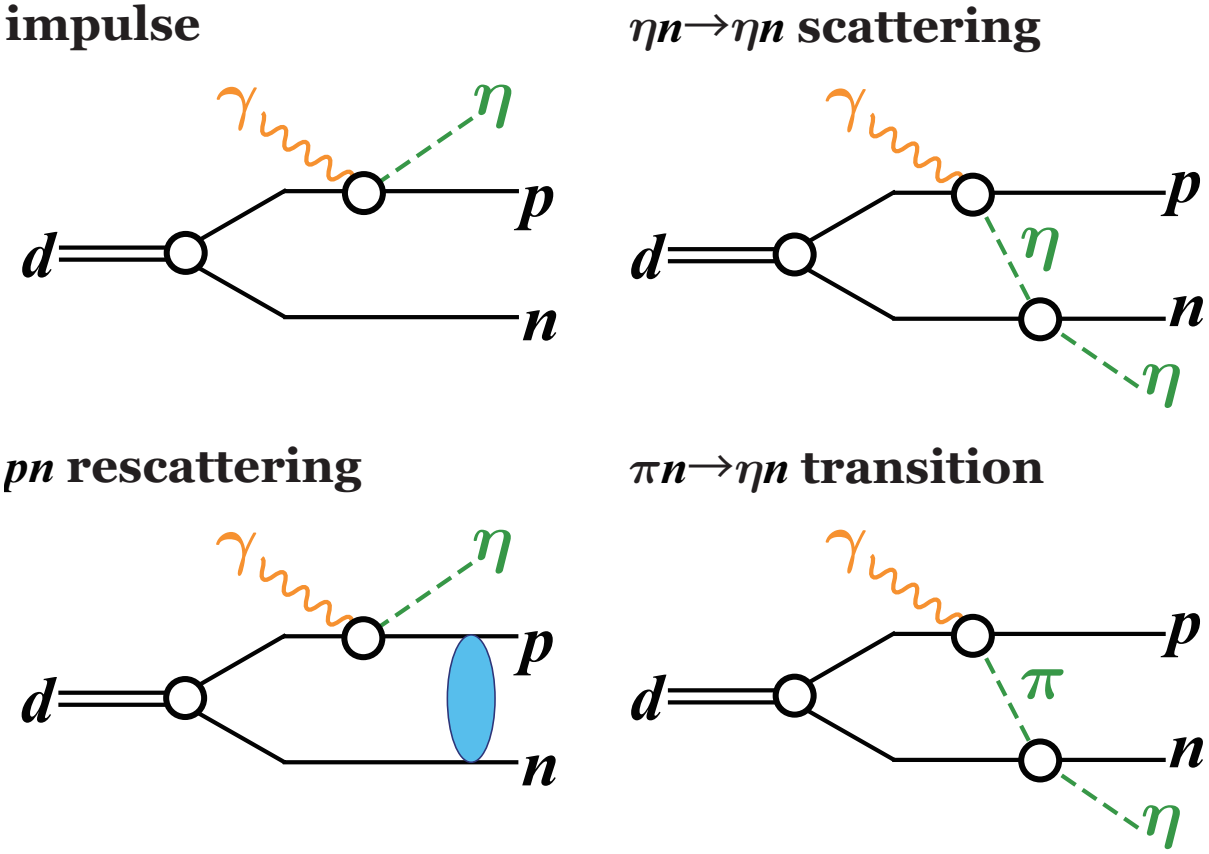


Fig.4. Four kinds of diagrams: impulse, $\eta n$ scattering, $pn$ rescattering, and $\pi n \to \eta n$ transition terms, which are considered in the DCC model calculation for the $\gamma d \to \eta pn$ reaction [13]. The $\pi n \to \eta n$ transition and $pn$ rescattering terms are expected to be small.

checked. The $d\sigma/dM_{\eta n}/d\Omega$ cross section with 5% error, binned in 1 MeV width of $M_{\eta n}$, can determine the Re$[a_{\eta n}]$ value at the precision of approximately $\pm 0.1$ fm. The model dependence of the deuteron wave function is found to be less than 0.5% near $M_{\eta n} \sim M_\eta + M_n$. The details of the results can be found in Ref. [13], where the possibility of the effective-range ($r_{\eta n}$) extraction is also discussed.

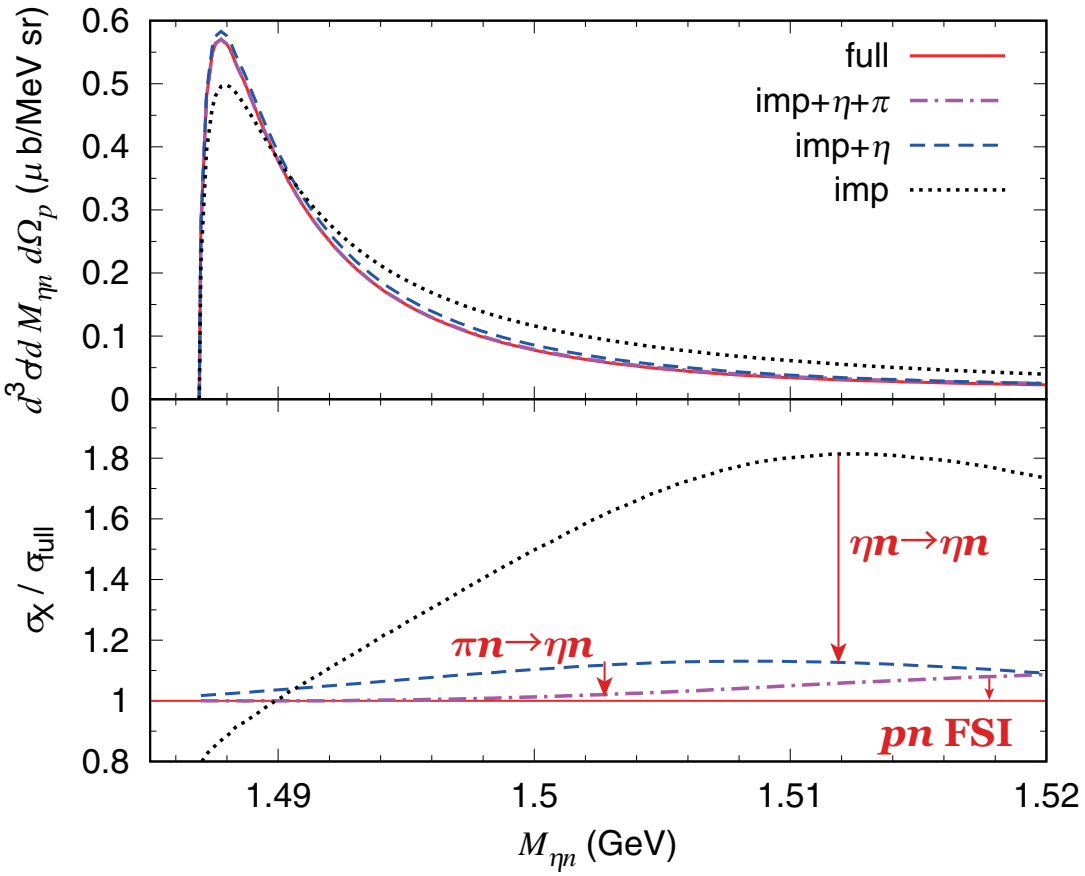


Fig.5. The differential cross section $d\sigma/dM_{\eta n}/d\Omega$ as a function of the $\eta n$ invariant mass, which is equivalent to the $\eta n$ relative momentum (upper panel). The solid curve (red) shows the cross section from the full calculation, and the dotted curve (black) is the cross section using the impulse term only. The dashed curve (blue) shows the result from the impulse and $\eta$-exchange terms, and the dash-dotted curve (magenta) shows the impulse, $\eta$-exchange, and $\pi$-exchange terms, Ratios of the differential cross sections calculated to those from the full calculation (lower panel). This figure is taken from Ref. [13] [S.X. Nakamura *et al.*, arXiv: 1704.07029 (nucl-th)].

## §3. Experimental setup

The differential cross sections for the $\gamma d \to p\eta n$ reaction will be measured at ELPH using the FOREST electromagnetic calorimeter system [16, 17] together with an additional forward charged-particle spectrometer [18]. Fig. 6 shows the experimental setup for the precise determination of $a_{\eta n}$. The incident photon energy ranges from 0.82 to 1.26 GeV [11] for the circulating electron energy of 1.32 GeV in the electron synchrotron [19]. The details of the FOREST detector including the liquid deuterium target is described elsewhere [16]. The forward scattered proton is momentum-analyzed with a bending

magnet (transported from the low-energy ring of KEKB) behind FOREST. The trajectory of a charged particle is measured with two planar drift chambers (DCs), and the time of flight is measured with a plastic scintillator (PS) hodoscope. Additional $e/\pi$ and $\pi/K$ separations are made using SF5 lead-glass and aerogel Cherenkov counters, respectively.

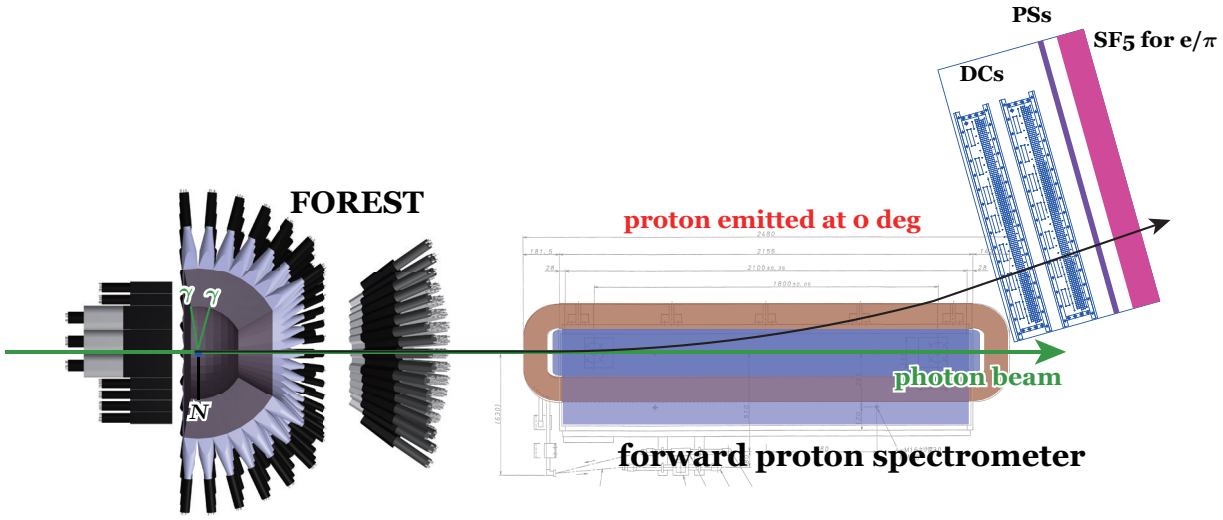


Fig.6. Experimental setup at ELPH for the precise determination of $a_{\eta n}$. The momentum and time of flight of the proton scattered at 0° are measured through a bending magnet. The forward emitted proton is momentum-analyzed with a bending magnet behind FOREST. The trajectory of a charged particle emitted at 0° is measured with two planar drift chambers, and the time of flight is measured with a plastic-scintillator hodoscope. Additional $e/\pi$ separation is made using SF5 lead-glass Cherenkov counters.

The expected proton-missing-mass resolution, which corresponds to the $\eta N$ invariant-mass resolution, is approximately 5 MeV. The value of the mass resolution are given by the photon tagging resolution (0.5–2.5 MeV) [11], the time resolution for the PS hodoscopes (40 ps), and the flight length of approximately 4.5 m.

We plan to determine Re$[a_{\eta n}]$ using the ratio of measured cross sections for $\gamma d \to \eta pn$ divided by those for $\gamma p \to \eta p$ convoluted with the proton momentum distribution in the deuteron. This can reduce the systematic uncertainty from the coverage of the forward spectrometer. The ratio also cancels the uncertainty of the elementary $\gamma p \to \eta p$ amplitudes [13]. Thus, we take both the data with the liquid hydrogen and deuterium targets. The first series of the experiments will start in the end of this October (2017) to determine Re$[a_{\eta n}]$ with a precision of 0.2–0.3 fm. Our final goal is to provide the Re$[a_{\eta n}]$ (Re$[r_{\eta n}]$) value with a precision of 0.1 fm (0.5 fm) using more high-intensity photon beams.

## §4. Commissioning

The measurement of the 3D magnetic flux of the bending magnet for the forward spectrometer BLC is described in §4.1. The results from the test experiment for the additional detectors using positron beams for testing detectors are reported: punch-through counters for SCISSORS III in §4.2, drift chambers (DCs) in §4.3, plastic-scintillator (PS) hodoscope in §4.4, and SF5 lead-glass counters in §4.5. In

addition, commissioning of the total system of the new FOREST experiment was made from May 22 to 30 in 2017 although the placement of the new detectors is temporary and we only take the liquid-hydrogen data due to the accelerator trouble. This commissioning is described in §4.6.

### 4.1 Bending magnet for the forward spectrometer BLC

We placed a bending magnet, which was transported from KEK, behind FOREST to measure the forward emitted protons. This magnet was called local chromaticity correction bending magnet (Blc) used in the 3.5 GeV positron ring (LER) in KEKB. We call it BLC instead of Blc. The excitation test of BLC with a dedicated power supply QC1LE was successfully finished on December 12 in 2016. We have decided the standard coil current of BLC is 1400 A although BLC was used with a current of 1000 A at maximum. The limit of the maximum current of 1400 A is determined by the primary 400-V current source and cooling power by the water in the GeV-$\gamma$ experimental hall.

The magnetic flux in the $xy$ plane is obtained using a 2D static magnetic and electric field calculation code Poisson Superfish with an assumption of the $z$-axis translational symmetry. The calculated magnetic flux at the center was 158.2 and 719.5 mT for the coil current of 300 and 1400 A, respectively. We measured them and obtained values are 159.4 and 717.2 mT, which are consistent with the calculated values within 0.5%. We also measured the 3D magnetic fluxes using a 3D hall probe, system, which was borrowed from Strange Nuclear Physics laboratory, Department of Physics in Tohoku University, in the $xy$ plane and along the $z$ axis near the exit of BLC in December 2016 [20, 21]. Fig. 7 shows the $x$ and $y$ components of the magnetic flux $B_x$ and $B_y$, respectively, as a function of the $x$ position. The calculated magnetic flux well reproduces the measured one.

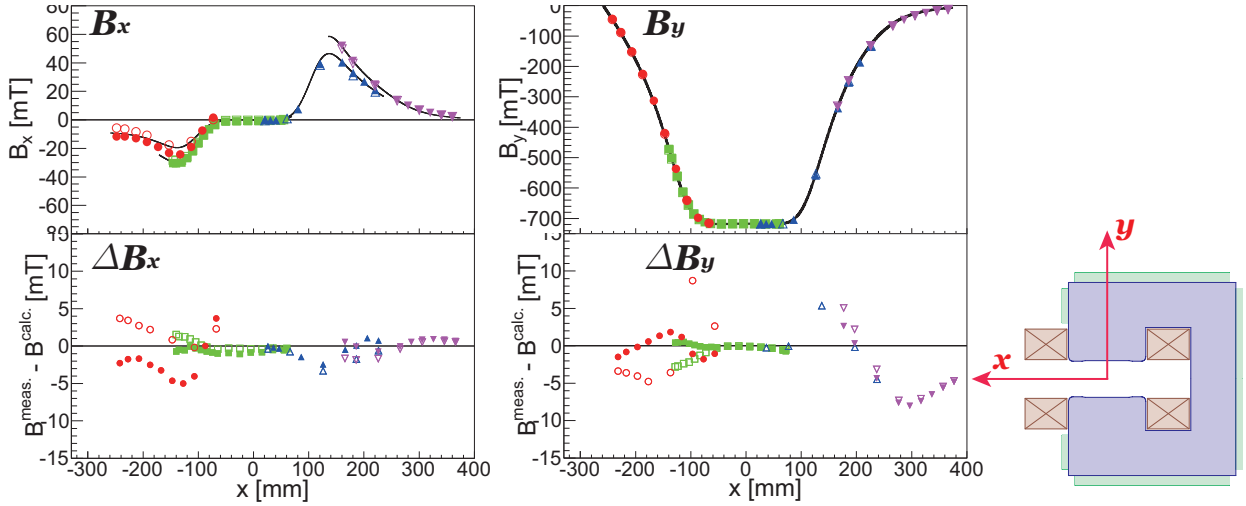


Fig.7. $x$ component of the magnetic flux $B_x$ as a function of the $x$ position (left) and $y$ component of the magnetic flux $B_y$ as a function of the $x$ position (right). The upper panels shows the measured $B_x$ and $B_y$, and the lower shows the difference from the calculated one. The different makers show different sets of the placement of the 3D linear stage for the 3D hall probe. The inset in the right-down panel shows the cross-sectional view of BLC and definition of the $x$ and $y$ axes.

### 4.2 Punch-through counters for SCISSORS III

Charged particles emitted at forward angles can be separated using the correlation between energy deposits in SPIDER and SCISSORS III. However, it is difficult to identify the charged particles which penetrate the SCISSORS III calorimeter. To extend the separation power of them, we placed 56 plastic-scintillator (PS) blocks with a size of $100 \times 100 \times 300$ mm$^3$ behind SCISSORS III. A 2-inch photomultiplier tube (PMT) is connected through a light guide at a end for each block. To investigate the energy (light output) response and time response as a function of the distance from the PMT window, we have tested some of all the PSs using the positron beams for testing detectors. The PS blocks were originally used for the TAGX experiments at the Institute of Nuclear Study (INS), University of Tokyo [24]. We have two kinds of PS materials: both are transparent but one is colorless (NE102) and the other is yellow (produced by Kyowa Hakko Co., Ltd.).

To check the difference of the PS materials, several PS blocks made of each PS material were tested. The momentum of the positron beam was 455 MeV/$c$, and it irradiated the PS block at five points from the edge to the PMT window. The trigger signal was generated in coincidence between the signals from a plastic scintillator with an area of $10 \times 10$ mm$^2$ and thickness of 3 mm and plastic scintillator with an area of $20 \times 30$ mm and thickness of 30 mm. The time resolution of this 30-mm thick PS is very high as 40–60 ps.

We fit the Moyal function (approximate Landau function) [22] to the measured energy distribution to get the centroid $\mu$ and width $\sigma$. The energy resolution given by $\sigma/\mu$ is from 6% to 12%, and getting worse from the PMT window to the edge. The individual differences of the energy resolutions are roughly 10%. The light output as a function of the distance from the PMT window is expressed by

$$L(x) = L_0 + L_1 x^2 \tag{3}$$

where $x$ denotes the distance from the edge window. The $L_1$ value is different by $\pm 25\%$ block by block, but the light output is well-reproduced in Eq. (3). We do not find any $y$-dependence in the light output, and we do not observe any difference between two PS materials. We find a different light output depending on the PMT used (Hamamatsu H6410 or H1161, and whatever else). Fig. 8 shows the energy resolutions and relative light outputs of the PS blocks in the punch-through counters as a function of the distance from the edge window.

### 4.3 Drift chambers

Two drift chambers (DCs) are placed at downstream of the bending magnet BLC for measuring the trajectory of a charged particle. The energy (momentum) of the particle will be basically determined from the time of flight measurement since we do not have a tracking device in the entrance of BLC and since we cannot achieve enough high momentum resolution. Thus the high position resolution is not required for the momentum determination. However, it is important to determine the scattering angle of the emitted proton precisely from the $x$ positions in the two DCs. The high position resolutions of two DCs are required for this purpose. The diameters of the sense and field wires in DCs is 20 $\mu$m and 100 $\mu$m, respectively. Each DC has $2 \times 56$ and $2 \times 24$ wires in the $x$ and $y$ planes, respectively. The drift

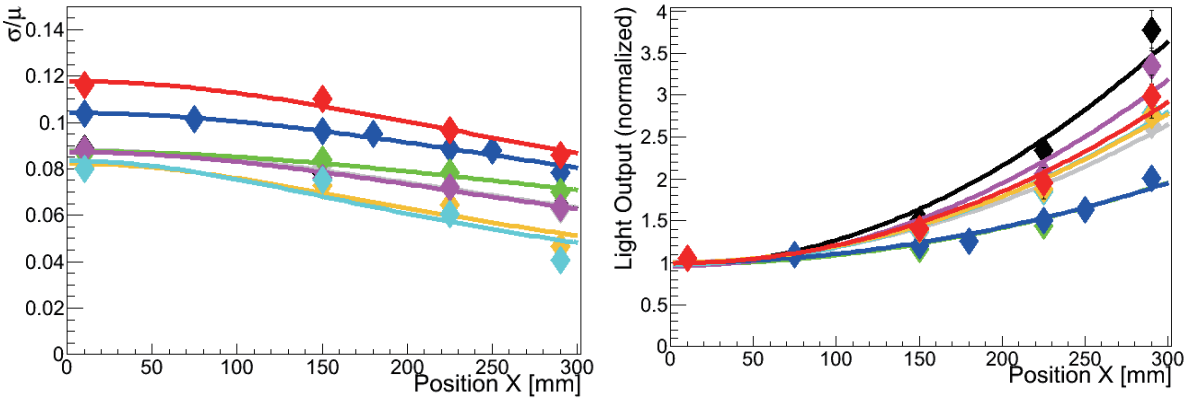


Fig.8. Energy resolution (left) and relative light outputs (right) of the PS blocks in the punch-through counters as a function of the distance from the edge window. The energy resolution is given by $\sigma/\mu$, where the centroid $\mu$ and width $\sigma$ is obtained fitting the Moyal function [22] to each measured energy distribution. The different color lines show the results on different individuals.

cell takes a square shape, and the half cell size is 10 mm.

The position resolutions of the DC planes were investigated using a 455 MeV/$c$ positron beam for testing detectors. The amplification gas used was a 50%-50% mixture of the argon and ethane since it was difficult to operate the two DCs using a cheap P10 gas due to electric discharges. The trigger signal was generated in coincidence between the signals from a plastic scintillator with an area of $10 \times 10$ mm$^2$ and thickness of 3 mm in front of the two DCs and plastic scintillator with an area of $70 \times 70$ mm and thickness of 1 mm behind the two DCs.

At first, the optimum supplied voltage was searched for. The detecting efficiency of positrons as a function of the supplied voltage (the plateau curve) was investigated, the efficiency reached approximately 100% above $-2200$ V. The drift velocity at $-2200$ V is found to be approximately 5.5 cm/$\mu$s, which is consistent with Ref. [23]. The actual incident angle of the charged particles is not 0°, where the incident angle of 0° corresponds to the perpendicular incidence. Thus, the positron beams were injected to the two DCs with incident angles of 0° and approximately 30°. Table 1 summarizes the widths of the $x$ residual distributions, and intrinsic $x$ position resolution with a perpendicular injection on the DCs and supplied voltage to field wires of $-2300$ V. A two-DC set has four $x$ planes and four $y$ planes, and the residual distribution for the $x$ planes are discussed here. The $x$ residual distributions were estimated for the three- and four-plane fits. While the four-plane fit used four wires from all the $x$ planes, the three-plane fit used three wires from the three $x$ planes excluding a wire in the $x$ plane of interest. The widths of the $x$ residual distributions are denoted by $\sigma_3$ and $\sigma_4$ for the three- and four-plane fits, respectively. The intrinsic position resolution $\sigma$ was given by the geometric mean between $\sigma_3$ and $\sigma_4$ namely $\sigma = \sqrt{\sigma_3\sigma_4}$. The intrinsic $x$ position resolution was approximately 0.3 mm for all the $x$ planes, and the $y$ position resolution was also approximately 0.3mm.

Table 1. Widths of the $x$ residual distributions, and intrinsic $x$ position resolution. The positron beam is injected on to the DCs perpendicularly, and supplied voltage to field wires is $-2300$ V. The $\sigma$ denotes the intrinsic position resolution, which is given as the geometric mean between $\sigma_3$ and $\sigma_4$ ($\sigma = \sqrt{\sigma_3\sigma_4}$), where $\sigma_3$ and $\sigma_4$ stand for the widths of the residual distributions for the three- and four-plane fits, respectively. The residual is given as a difference between the measured and fitted $x$ positions at the plane of interest. The four-plane fit uses four wires from all the $x$ planes, and the three-plane fit uses three wires from the three $x$ planes excluding a wire in the $x$ plane of interest.

| | $\sigma_4$ ($\mu$m) | $\sigma_3$ ($\mu$m) | $\sigma$ ($\mu$m) |
|---|---|---|---|
| DC1 $X$ | 205 | 470 | 310 |
| DC1 $X'$ | 225 | 464 | 323 |
| DC2 $X$ | 223 | 407 | 301 |
| DC2 $X'$ | 202 | 423 | 292 |

### 4.4 Plastic-scintillator hodoscope

For the time-of-flight measurement of charge particles, we adopted the time-of-flight counters for neutrons (NTOF) developed for the E26 experiment in J-PARC (spokesperson: K. Ozawa). A each NTOF counter consists of a plastic scintillator (PS) with a width of 100 mm, a thickness of 30 m, and a height of 600 mm. The PS material is Saint Gobain BC-408. A 2-inch PMT, Hamamatsu H243, is connected at each end of PS through a silicon cookie. The time resolution of the NTOF counter was once measured at SPring-8/LEPS. The high resolution of approximately 60 ps was achieved. The NTOF counters have not been used since the test experiment at LEPS, and the circuit used in LEPS for the NTOF counter is different from ours. The circuit for the NTOF counters is planed to consist of QTC discriminators, Fuji Diamond International GeV$\gamma$-1370, and multi-hit TDC modules, CEAN V1290A.

To investigate the time resolution of the NTOF counters, we have tested some of them using the positron beams for the testing detectors at ELPH. We place each TOF counter rotating so that the two PMTs were in the left and right sides. The trigger signal was generated in coincidence between the signals from a plastic scintillator with an area of $10 \times 10$ mm$^2$ and thickness of 3 mm and plastic scintillator with an area of $20 \times 30$ mm and thickness of 30 mm. The time resolution of this 30-mm thick PS is very high as 40–60 ps.

Positron beams were injected not only the center but also $\pm$5-, $\pm$10-cm shifted in the horizontally from the center. Fig. 9 shows the typical time difference distribution between the top and bottom PMTs. The width obtained was 3.1 channels fitting a Gaussian function to the distribution. Since the channel-to-time coefficient is 27.5 ps/channel, the time resolution of the difference was found to be 85 ps. We tested two NTOF counter with various conditions, the widths of the time differences are approximately 90 ps. The actual time is determined averaging the times from the top and bottom PMTs, and the precision of the time measurement is approximately 45 ps. Suppose the intrinsic time resolutions for the top and bottom PMT are $\sigma_1$ and $\sigma_2$, the time resolution of the difference $\sigma_{12}$ is determined from $\sigma_{12}^2 = \sigma_1^2 + \sigma_2^2$. Thus the time resolution of the average of the top and bottom PMTs $\sigma$ is given by $\sigma^2 = \sigma_1^2/4 + \sigma_2^2/4$ namely $\sigma = \sigma_{12}/2$. The positron beams were injected onto an NTOF counter not only perpendicularly but also with an incident angles of approximately $\pm 20^\circ$.

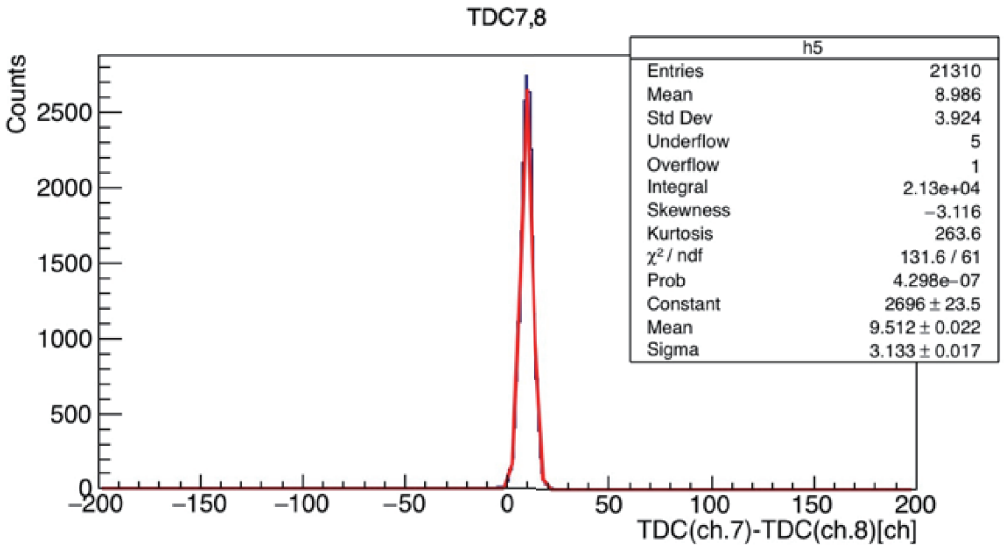


Fig.9. Typical time difference distribution between the top and bottom PMTs. The width obtained is 3.1 channels fitting a Gaussian function to the distribution. Since the channel-to-time coefficient is 27.5 ps/channel, the time resolution of the difference is found to be 85 ps.

### 4.5 SF5 lead-glass counters

The SF5 lead-glass counters are placed at most downstream of the detectors behind the bending magnet BLC. To save the space between the detectors and the west wall in the GeV-$\gamma$ experimental hall, they are placed so that the PMT is at the top (usually PMT is placed at the rear side from the surface that charged particles inject). This placement is the similar to that adopted in the E325 experiment in the proton synchrotron at KEK. We have tested ten SF5 counters in total and investigated their energy resolutions using the 100–800-MeV/$c$ positron beams for testing detectors at ELPH. The energy resolution was determined by $\sigma/\mu$ where $\mu$ denotes the centroid and $\sigma$ denotes the width. The $\mu$ and $\sigma$ were obtained fitting a Gaussian function to the measured energy distributions. The energy resolutions were found to be approximately 13%–14%, and constant almost independently of the incident energy. In general, the (relative) energy resolution becomes higher as the incident positron momentum increases. Injecting positron beams on the side surface of the SF5 counter, the effect of the longitudinal leakage of the electromagnetic shower is large. And the fraction of the longitudinal leakage becomes larger as the incident energy increases. In addition, the number of photoelectrons becomes larger and the statical fluctuation becomes smaller as the incident energy increases. These two contributions are expected to be canceled, and the energy resolution is approximately constant independently of the incident energy.

Next, we discuss the separation power of the positrons to charged hadrons. Fig. 10 shows the mean and width of the measured energy distribution of the SF5 lead-glass counter as a function of the incident positron energy. It should be noted that the positron beams are injected from the side surface of the counter. When a high-energy positron enters the SF5 counter, the electromagnetic shower takes place. No shower takes place when a charged hadron enter the counter. Thus the energy response to a

charged hadron is expected to be similar to cosmic rays $\mu^{\pm}$. Simply thinking, the positron and a charged hadron are expected to be separated using the SF5 counter at momenta higher than 300 MeV/$c$ as show in Fig. 10. The measured energy becomes high once a charged hadron makes a nuclear reaction in the SF5 counter. Thus the usage of particle identification using the SF5 counter is useful but is not perfect.

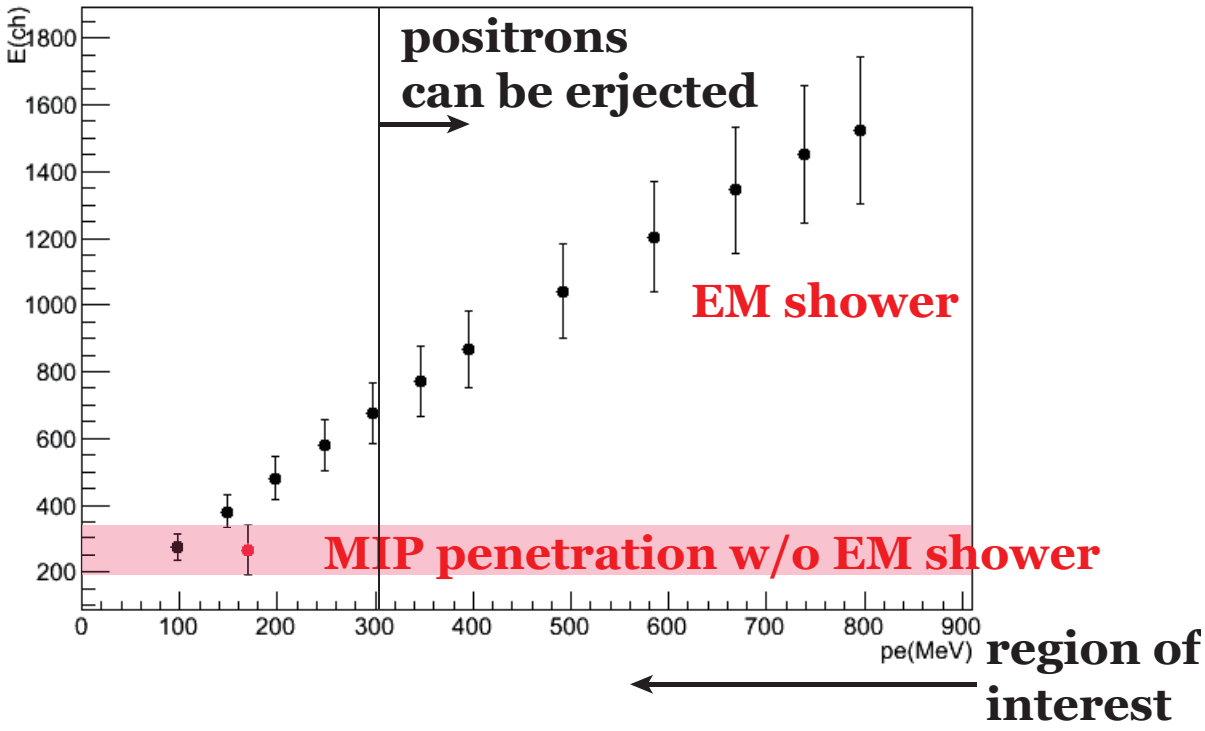


Fig.10. Mean $\mu$ and width $\sigma$ of the measured energy distribution of the SF5 lead-glass counter as a function of the incident positron energy. The positron beams are injected from the side surface of the counter. The black data points show the $\mu$ value with an error bar corresponding to the $\sigma$ value. The red data point represent the result from the measured energy distribution using cosmic rays. The incident of energy of the cosmic-ray measurement is determined in view of an equivalent energy deposit in the SF5 counter. The positron and charged hadron are expected to be separated using the SF5 counter at momenta higher than 300 MeV/$c$.

### 4.6 Commissioning

Commissioning of the new FOREST experiment was made from May 22 to May 31 in 2017. Originally our beam time had been assigned from May 15, but the beam time from May 15 to May 21 was canceled owing to the accelerator trouble happened on May 15 (error in the high voltage supplier of the electron synchrotron). The operation of the accelerators was recovered on May 22. Since the construction of the detector frame for the forward detector was not finished, the placement of the detectors were temporary. Fig. 11 shows the experimental setup of the detectors for the forward spectrometer. In the temporary setup, we placed two DCs, nine NTOF counters, and six SF5 lead-glass counters in order from the upstream.

The readout of sense wires in the two DCs was made using the 32-channel RAINER board. We used

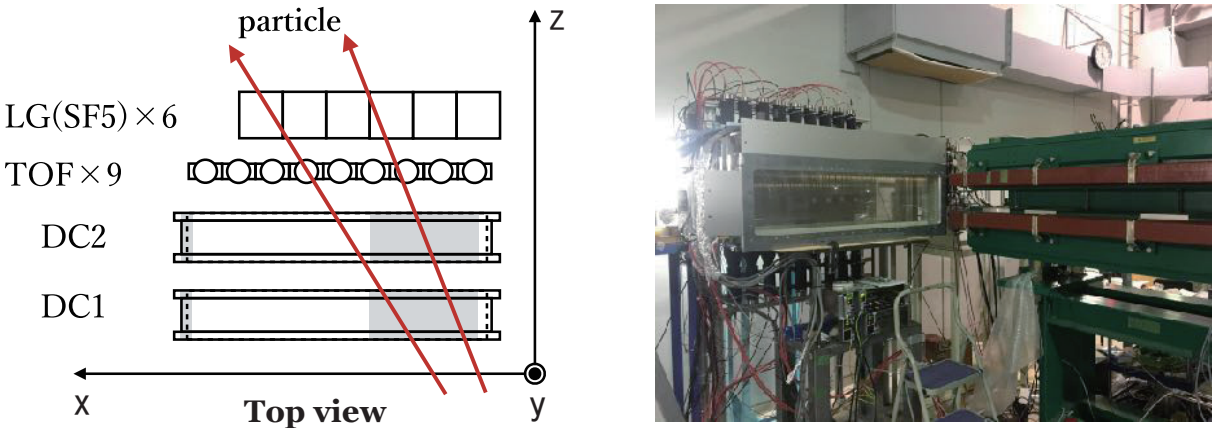


Fig.11. Experimental setup of the detectors for the forward spectrometer. The left panel shows the schematic top view of the detectors. The right panels shows a photo taken from the south-east. Two DCs, nine NTOF counters, and six SF5 lead-glass counters are placed in order from the upstream.

six boards out of ten due to the troubles, and readout signals from 64 $x$ wires and 24 $y$ wires from each DC. Although we took signals from all the $y$ wires, we took signals from wires in a 64-cm width in the BLC side. The two DCs are planed to be placed at the angle of 15.7° with respect to the $z$ axis in the new FOREST experiment. However, the DC wire planes are placed perpendicular to the $z$ (photon beam) axis in this commissioning.

The power supply for BLC, QC1LE, halted many times, indicating the ground fault error, after we operated the two-stage Gifford-McMahon (GM) refrigerator, Sumitomo Heavy Industries RKD-415D. The error was thought to happen because the resistance of cooling water is not enough high together with the noise from the refrigerator. We plan to insert ion-exchange resins in the cooling systems for the power supplier of the magnets and magnets themselves. To suppress the halt of the BLC excitation, we decrease the coil current from 1400 A to 1250 A.

First of all, we checked whether the two DCs worked well or not using the data from special runs. In these special runs, the trigger condition of the data acquisition was logic OR signal of all the tagging signals, and thick converter was placed in front of BLC to produce the positrons with the speed of light from a faint photon beam. Almost all the charged particles came to the two DCs were positrons from tagged photons. We estimated the correlation of the TDC values between the odd- and even-number wires to confirm that we correctly measured the response times from the wires. Sense wires are placed alternately in the $X$ ($Y$) and $X'$ ($Y'$) planes. When charged particles are incident on a drift chamber perpendicularly, they penetrate the interval between adjacent $X$ and $X'$ wires. Thus the sum of the TDC values for the adjacent $X$ ($Y$) and $X'$ ($Y'$) wires must be constant. Fig. 12 shows the correlation of the TDC values between the adjacent odd $(2i-1)$- and even $(2i)$-number wires. As shown in Fig. 12, Event concentrations are observed at the constant sum loci in the $Y$-$Y'$ planes for DC1 and DC2. On the other hand, Charged particles are incident on a DC at the incident angles larger than 10° in the $zx$ plane. And this incident angle becomes larger as the distance from BLC becomes longer. Charged

particles are more likely to pass through the same side from the sense wires of the $X$ and $X'$ planes in the far side (south) . The loci corresponding to the constant difference is longer for the far side. The loci corresponding to the constant sum is longer for the near side (north).

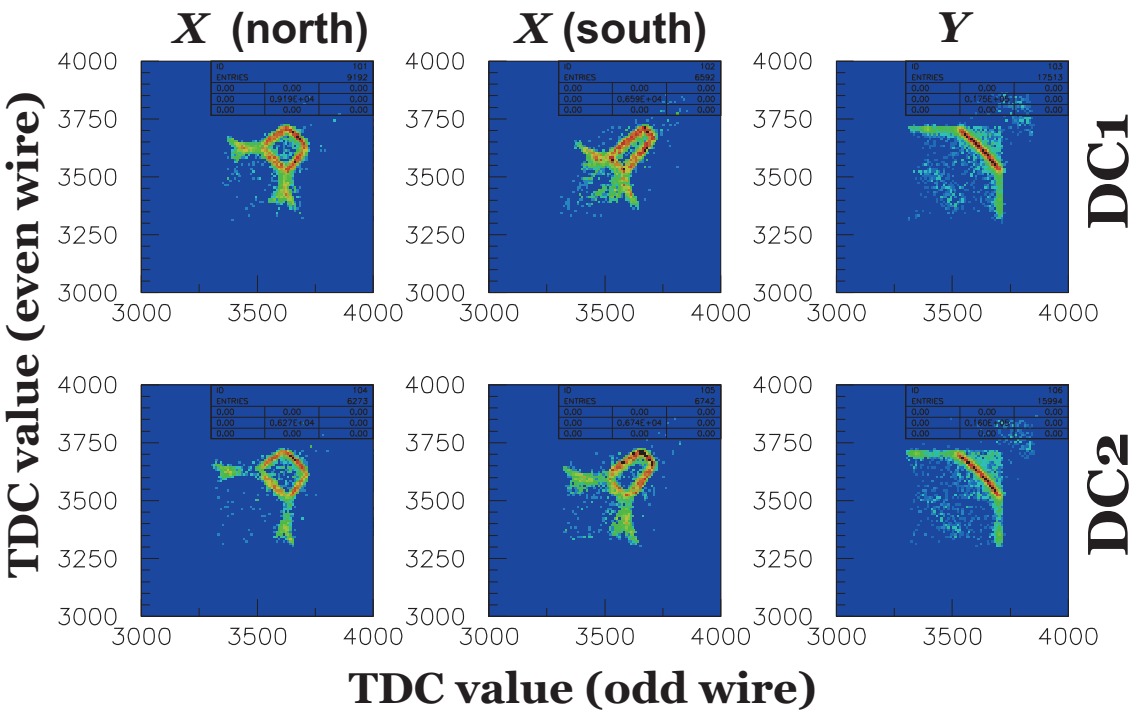


Fig.12. Correlations of the TDC values between the adjacent odd $(2i-1)$- and even $(2i)$-number wires. The upper and lower panels show the correlations for DC1 (upstream) and DC2 (downstream), respectively. The left, central, and right panels show the the correlations for the $X$-$X'$ wires in the near side (north), in the far side (south), and $Y$-$Y'$ wires, respectively.

Next, we checked the correlation of the wire numbers in the $X$-$X'$ planes between DC1 and DC2 to know the incident angle of charged particles. Fig. 13 shows the correlation of the wire numbers in the $X$-$X'$ planes between DC1 and DC2. The 8th wire in the $X$-$X'$ planes of DC1, which was removed to avoid the ground fail, was missing. Event concentration corresponds to the correlation for the positrons between the wire number in the $X$-$X'$ planes of DC1 is higher than 20 and that of DC2 is larger than 25. Since the positrons are mainly produced from the photon beam, and the maximum energy of the positron corresponds to the circulating energy of the primary electron in the synchrotron approximately 1.3 GeV. Thus events of the positron incidence exist for the wire numbers in the $X$-$X'$ planes of DC larger than 20. Event concentration in the lower part corresponds to the correlation for the events that charged particles or $X$ rays pass through the two DCs coming from the beam dump because wire number is smaller in DC2 suggesting $dx/dz < 0$. Event concentration in the left side correspond to the correlation for the events that the high-energy positive hadrons are incident on the two DC2, or for the events that charged particles come directly without passing through BLC. If charged particles are correctly momentum-analyzed in BLC, events for the wire numbers of DC1 smaller than 15 correspond to charged particles with energies higher than 1.3 GeV. If charged particles do not pass through BLC,

they can also come to the region corresponding to the wire number of DC1 smaller than 15.

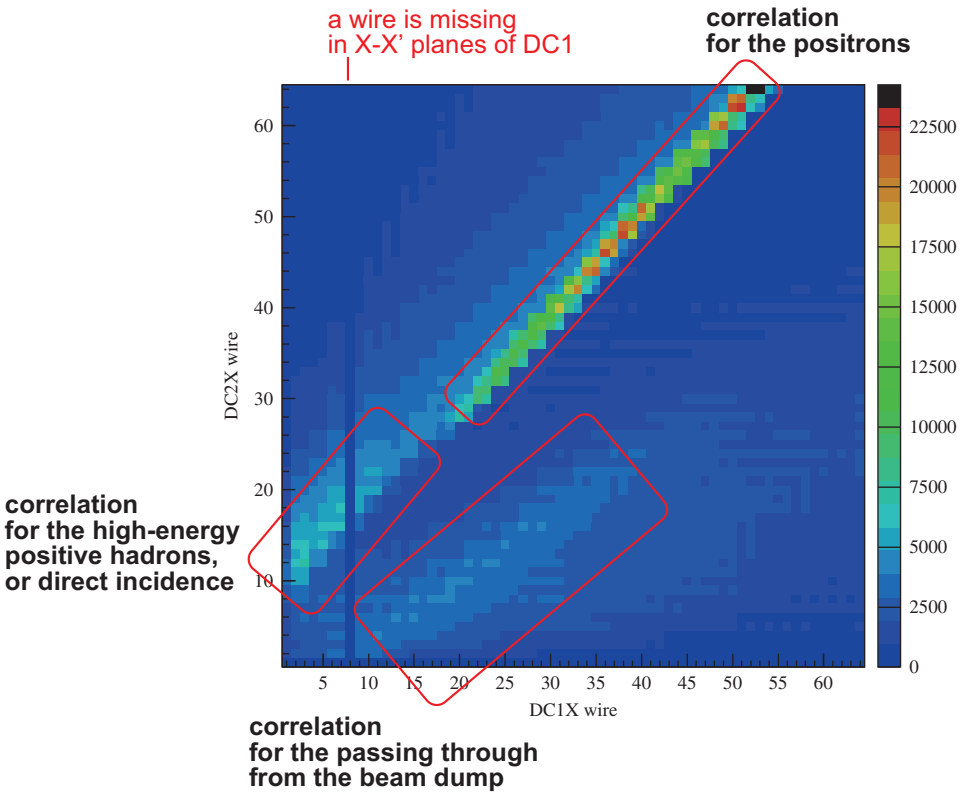


Fig.13. Correlation of the wire numbers in the $X$-$X'$ planes between DC1 and DC2. The 8th wire in the $X$-$X'$ planes of DC1 is missing. Event concentration corresponds to the correlation for the positrons between the wire number in the $X$-$X'$ planes of DC1 is higher than 20 and that of DC2 is larger than 25. Event concentration in the lower part corresponds to the correlation for the events that charged particles or $X$ rays pass through the two DCs coming from the beam dump. Event concentration in the left side correspond to the correlation for the events that the high-energy positive hadrons are incident on the two DC2, or for the events that charged particles come directly without passing through BLC.

Since the coil current for BLC was as low as approximately 1250 A in the commissioning period due to the power supplier (QC1LE) trouble , we cannot get enough bending power. Protons with a momentum around 940 MeV/$c$, which is of most interest to determine low-energy $\eta n$ scattering parameters from the $\gamma d \to p\eta n$ reaction, comes onto the second NTOF counter from the BLC side. We have estimated the time difference distributions between a NTOF counter and tagging signals to check whether the positive pions and protons are well separated or not. Coincidence between the FOREST detector and tagging signal is required to remove the accidental background contributions. A sideband-subtraction method was applied to get the coincidence of them, where the prompt time difference (the FOREST time is subtracted by the response time of hte tagging signal) region was defined from $-8$ to $+2$ ns and the background from $-28$ to $-8$ and from $+2$ to $+22$ ns. Fig. 14 shows the time difference distributions between the NTOF and tagging signals for eight NTOF counters. Here, the coincidence between the FOREST detector and tagging signals was confirmed. The connection of the top PMT to the first NTOF

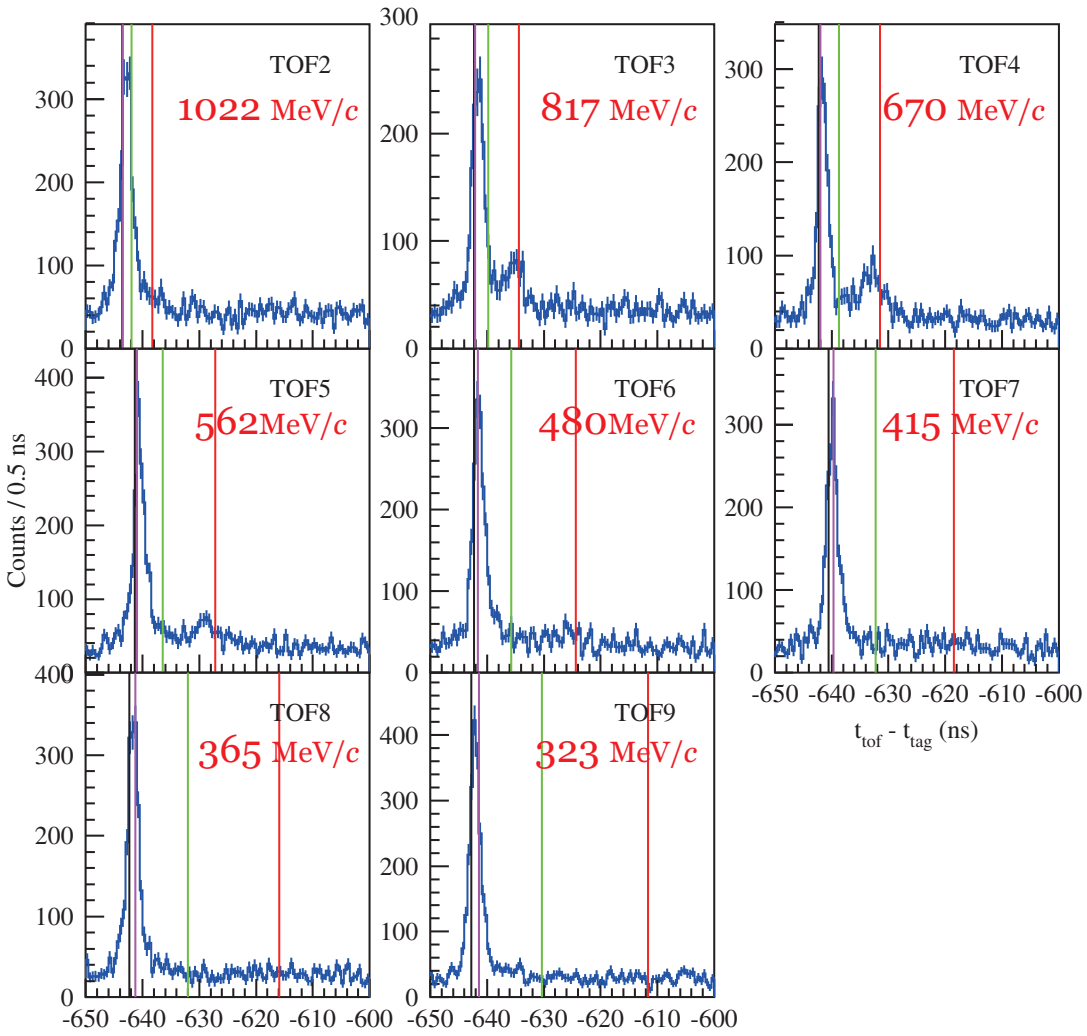


Fig.14. Time difference distributions between the NTOF and tagging signals for eight NTOF counters. The coincidence between the FOREST detector and tagging signals is required. The block, magenta, green, and red vertical lines represent the time difference for the positrons, positive pions, positive kaons, and protons with an energy of central momentum coming to each NTOF counter.

was broken during the experiment, and light output was very small. Thus, we omit the first NTOF (TOF1) data.

We compared the measured time difference to the calculated time difference for the positive pions, positive kaons, and protons with an energy of central momentum coming to each NTOF counter. To make the calibration of the time difference, the position corresponding to the positron peak was obtained using the special runs, in which the trigger condition of the data acquisition was logic OR signal of all the tagging signals, and thick converter was placed in front of BLC to produce the positrons with the speed of light from the photon beam. Both the positive pion and proton peaks were clearly observed from the second (TOF2) to fifth (TOF5) NTOF counters, corresponding to the momentum above 562 MeV/$c$. It should be noted that still we have a large amount of the uniform background contribution from accidental coincidence.

Since we successfully readout the signals from DCs, the time difference distribution can be also estimated wire by wire. Fig. 15 shows the correlation between the wire number in the $X$-$X'$ planes of DC1 and time difference between the NTOF and tagging signals. The loci corresponding to the positive pions and protons were clearly observed. The scattering angle of charged particles in the horizontal plane which can be correctly momentum-analyzed ranged from 0° to 1°. Different scattering angles make different flight lengths, and make the time difference distributions broader. After the $T_0$ calibration and $xt$ curve determination for the DC wires are finished, the time difference distributions will be estimated more accurately.

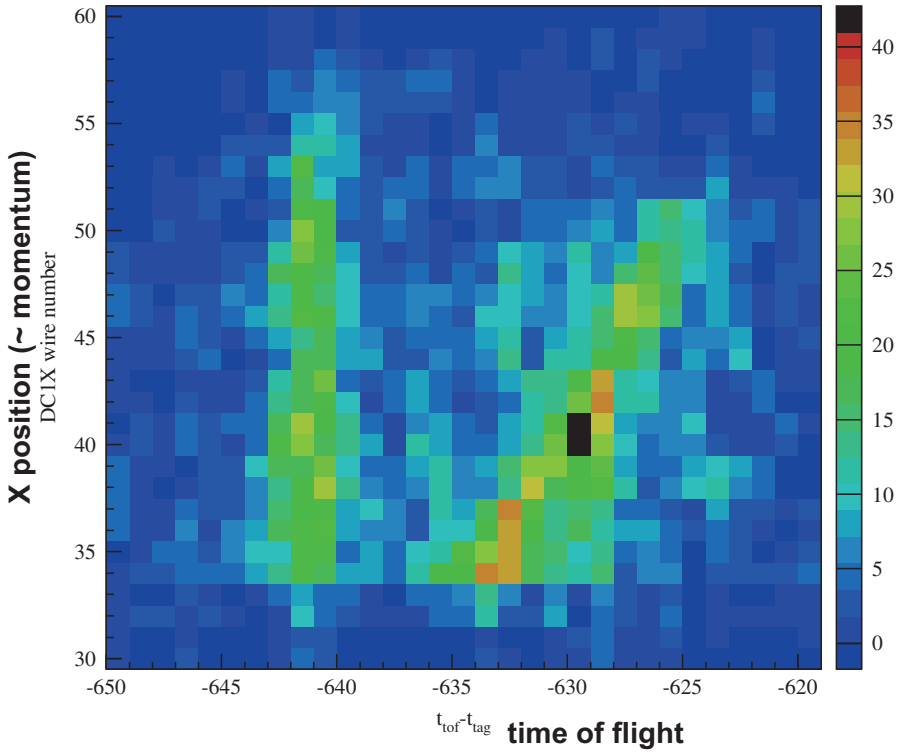


Fig.15. Correlation between the wire number in the $X$-$X'$ planes of DC1 and time difference between the NTOF and tagging signals. The loci correspond to the positive pions (left) and protons (right) are clearly observed.

## §5. Summary

An experiment is planed at ELPH using the FOREST detector to determine the $\eta n$ scattering length $a_{\eta n}$ using the $\gamma d \to p\eta n$ reaction. Proton detection at 0° using 0.94 GeV photon beam give the recoilless condition of $\eta$ mesons. The $\eta n$ final-state interaction can be studied thanks to the small relative momentum between $\eta n$. Commissioning of the new detectors at downstream of the forward spectrometer has been finished. The first series of the experiments will start in the end of this October (2017) to determine Re$[a_{\eta n}]$ with a precision of 0.2–0.3 fm. We will provide an accurate Re$[a_{\eta n}]$ value ($\sim$ 0.1 fm) in the near future.

## Acknowledgments

The authors give thanks to the ELPH accelerator staff for their great efforts in the stable operation of the electron synchrotron. They deeply acknowledge S.X. Nakamura and H. Kamano for giving us the predictions for the $\eta n$ rescattering effect in the proposed $\gamma d \to p\eta n$ experiment. This work was supported in part by Grants-in-Aid for Scientific Research (A) (24244022), for Scientific Research (C) (26400287), and for Scientific Research (A) (16H02188).

## References

[1] Q. Haider and L.C. Liu: Int. J. Mod. Phys. E **24**, 1530009 (2015);
and references therein.

[2] A.M. Green and S. Wycech: Phys. Rev. C **71**, 014001 (2005);
Erratum Phys. Rev. C **72**, 029902 (2005).

[3] R.A. Arndt *et al.*: Phys. Rev. C **72**, 045202 (2005).

[4] C. Patrignani *et al.* (Particle Data Group): Chin. Phys. C **40**, 100001 (2016).

[5] S.D. Bass and A.W. Thomas: Phys. Lett. B **634**, 368 (2006);
S.D. Bass and A.W. Thomas: Acta Phys. Polon. B **45**, 627 (2014).

[6] A. Matsuyama, T. Sato, T.-S.H. Lee: Phys. Rep. **439**, 193 (2007).

[7] H. Kamano *et al.*: Phys. Rev. C **88**, 035209 (2013).

[8] A. Sibirtsev *et al.*: Phys. Rev. C **65**, 044007 (2002).

[9] A. Fix and H. Arenhövel: Eur. Phys. J. A **19**, 275 (2004).

[10] T. Ishikawa *et al.*: ELPH-2803 letter of intent (2014);
T. Ishikawa *et al.*: ELPH-2844 experiment (2016).

[11] T. Ishikawa *et al.*: Nucl. Instrum. and Meth. A **622**, 1 (2010).

[12] T. Ishikawa *et al.*: Nucl. Instrum. and Meth. A **811**, 124 (2016).

[13] S.X. Nakamura, H. Kamano, and T. Ishikawa: arXiv: 1704.07029 (nucl-th).

[14] R. Machleidt: Phys. Rev. C **63**, 024001 (2001).

[15] V.G.J. Stoks, R.A.M. Klomp, C.P.F. Terheggen, and J.J. de Swart: Phys. Rev. C **49**, 2950 (1994).

[16] T. Ishikawa *et al.*: Nucl. Instrum. and Meth. A **832**, 108 (2016).

[17] T. Ishikawa *et al.*: Phys. Lett. B **772**, 398 (2017);
T. Ishikawa *et al.*: PoS (INPC2016) 267;
T. Ishikawa *et al.*: PoS (Hadron2013) 095.

[18] T. Ishikawa *et al.*: JPS Conference Proceedings **13**, 020031 (2017);
T. Ishikawa *et al.*: JPS Conference Proceedings **10**, 031001 (2016).

[19] F. Hinode, et al.: Journal of Physics: Conference Series **425**, 072011 (2013).

[20] T. Ishikawa, Internal GeV-$\gamma$ Analysis Note HD No. **413**$\mathcal{N}$ (2016).

[21] Y. Inoue, Internal GeV-$\gamma$ Analysis Note HD No. **415**$\mathcal{N}$ (2017).

[22] J.E. Moyal, Phil. Mag. 46 (1955) 263; M.D. Marucho, C.A. Garcia Canal, H. Fanchiotti, Int. J. Mod. Phys. C 17 (2006) 1461.

[23] A. Peisert, F. Sauli, Drift and Diffusion of Electrons in Gases: A Compilation, CERN-84-08 (1984).

[24] K. Maeda, private communication.

(ELPH Experiment : #2823)

# Evaluation of Time Projection Chamber for H-dibaryon search experiment and test of Multi-gap Resistive Plate Chamber for J-PARC Heavy-Ion project

H. Sugimura[1*], T. Chujo[2], H. Ekawa[1], S. Hasegawa[1], Y. Ichikawa[1], S. Kimbara[1], H. Sako[1], S. Sato[1], K. Tanida[1], J.K. Ahn[3], S.H. Kim[3], W.S. Jung[3], W.J. Choi[3], J.Y. Lee[4], R. Aoyama[2], T. Ichisawa[2], H. Kato[2], T. Nonaka[2], K. Sato[2], T. Sugiura[2], and M. Inaba[5]

[1]*Japan Atmic Energy Agency (JAEA), Tokai, Ibaraki, 319-1195, Japan*
[2]*Faculty of Pure and Applied Sciences, Division of Physics, University of Tsukuba, Tsukuba, Ibaraki, 305-8571, Japan*
[3]*Department of Physics, Korea University, Seoul 02841, Republic of Korea*
[4]*Department of Physics and Astronomy, Seoul National University, Seoul 151-747, Republic of Korea*
[5]*Faculty of Industrial Technology, Tsukuba University of Technology, Tsukuba, 305-8520, Japan*

A Time Projection Chamber (TPC) has been developed for an H-dibaryon experiment at J-PARC. The TPC consists of readout pad, three-layer GEM, gating-grid and field cage. To evaluate basic performance, we have conducted beam test with positron beam at Research Center for Electron Photon Science (ELPH). In event display, the positron track was clearly seen, and position resolution was measured to be 400 $\mu$m in the pad direction and 600 $\mu$m in the drift direction, respectively. In parallel, Multi-gap Resistive Plate Chamber (MRPC) was tested for time resolution study for the J-PARC Heavy-Ion Project.

## §1. Introduction

### 1.1 Time Projection Chamber

We have proposed the H-dibaryon search experiment via ($K^-$, $K^+$) reaction at Hadron Experimental Facility, J-PARC. The proposed experiment will be measured invariant mass spectrum of $\Lambda\Lambda$ or $\Lambda p\pi$ from H decay, with a mass resolution of 1 MeV/$c^2$. To measure this decay mode, we have developed the TPC (Fig.1). The TPC has the octagonal drift volume defined by the field cage, the cathode plane at the top and the amplification region at the bottom. The whole volume is filled with a gas mixture of Ar-$CH_4$(P-10). The target is located inside the drift volume. For amplification, we adopted tripple GEMs with the configuration of 50 $\mu$m for top two layer and 100 $\mu$m for bottom layer to achieve gain of the $10^4$ level. The most characteristic specification of our TPC is to operate not only decay particle but also high rate kaon beam up to $10^6$ cps. In high rate operation, space charge effect in the drift volume can not neglect. To reduce this, we adopted to locate gating grid just above the top of GEM layer. The purpose

*Present address: High Energy Accelerator Research Organization (KEK), Tsukuba, Ibaraki, 305-0801, Japan

of the ELPH experiment is to evaluate position resolution and position shift due to space charge effect with and without gating grid.

Fig.1. (left) The picture of developed TPC. (right) Gating wire, GEM, readout pad and conversion connector from the top picture.

### 1.2 Multi-gap Resistive Plate Chamber

A Multi-gap Resistive Plate Chamber (MRPC) is one of the most commonly used apparatus as a time-of-flight detector for charged particle identification. MRPC is the basically a gaseous detector operated at the avalanche mode, and applying a high voltage on the electrode, which is usually about 14 kV. In between the electrodes, we produced many gas gaps by stacking many high resistive materials, such as float glasses, with a spacing of few $\mu$m gas gap. When a charged particle passes through, the electron avalanche develops and it induces charge on the readout pad. This is the signal with a good timing characteristics, and we can build TOF detector easily less than 100 ps of timing resolution with high detection efficiency.

We have been working on the prototype of MRPCs for many years, to optimize the various parameters of this detector, seeking for the timing resolution below 30 ps. At this beam test experiment at ELPH, we have tested basically three types of MRPC detectors as follows.

- Small area MRPC (4 stacks)
- Large area MRPC (4 stacks)
- Small area MRPC with narrow pad width (1 stack)

We show the results at this beam test for each type of MRPC in Sec3.2.

## §2. Experimental Setup

The experimental setup is shown in Fig.2. There are several counters to evaluate the TPC performance. A large plastic scintillation counter (T1) whose size is $50^H$ mm $\times$ $50^V$ mm, is located at the most upstream. A small plastic scintillation counter (F1) whose size is 1 cm $\times$ 1 cm, is located at just downstream of the T1. Two silicon-strip detectors (SSD) with an 80 $\mu$m strip pitch and a sensitive area

of $31^H \times 30.8^V$ mm$^2$ were located in front of and behind the TPC, respectively. The TPC was located between two SSDs. The positron beams are measured by the SSD and the TPC. The SSDs play a role of reference of the track position to evaluate beam shift due to space charge effect inside of the TPC. T2 and F2 are same counter as T1 and F1, respectively and are located at the downstream of the SSD2. A plastic scintillation counter (VETO) has a small hole at beam through position to detect scattered positron and to reject from trigger, and is located at behind the F2. MRPCs were located at downstream of the TPC measurement counters.

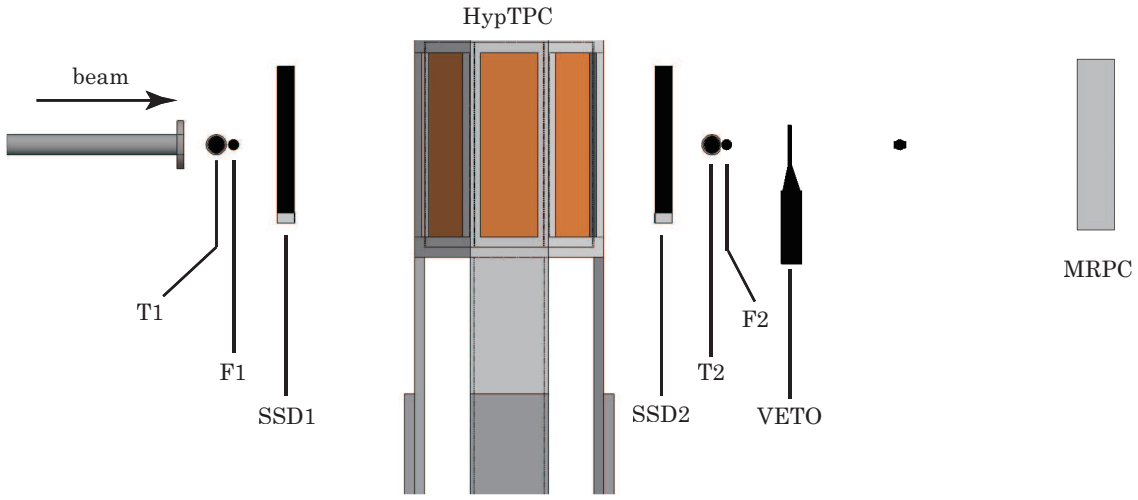


Fig.2. ELPH setup

# §3. Analysis

## 3.1 TPC analysis

### 3.1.1 No Gating-Grid operation

In this ELPH expetiment, we tested basic performance of the TPC. Figure 3 left shows event display of positron track. Pad color indicates amount of charge deposit of each pads. The track was clearly seen at central position. A concerning point is that the track was slightly bent at the edge of the TPC. The reason has not been recognized yet.

Figure 3 shows typical wave form. Dynamic range was set to 120 fC and the shaping time was 212 ns with $V_{GEM}$ of 315 V. S/N ratio was more than 100 that is because we could identify the clear signal.

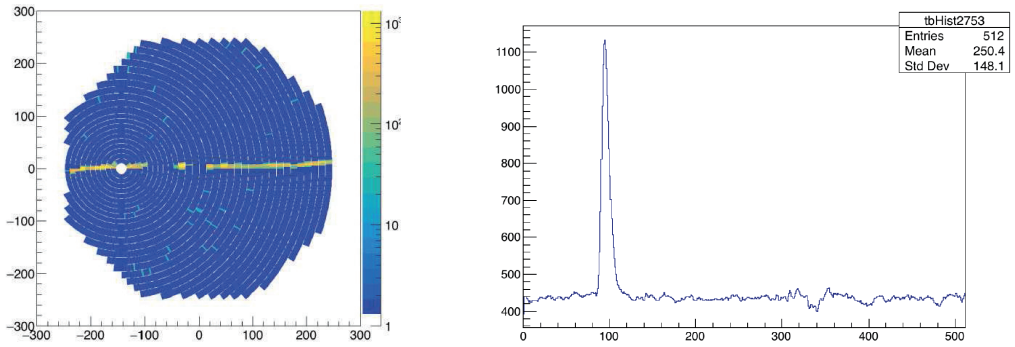


Fig.3. (left) Event display of the positron track. (right) Typical wave form get from readout pad.

Figure 4 shows the pad efficiency of each layer. The horizontal axis shows layer number. The order of layer number is defined from central target position, and total layer is 32. The "$ncl$" indicates number of cluster. The signal was clustered in each layer. The pad efficiency was estimated more than 90% at the $ncl \geq 2$, and more than 99% at the $ncl \geq 1$. However, there were some low efficiency layers. These layers could not be measured because of the GEM broken. In this test measurement, we found that the GEM was often broken at more than 320 V. To increase 320 V, we should modify GEM structure (support frame etc.) and take long time aging.

Figure 5 shows typical residual distributions in the direction of pad and drift, respectively. We tested with no magnetic field ($B = 0$) and low electric field ($E = 130V/cm$), which is relatively lower than operation voltage ($E = 180V/cm$) [1]. In the pad direction analysis, we applied cluster size more than 3 and calculated position with weighted mean method. The position resolution was estimated to $400 \sim 500$ $\mu$m. In the drift direction analysis, we calculated from maximum time bin obtained from the wave form, and applied mean value from the Gauss fit. The position resolution was estimated to $500 \sim 600$ $\mu$m.

### 3.1.2 Gating Grid operation

Figure 6 shows typical wave form of gating grid operation. We applied gating voltage at the range from $\pm$25 V to $\pm$50 V. The leftmost oscillation from 20 to 150 time bin and the rightmost peak from 420

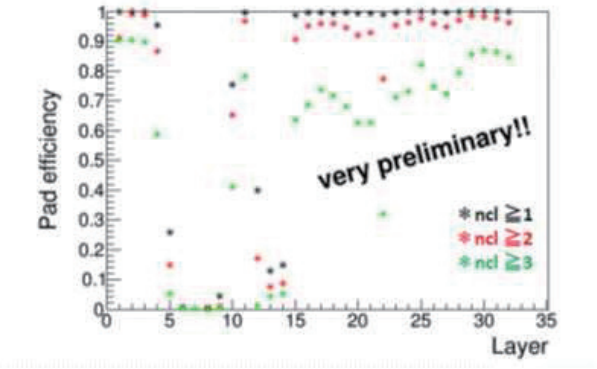


Fig.4. Pad efficiency of each layer.

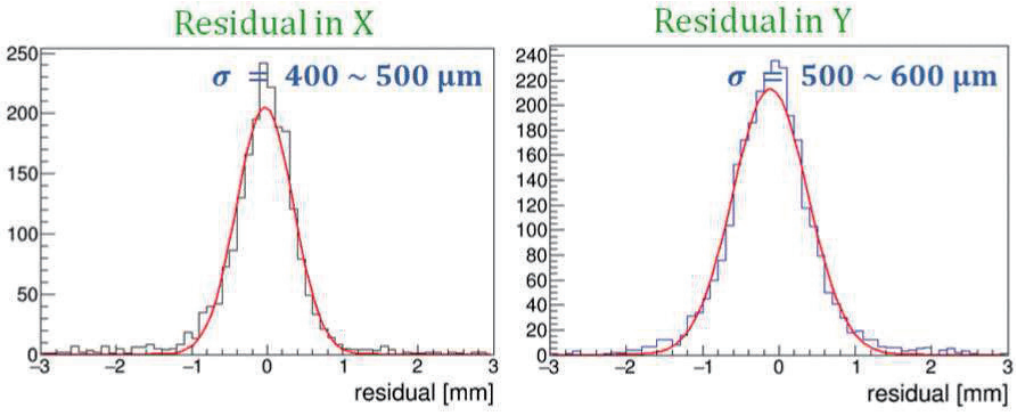


Fig.5. Residual distributions in the direction of pad and drift, respectively

time bin show noise induced by the leading and trailing edges of the gate pulse. The middle peak is the signal from positron track at the height of 45 cm from gating grid. In the no gating grid operation, S/N ratio was more than 100. However, we can not neglect gating pulse noise. If the tracks pass through near the gating grid, signal is overlapped with gating pulse noise. Figure 7 shows pad inefficiency at the height of 45 cm when the gaint grid is CLOSE. In the closed mode, signal can not be reached at the amplification area (GEM). If gating grid CLOSE level is low, some charge is leaked and amplifier at GEM. Signal was not detected around the $V_{gate} = 50$.

In this test experiment, we didn't take data at low height operation with gating grid. Detailed gating grid study will be measured near future.

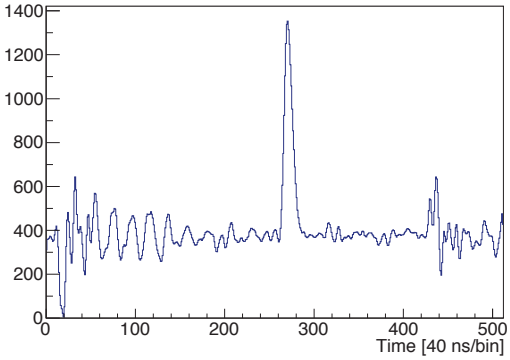


Fig.6. Typical wave form of gating grid operation

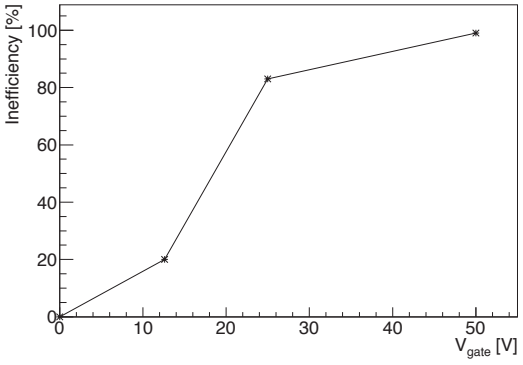


Fig.7. Inefficiecy of the Gate CLOSE operation

### 3.2 MRPC analysis

#### 3.2.1 Small area MRPC

We developed 4-stucked MRPC, which is called "Small area MRPC". Its effective area is 100 mm wide and 136 mm long, and total hight is about 30 mm. The signal can be read out from both sides of read out pad. In this type, we measured timing resolution and efficiency as a function of applied voltage and position. Figure 8 shows a sample of signal shape taken by the DRS4 evaluation board [2]. Three parameters were extracted by fitting a signal, i.e. amplitude of signal $A$, charge $Q$ (integrated around a peak), and a time when it reaches at $A/2$, $t_0$.

The correlation between amplitude and charge is shown in Figure 9. A linear distribution is seen at the middle panel, and some points are placed above the line. These can be considered as streamers, which usually have two-peaked signals as shown in the top-left, and a larger decay time as shown in the bottom-left panel.

Figure 10 shows the voltage dependence of efficiency. The efficiency is defined as the ratio of the number of events whose amplitude of MRPC signals are $>$ 10 mV to the number of triggered events by scintillation counters. Filled circles are for the efficiency including streamers, and open circles are the fraction of the streamers over the total number of events.

The color (red or blue) corresponds to the different position of beam spot as shown in the figure.

Figure 10 shows that the efficiency gets better to be $> 98\%$ more than 12.5 kV.

Figure 11 shows the timing resolutions as a function of the applied voltages. The beam was irradiated at the center of the counter. Streamer events are excluded from this analysis because rising signal might be deformed by the pulses come after, and exact $t_0$ parameter cannot be measured correctly. we achieved the timing resolution of $67.4 \pm 2.8$ ps at 12.0 kV and achieved efficiency up to 98% at the same time. We concluded that the best voltage setting for this type of MRPC is 12.0 kV from this data.

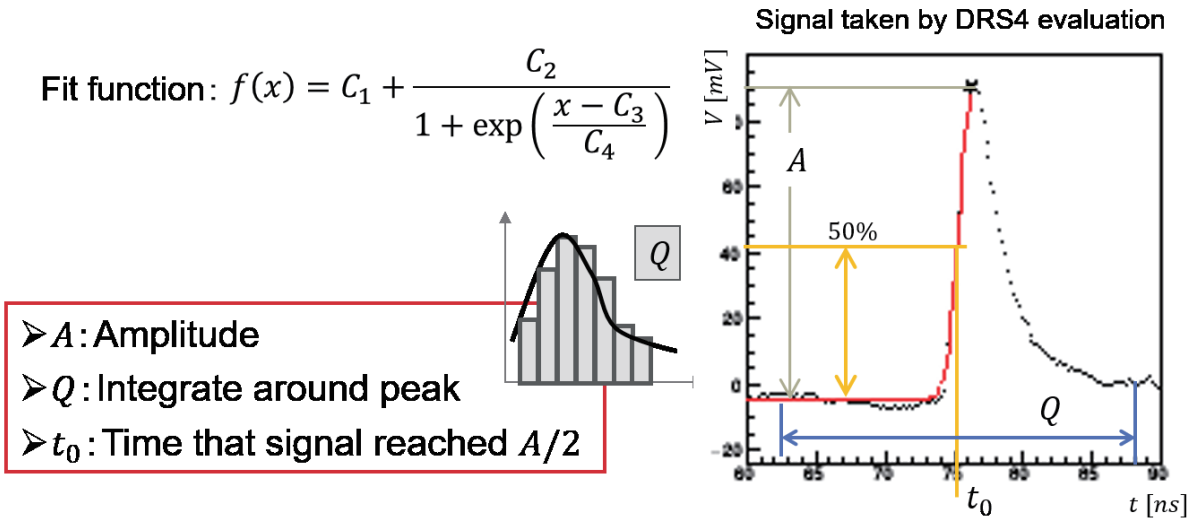


Fig.8. Signal taken by DRS4 evaluation board and the method of data extraction

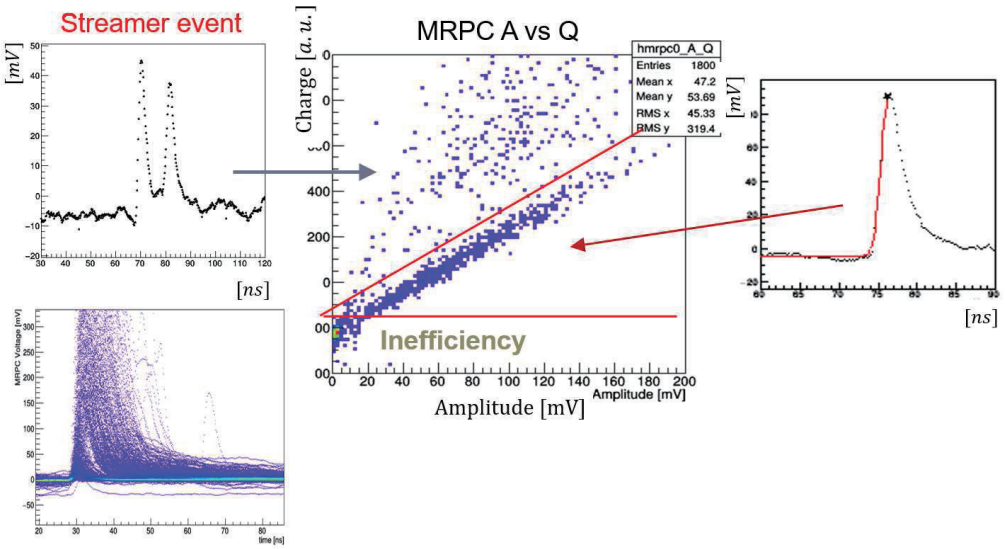


Fig.9. Scatter plot of amplitude and charge. Plots are divided into 3 groups.

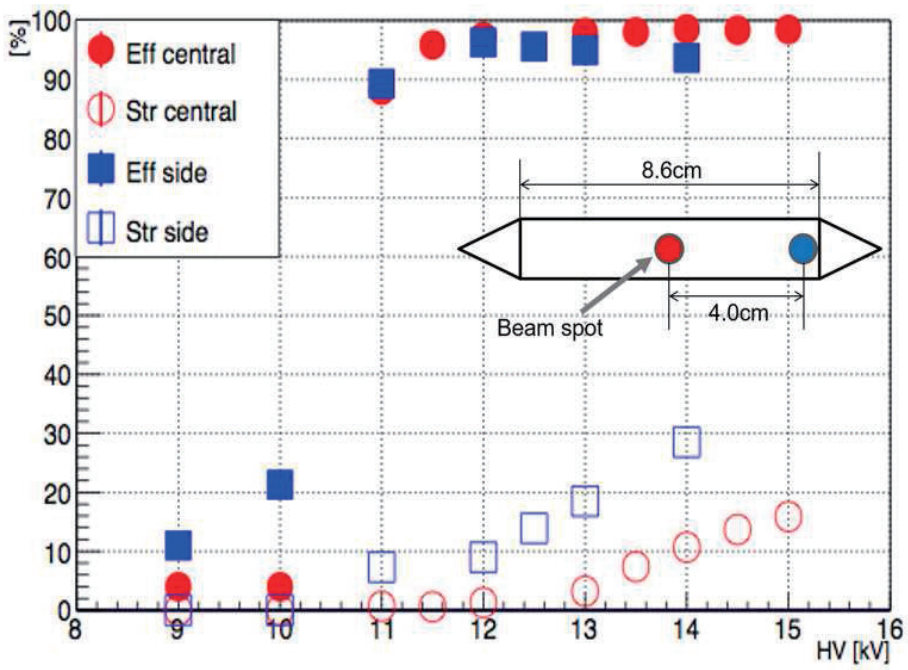


Fig.10. Efficiency and the ratio of streamer, applied voltage and beam spot dependence

### 3.2.2 Large area MRPC

Figure 12 (left) shows 30 $\times$ 20 cm$^2$ large prototype of MRPC (4 stuck), and we evaluated it with beams at ELPH. We took data in 4 different high voltage setting at each position (7 points), as shown in Figure 12 (right).

We evaluated applied voltage and position dependence of timing resolution (Fig.13 left). The best timing resolution was 79.8 $\pm$ 1.8 ps at position No.5 when the applied voltage was 15.0 kV. This figure shows that the time resolution went the better with inclease applied voltage. However, it looks different structure at position No.2, and it can be considered that positron beam hit outside of the pad of MRPC.

We originally expected the best value of timing resolution would be at the center because it was considered that the signal is read out of both side of pad at the same time. However it turned out to be the opposite result. The applied voltage and position dependence of the efficiency are shown in Fig.13 right. The efficiency got the better with increase applied voltage. On the other hand, if the beam position got closer to the detector center, the efficiency got worse. These effect can be considered that the large reflection of the signal, because on the edge of the pad, the true pulse and reflected signal are almost close to each other, then the amplitude is bigger. But the beam hit in the center, true pulse and reflected signal are located next to each other, smaller amplitude and broader pulse would be formed by true pulse and reflected pulses, it causes worse timing resolution. Those results indicate the importance of the impedance matching among detector, cables, and pre-amplifier.

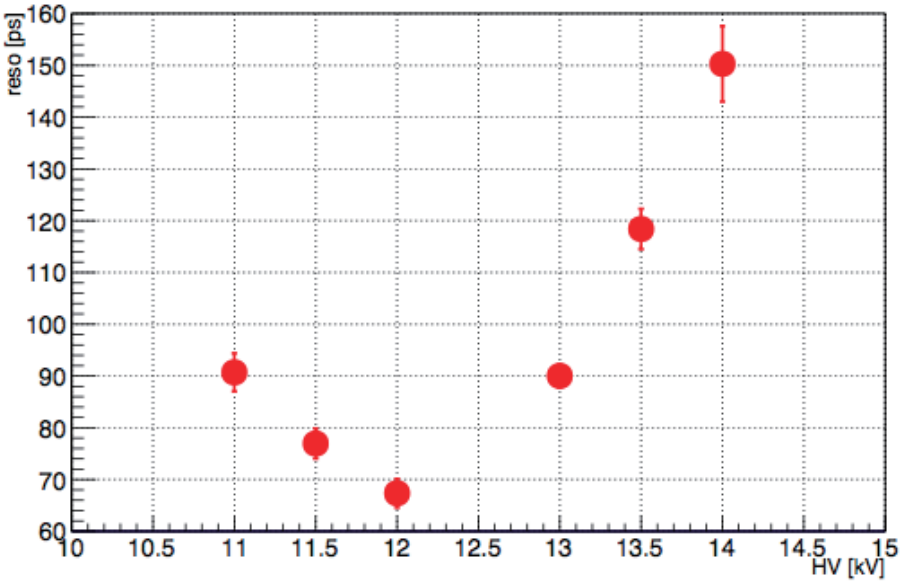


Fig.11. Timing resolution. The beam spot is the center.

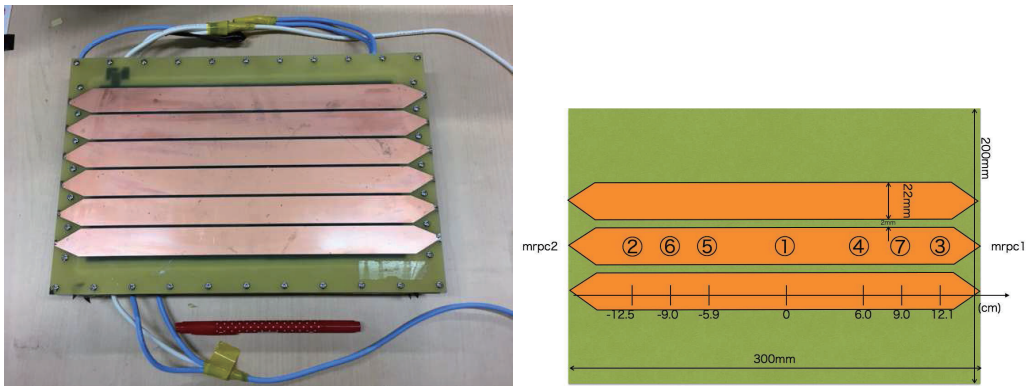


Fig.12. left:prototype of large MRPC , right:positron beam incident position

### 3.2.3 Small area MRPC with narrow pad width

The purpose of this study is to evaluate the pad width effect to the timing resolution and efficiency. In here, we used the single stuck MRPC. In this study, we collaborated with SONY Global Manufacture & Operation. They performed the electromagnetic field simulation. Based on the simulation results, it is possible to improve and optimize the wave shape quality of MRPC by changing the pad shape. We made the same type of MRPC as the simulation and performance beam test for those at ELPH.

In this experiment, we made 2 types of MRPCs. One is the reference counter whose width of the reading pad is 2.4 cm. This type is same shape of “Small area MRPC”, as we discussed before. We call it as “type A”, and the other is “type B” which has narrower width of reading pad to 1.2 cm than the type A.

We measured the efficiency using e.q.1. ”$N_{MRPC.th}$” is number of events in which the amplitude of

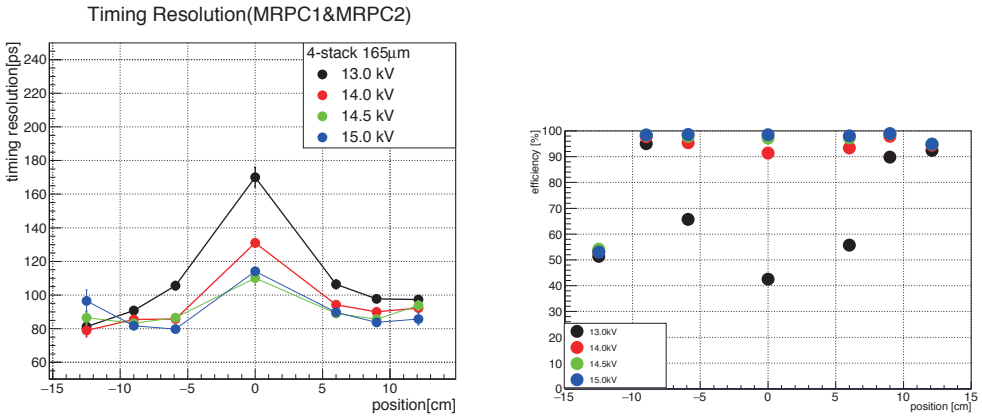


Fig.13. (left) position and applied voltage dependence of timing resolution, (right) position dependence of efficiency

MRPC exceeding certain threshold. In this analysis, the threshold value is set to 10 mV. "$N_{allevents}$" is the number of all trigger events. Both A and B types of MRPCs are obtained over 95% efficiency.

$$efficiency[\%] = \frac{N_{MRPC.th}}{N_{allevent}} \times 100 \tag{1}$$

We measured the rise times because it is one of the important elements. The quality of the waveform determines the timing resolution. We defined raise time as the time taken amplitude from 10% to 90%. Fig.14 shows a comparison of rise time for type A and type B. It shows the raise time of type B is faster than type A. This indicates that type B have a good wave shape compared to that for type A. So that it is expected that the timing resolution is better for type B. We measured the timing resolution: Type A is $85.4 \pm 2.4$ ps and type B is $78.9 \pm 1.8$ ps (Fig.15). We did not observed a clear difference on timing resolution by considering statistical uncertainties. The band width of pre-amplifier would not be optimized yet for the higher frequency (GHz). It is thought that the effect of timing resolution with different pad could be seen by using a high frequency pre-amplifier to catch a wider bandwidth.

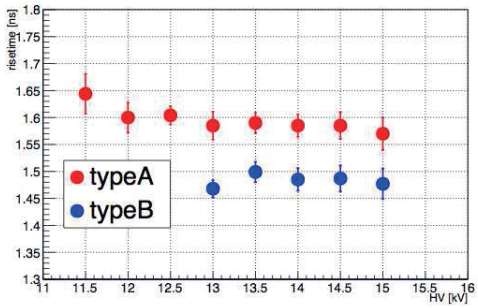


Fig.14. Applied voltage dependence of raise time. Comparison of type A and type B.

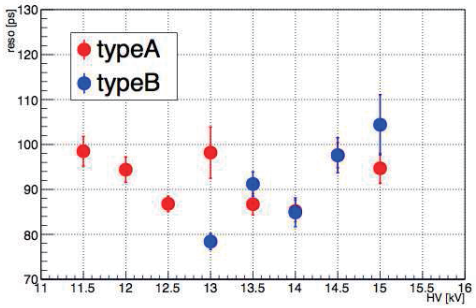


Fig.15. Applied voltage dependence of timing resolution. Comparison of type A and type B.

## Acknowledgment

We would like to acknowledge the ELPH accelerator staffs to provide the stable beam. This work was supported in part by Grants-in-aid for Research on Innovative Areas 2404, No. 24105002, KAKENHI Grant-in-aid No. JP15K13475, and Toray Science and Technology Grant.

## References

[1] J.K. Ahn *et al.*: Technical Design Report of J-PARC E42 experiment.

[2] DRS4 Manual, https://www.psi.ch/drs/DocumantationEN/manual_rev30.pdf

(ELPH Experiment：#2825:#2855)

# 大強度電子線形加速器を用いた $^{22}$Na、$^{24}$Na の生成

石久保宏平[1],上田惟行[1],小松巧[1],塚田暁[1],二宮慎吾[1],吉田千尋[1]

[1]東北大学電子光理学研究センター（982-0826 仙台市太白区三神峯 1-2-1）

# Production of $^{22}$Na and $^{24}$Na with a high-intensity electron beam

K. Ishikubo[1], T. Ueda[1], T. Komatsu[1], K. Tsukada[1],
S. Ninomiya[1], C. Yoshida[1]

[1]Research Center for Electron Photon Science, Tohoku University, Sendai, 982-0826

By irradiating the 50 MeV electron beam on 27Al target, 24Na and 22Na were generated via the photonuclear reaction. The amounts and spacial distributions of generated RIs were measured by NaI scintillation counters, Germanium detector, and the imaging plate.
The experimental results are compared with Geant4 simulation.

## §１.はじめに

本研究では電子光理学研究センターの所有する大強度線形加速器を用いて $^{27}$Al に 50MeV 電子ビームを照射し、$^{22}$Na および $^{24}$Na を生成した。NaI シンチレータと Ge 半導体検出器を用いて RI の生成量と半減期を測定し Ge 半導体検出器とイメージングプレートを用いて RI 生成分布をそれぞれ測定した。今回測定する放射線は、$^{22}$Na では 1.27MeV 及び β 崩壊からの陽電子が対消滅して生じる 0.511MeV の γ 線、$^{24}$Na では 2.75MeV と 1.37MeV の γ 線である。測定から得た結果との比較を Geant4 [1] を用いたシミュレーションで行った。

本研究では、２回のビーム照射を行った。１回目のビーム照射では RI の生成量を測定することを目的とした。２回目のビーム照射では Al ブロック内での放射化分布の広がりを調べることを目的とした。

## §２．生成量測定実験

今セクションでは１回目のビーム照射について説明する。

### 2.1. ビーム照射のセットアップ

電子ビーム照射による RI の生成量を調べる。ターゲットの厚さでの生成量の違いの検証のためにターゲットをそれぞれ 1cm 片の Al 板で厚さ 1mm を１枚、2mm を２枚とした。

セットアップは第１図になる。

今回のビーム照射では 50MeV 電子ビームをアベレージカレント 100μA で 5 時間照射した。

### 2.2. NaI シンチレータでの測定

ビーム照射直後から一週間の $^{24}$Na のレートの高いうちはコリメータを用いて $^{24}$Na を測定した。レートの下がった後は二つのシンチレータを用いてコインシデンス測定にて$^{22}$Na を測定した。それぞれのセットアップを第2図に示し、得られたヒストグラムを第3図にまとめる。

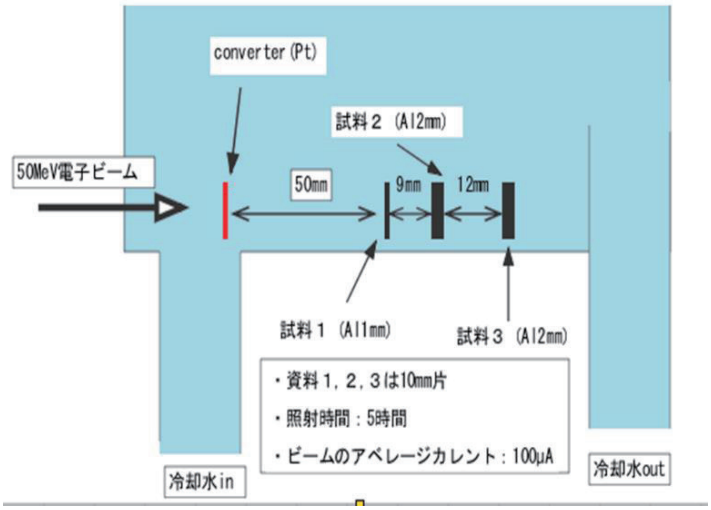


第１図　生成量測定のビームセットアップ

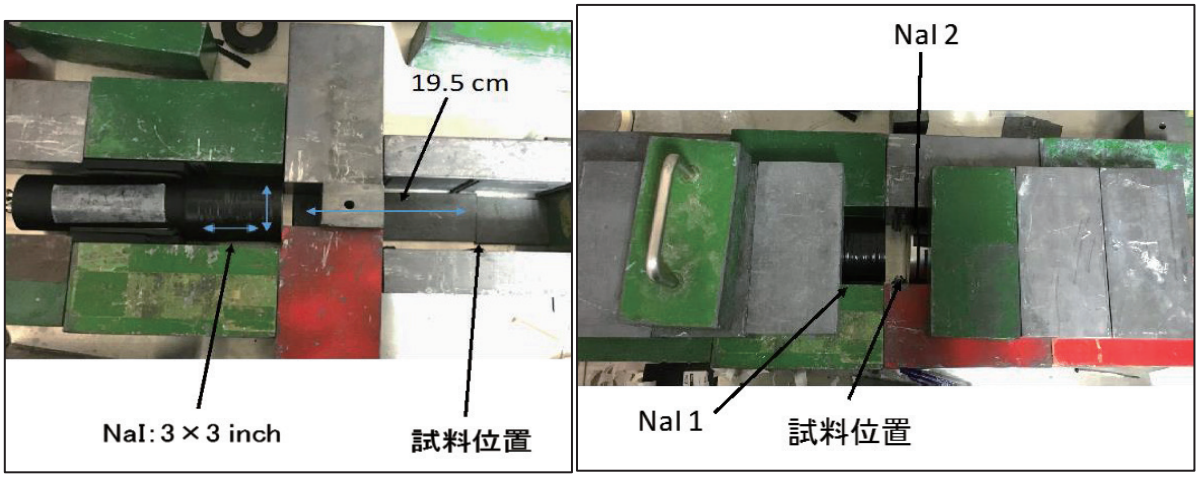


第２図　NaI シンチレータ測定のセットアップ（左 $^{24}$Na 測定、右 $^{22}$Na 測定）

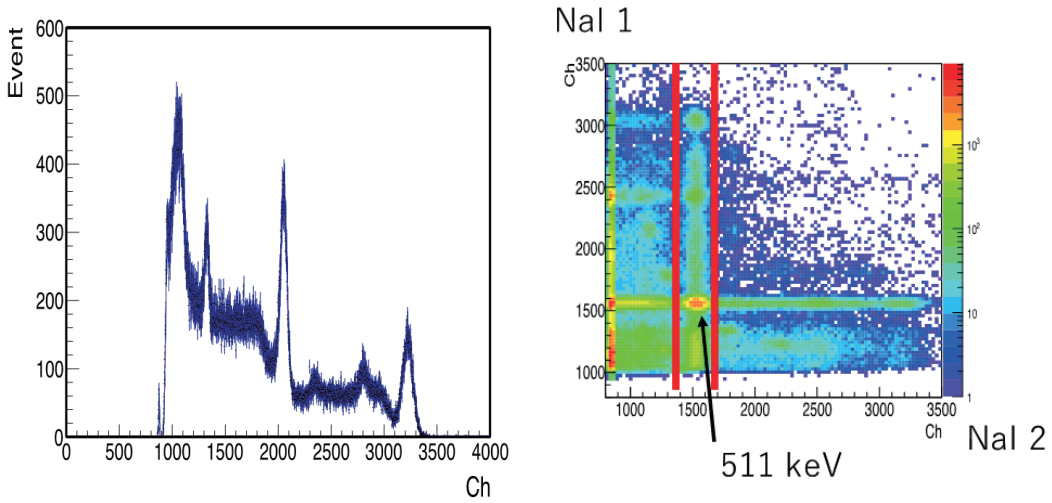


第3図　得られたヒストグラム（左 $^{24}$Na、右コインシデンス測定による $^{22}$Na）

2.3.　Ge 半導体検出器での測定

照射した 3 枚の Al 試料について、電子光理学研究センター第三実験室にある Ge 半導体検出器を用いて測定を行った。測定時間は約 10 分。測定のセットアップは第4図にまとめた。

試料の中心が Ge 結晶の中心とほぼ一致するように垂直方向に 5cm 離して置いた。
測定で得られたヒストグラムを第5図に示す。

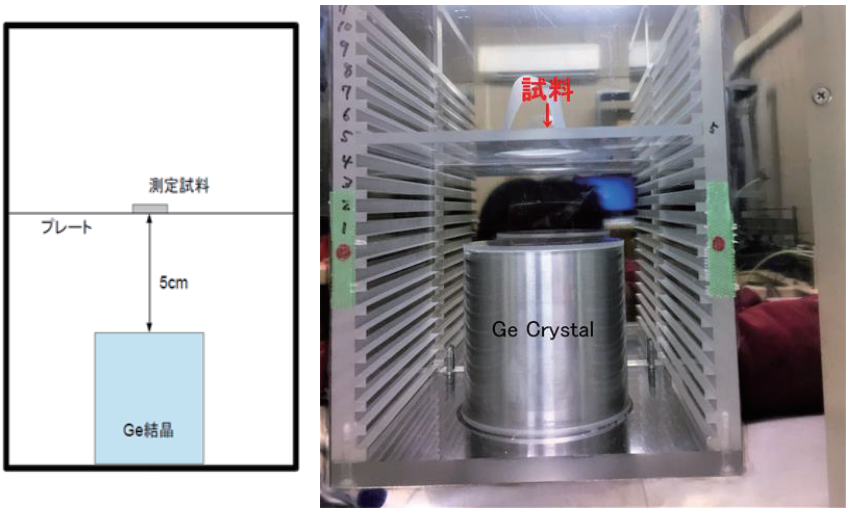


第4図　測定のセットアップ（左概略図、右実際のセットアップ）

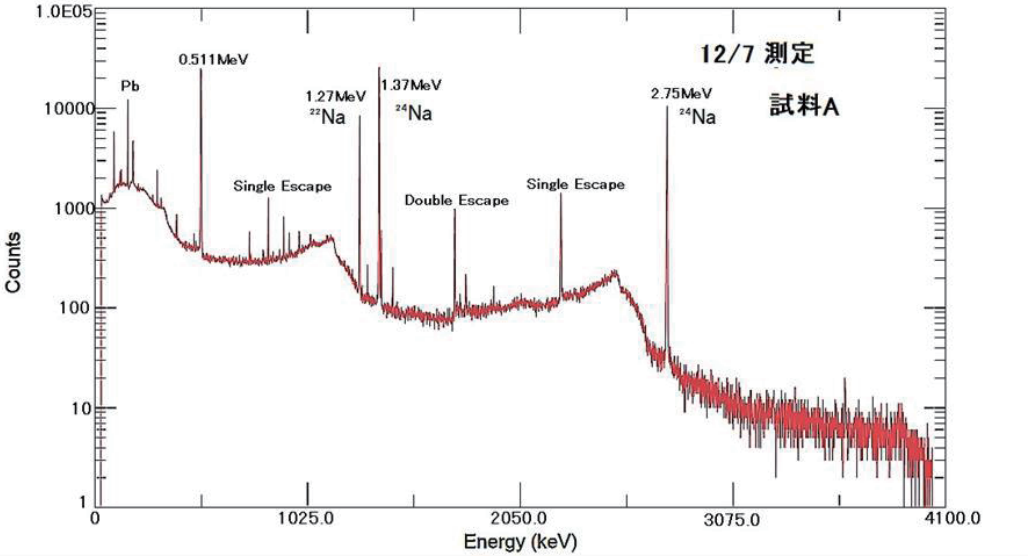


第 5 図　得られたヒストグラム

2.4. シミュレーション

RI の生成量は以下の式で見積もることができる。

$$Y = \sigma \cdot I_e \cdot R \cdot N_t \cdot T \qquad (1)$$

R は電子の数に対するγの数の比、$N_t$は標的の原子の数、T は照射時間である。Geant4 を用いて$I_e \cdot R$、つまり試料に照射されたγ線の数をシミュレーションした。断面積σは TALYS [2] を用いて計算したものを使用した。第 6 図に Talys で計算した断面積と、$^{24}$Na の断面積の文献値および 50MeV の電子が制動放射によって放出するγ線のエネルギー分布をまとめた。

TALYS コードとは A.J.Koing らによって開発され、2004 年に公開された汎用核反応理論計算コードである。直接反応、複合核反応、前平衡反応、核分裂反応に対する核反応模型が組み込まれている。

2.5. 測定結果とシミュレーションの比較

得られた測定結果とシミュレーションの結果を一つにまとめたものを $^{24}$Na については第 7 図に $^{22}$Na については第 8 図に示す

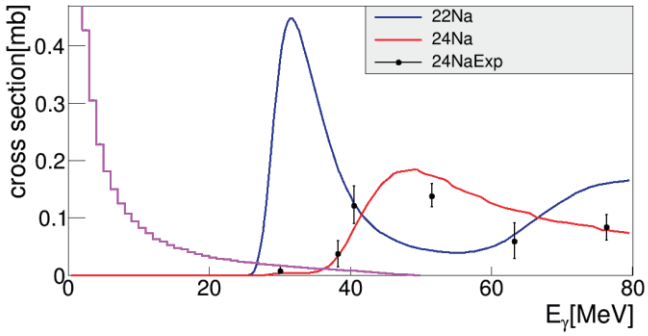


第 6 図　Talys による断面積と文献値［3］およびγ線のエネルギー分布
γ線のエネルギー分布の縦軸はスケールしてある。

2.5. 測定結果とシミュレーションの比較

得られた測定結果とシミュレーションの結果を一つにまとめたものを $^{24}$Na については第 7 図に $^{22}$Na については第 8 図に示す。

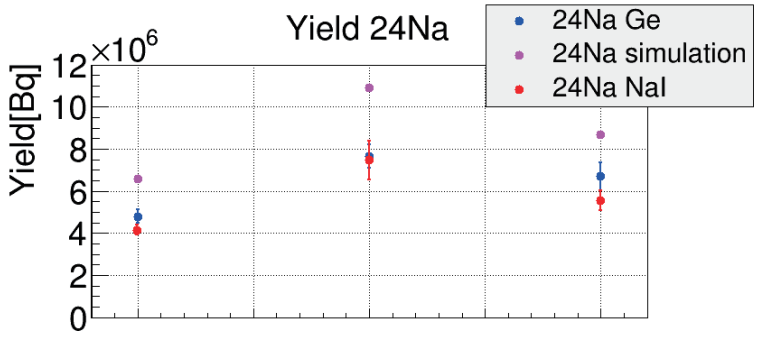


第 7 図　$^{24}$Na の生成量の比較(左から試料 1、2、3)

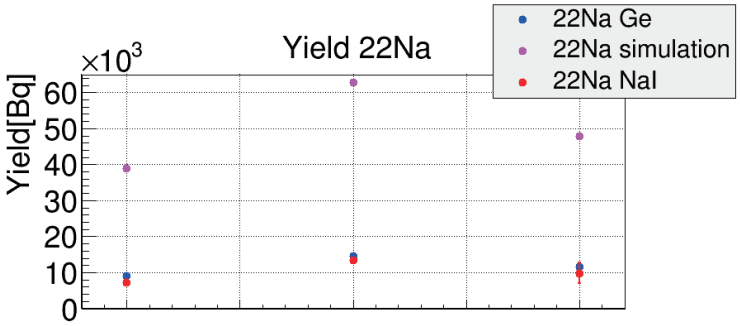


第 8 図　$^{22}$Na の生成量の比較(左から試料 1、2、3)

試料 1、2、3 の生成量の比はシミュレーションと測定でよく一致した。$^{24}$Na は測定値の 30%程大きく、$^{22}$Na は測定値の 4 倍程度となった。

Ge 半導体検出器と NaI シンチレータで測定した値は誤差の範囲で一致している。$^{24}$Na の生成量のシミュレーションでの値は測定値よりも 30%ほど大きかった。これは断面積を見てみると、TALYS で求めた断面積が文献値よりも大きくなっており、また、文献値の誤差も大きい。これらのことから、この差異は誤差の範囲内にあると考えられる。$^{22}$Na の生成量はシミュレーションでの値が測定値の 4 倍になった。これは断面積のエラーでは説明がつかないので Talys で計算した断面積が大きく見積もられすぎていると考えられる。

## §３．放射化分布測定実験

二回目のビーム照射では、放射化分布の広がりを調べるために、Al ブロックへのビーム照射を行った。

3.1. ビーム照射のセットアップ

ブロックの放射化分布を調べるために第 9 図のようなセットアップを作った。

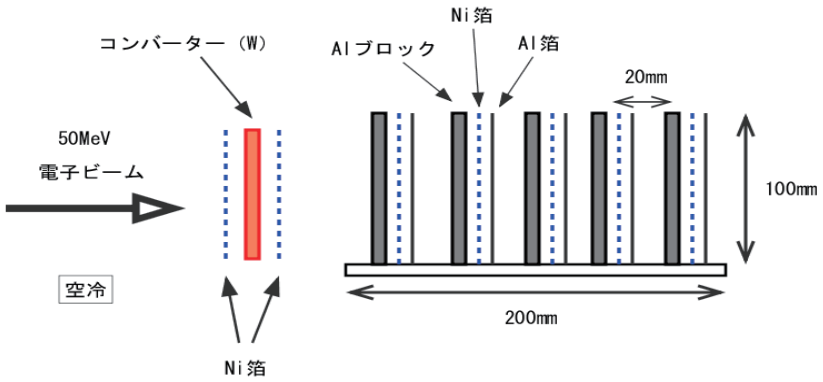


第 9 図　ブロック実験の概略図

このセットアップは Al ブロック（H 100 ㎜、W 100 ㎜、T 20 ㎜）を Al 板（H 10 ㎜、W 200 ㎜、T 200 ㎜）に幅 20 ㎜の隙間を空けてネジ止めし、ビーム下流側に Al 箔（H 100 ㎜、W 90 ㎜、0.05 ㎜）をクリップによって Al 板に固定した。

今実験では 50MeV 電子ビームを 1 時間このセットアップに照射し、イメージングプレートおよび NaI、Ge 検出器を用いて Al 箔の放射化分布を測定した。

3.2. 放射化分布測定

まず、Al 箔をイメージングプレートに露光し、東北大学サイクロトロン・ラジオアイソトープセンターの RI 棟 3 階の IP 室の現像機で現像を行った。その後 Al 箔を 1cm 片に切りビーム照射中心付近を Ge 半導体検出器で測定した。

得られた結果を第10図に示す。ここではビーム上流方向から置いた順に Al1−Al4 とした。

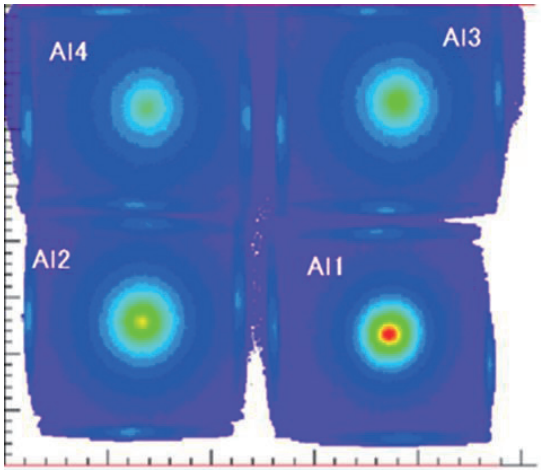


第10図　イメージングプレートで得られた結果

3.3. 測定結果とシミュレーション結果の比較

イメージングプレート、Ge 半導体検出器、シミュレーションでのビーム上流から見て 1 枚目の Al 箔の放射化分布を一つのグラフにプロットしたものを第１１図に示す。

シミュレーションの分布の半値幅は Ge 半導体検出器での半値幅の 1/2 程度となっている。また、イメージングプレートでの放射化分布は裾が広がっている。これらの原因は究明中である。

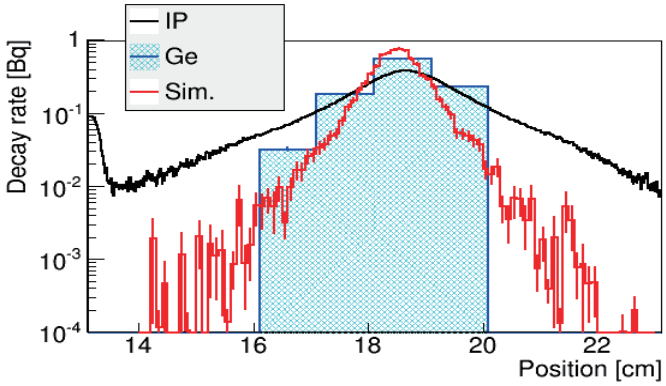


第１１図　放射化分布の広がり

§６．まとめ

大強度電子線形加速器を用いて $^{27}$Al 標的に電子ビームを照射し $^{24}$Na と $^{22}$Na を生成した。その生成量と分布を NaI シンチレーターと Ge 半導体検出器とイメージングプレートを用いて測定した。Geant4 を用いてシミュレーションを行い、その結果を測定値と比較した。

$^{24}$Na の生成量のシミュレーションでの値は Ge 半導体検出器での測定値より 30%ほど大きくなった。これは断面積のエラーの範囲内にあると考えられるので、シミュレーションは測定値をよく再現できていると言える。$^{22}$Na の生成量のシミュレーションでの値は Ge 半導体検出器での測定値の 4 倍程度となった。これは、断面積のエラーでは説明がつかないので、Talys で計算した断面積が大きすぎるのではないかと考えられる。

放射化分布の広がりは Ge 半導体測定値での測定値がシミュレーションでの値の 2 倍となり、イメージングプレートの分布は裾が広がっていた。これらの原因はいまだはっきりとわかっておらず、原因を究明中である。

参考文献

[1] Geant4 website: 〈http://geant4.cern.ch/〉
[2] TALYS website: 〈http://www.talys.eu/〉
[3] Soviet Physics JETP11(1960)783

(ELPH Experiment : #2840)

# Large Acceptance Multi-Purpose Spectrometer (LAMPS) Time Projection Chamber (TPC) Prototype Beam Test

H. S. Lee[1], Y. J. Kim[1], M. S. Ryu[1], and J. W. Lee[2]

[1]*Rare Isotope Science Project, Institute for Basic Science, Daejeon, 34047, Korea*
[2]*Department of Physics, Korea University, Seoul, 02841, Korea*

LAMPS is the nuclear science facility to study a nuclear equation of state via heavy-ion collisions at RAON. TPC is the main tracking detector of the LAMPS solenoid spectrometer to identify particle species and reconstruct the momentum of each track with high precision over a large acceptance. The LAMPS TPC prototype was made for 1/2 size of a real LAMPS TPC. We measured the drift velocity, diffusion and position resolution to understand the characteristics of the LAMPS TPC prototype by using a positron beam.

## §1. Introduction

### 1.1 Large Acceptance Multi-Purpose Spectrometer (LAMPS)

RAON is the rare isotope (RI) beam accelerator facility in Korea. The motivation of RAON is to understand the nuclear structure of exotic nuclei close to drip lines, the astrophysical processes and the detailed properties of dense nuclear matters. One of the nuclear science facilities at RAON is LAMPS for the study of a nuclear equation of state (EoS) via heavy-ion collision experiments. Using RI beams allows us to widely vary and control a neutron to proton ratio of the colliding system. Such a controlled experiment is possible to explore the isospin dependent part of nuclear matter EoS, known as symmetry energy, which is an important component of understanding the neutron star, supernova, nuclear synthesis and exotic nuclei near neutron drip lines.

At the end of the In-Flight separator, LAMPS will be located for completing an event reconstruction by detecting all the particles produced in heavy-ion collisions within a large acceptance angle to measure particle spectrum, yield, ratio and collective flow of pions, protons, neutrons, and intermediate fragments at the same time. LAMPS consists of a solenoid spectrometer and a forward neutron wall. A Time Projection Chamber (TPC) and a time-of-flight (ToF) detector will be placed inside cylindrical solenoid magnet of 0.5 T for charged particle tracking and particle identification. The forward neutron wall will be made of 8 layers of plastic scintillators for neutron tracking.

### 1.2 LAMPS TPC

LAMPS has TPC as a main tracking device in the solenoid spectrometer to identify particle species and reconstruct the momentum of each track with high precision over a large acceptance. Inside of TPC, micro patterned gas amplifiers such as triple stacks of Gas Electron Multiplier (GEM) are deployed. [1]

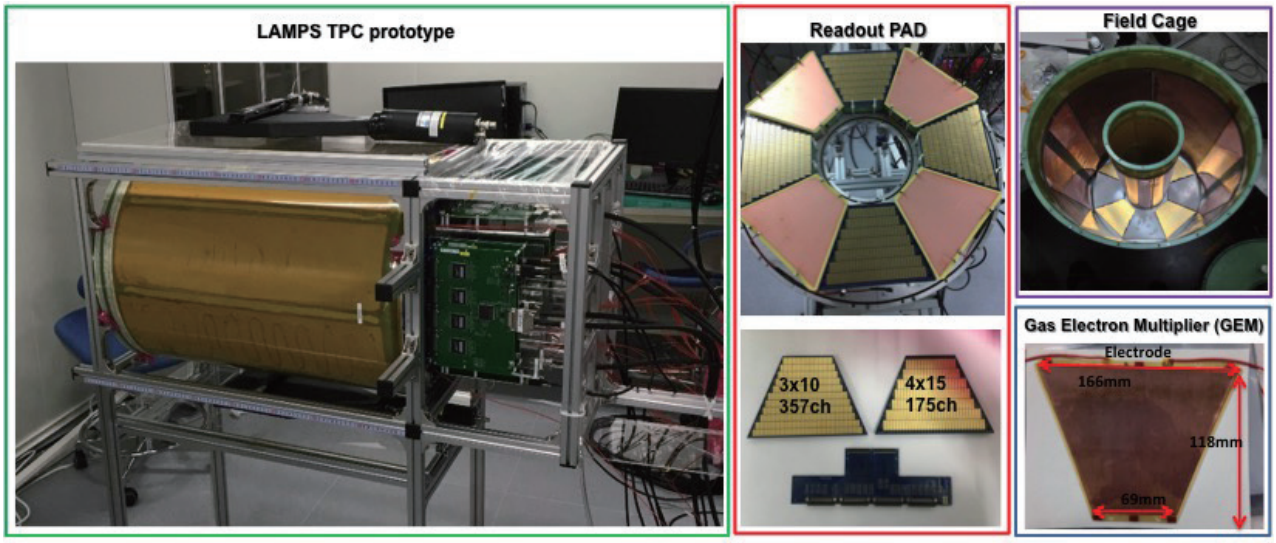


Fig.1. LAMPS TPC prototype.

The LAMPS TPC is cylindrical with a central axis lying on a beam direction. The length of a gas volume inside TPC is 1.2 m and its radius is 50 cm. In order to avoid gain saturation due to beam particles, the cylindrical hole with radius of 15 cm is made along the beam axis. The readout PAD is located at the end of the cylinder and is segmented into eight identical trapezoidal sectors in azimuthal angles. Each sector is equipped with three GEM foils for amplifying the charge signal which is composed by 2 mm gap between GEM foils. The nominal target position is a quarter of the total length of the gas volume (30 cm) from the upstream face of TPC to enlarge the geometrical acceptance at mid-rapidity. Therefore, TPC covers the range of $25^o$ to $126^o$ in the polar angle of a laboratory system.

The LAMPS TPC prototype was designed for 1/2 size of real LAMPS TPC in terms of an outer radius and a drift length but an inner radius of the cylindrical hole is the same to the real LAMPS TPC. The LAMPS TPC prototype will give us various information : drift velocity, performance of field cage, and position resolution of different readout PAD designs. Figure 1 shows the LAMPS TPC prototype, a field cage, readout PAD and a GEM. Two different designs of readout PADs ($3 \times 10$ mm$^2$, $4 \times 15$ mm$^2$) are installed.

## §2. Experiment

The purpose of this experiment is to understand the characteristics of the LAMPS TPC prototype with a positron beam. We measured a drift velocity by modulating an electric field of the field cage and the performance of two different readout PAD designs ($4 \times 15$ mm$^2$ and $3 \times 10$ mm$^2$), which were compared for two different gas mixtures : P-10 (Ar 90% + $CH_4$ 10%) and $ArCO_2$ (Ar 90% + $CO_2$ 10%).

Figure 2 shows an experiment setup at the ELPH beam line. The LAMPS TPC prototype is placed at the beam line and on the lab jack to change a beam injection height at TPC. To define beam trigger, 6 trigger counters are placed in the front and back side of the LAMPS TPC prototype. At the front, two

Fig.2. ELPH experiment setup.

scintillators whose size is 1 cm width are installed to define $1 \times 1$ cm$^2$ beam size. 4 cm scintillators are installed to make a trigger signal by passing the beam in the back of TPC. Two large scintillators whose size is $20 \times 20$ cm$^2$ are placed just in front and back side of TPC.

Two different PADs are installed in the LAMPS TPC prototype. We tested $4 \times 15$ mm$^2$ PAD in the LAMPS TPC prototype, and the other $3 \times 10$ mm$^2$ PAD was tested by using a small GEM test chamber next to the LAMPS TPC prototype as shown in Fig. 2.

A trigger signal is defined by the coincidence of 6 scintillators. We took VME data for scintillator counters and TPC data by using a different DAQ program at the same time. In order to synchronize two different DAQs, we made the gate signal with a trigger signal from scintillating counters, trigger ready from TPC DAQ and busy signal from TPC DAQ.

Figure 3 shows one example of beam event display on TPC. The top figures are raw signals of each PAD

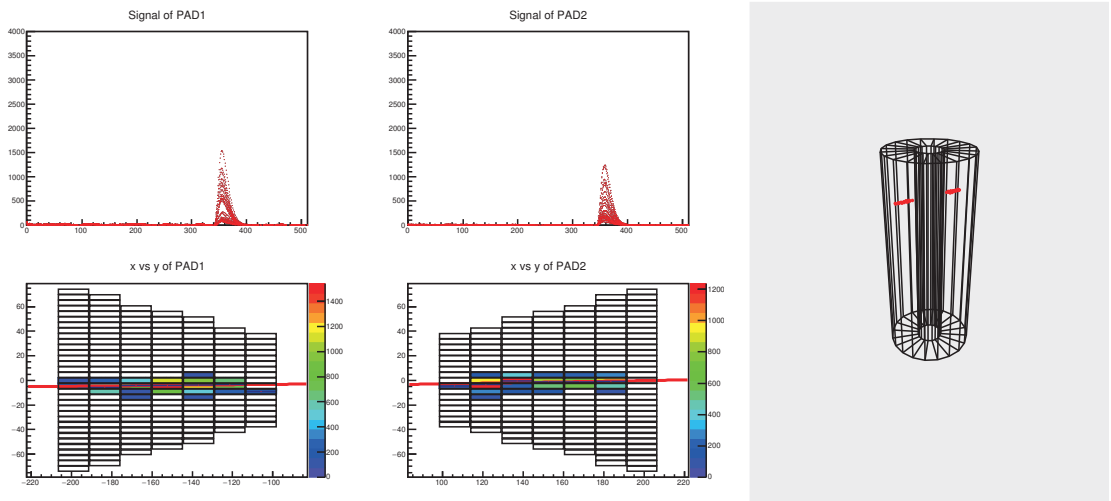


Fig.3. Event display of positron beam.

after TPC front-end electronics and the bottom figures show the beam tracking on the two PADs. Since the beam passes through the same height of the LAMPS TPC prototype, all signals of PAD are located at the same timing. Right figure shows 3 dimensional event display.

We have taken data for two different gases for 2 days. On the first day, we have tested with different electric field of the field cage from 115 V/cm to 155 V/cm with P-10 gas. Also, we varied a beam injection height (20.24 cm, 35.24 cm and 50.24 cm) in the LAMPS TPC prototype. On the next day, we have tested with $ArCO_2$ gas by changing the beam injection height. In this case, we fixed an electric field at 170 V/cm.

## §3. Analysis and Result

### 3.1 Drift Velocity

TPC is a very good 3 dimensional tracking detector. $X$ and $Y$ positions are defined by the readout PAD positions. $Z$ position is defined by the drift time of electron along the field cage. We measured a drift velocity as a function of 5 electric fileds (115 V/cm $\sim$ 155 V/cm). To calculate a drift velocity, we measured 3 different beam injection heights in the LAMPS TPC prototype. Figure 4 shows the measured drift velocity as a function of electric fields. Red points are the measured values by using the positron beam at ELPH. Blue one is from the muon test in the lab and black is based on garfield++ calculation from the gas table. In the P-10 gas, the maximum drift velocity is 5.26 cm/$\mu$s with positron beam at an electric field of 155 V/cm. The drift velocity of $ArCO_2$ gas is 1.07 cm/$\mu$s at an electric field of 170 V/cm. Since a real LAMPS TPC will have 120 cm field cage, the drift time with a full range will be around 23 $\mu$s if we use P-10 gas with 155 V/cm electric field. Since we need the drift velocity faster than 6 cm/$\mu$s in order to record complete information within time range of electronics which cannot be achieved using P-10, we tested P-20 (Ar 80% + $CH_4$ 20%) gas mixture. As shown in Fig. 4, by using P-20 gas, we could measure the drift velocity of 6.7 cm/$\mu$s at the 205 V/cm electric field.

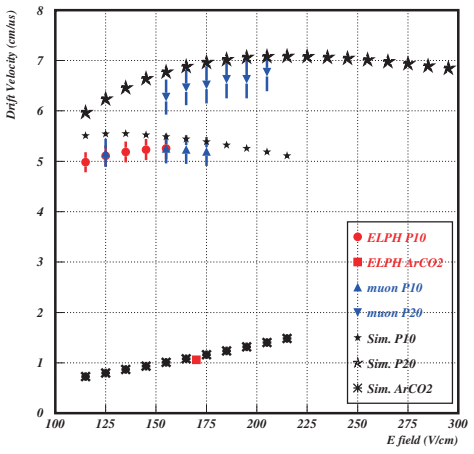


Fig.4. Drift Velocity as a function of electric field.

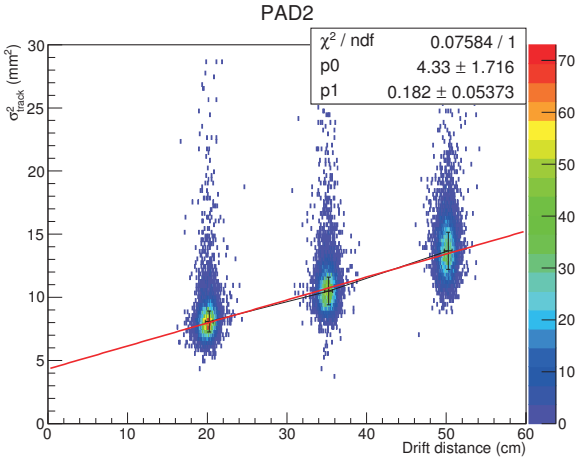


Fig.5. Square of charge cloud width as a function of position beam height.

### 3.2 Diffusion

One of the most important characteristics of TPC is the position resolution. The position resolution is determined by various parameters of TPC : gas diffusion, PAD size and so on. Since the diffusion coefficient represents a spread of the electron cloud, the diffusion coefficient of the chosen gas is the most important factor to determine the position resolution.

The spread of the charge cloud increases along the drift distance ($Z$) due to collisions with gas atoms and molecules. Therefore, the width of the track ($\sigma_{\text{track}}$), which is perpendicular to the track, is a function of drift distance $Z$ : [2]

$$\sigma_{\text{track}}^2 = D^2 Z + \sigma_0^2 \tag{1}$$

where $D$ is a transverse diffusion coefficient and $\sigma_0$ is a coefficient due to the amplification system (triple GEM system of the LAMPS TPC prototype).

Figure 5 shows the width of the charge cloud ($\sigma_{\text{track}}$) as a function of the drift distance ($Z$) at an electric field of 155 V/cm. In the linear fitting, the slope (p1) corresponds to a transverse diffusion coefficient. The diffusion coefficient was obtained as 426 $\mu$m/$\sqrt{\text{cm}}$.

### 3.3 Position resolution

We have tested two different size PADs : 4 $\times$ 15 mm$^2$ in the LAMPS TPC prototype and 3 $\times$ 10 mm$^2$ in the small GEM test chamber. Figure 6 shows the residual distribution along the distance between the beam track and the hitting position on the PAD. We have measured position resolutions for the P-10 gas condition. The left distribution is for the 4 $\times$ 15 mm$^2$ PAD and its position resolution is 605.6 $\mu$m. The right one is for the 3 $\times$ 10 mm$^2$ PAD and 227.5 $\mu$m position resolution.

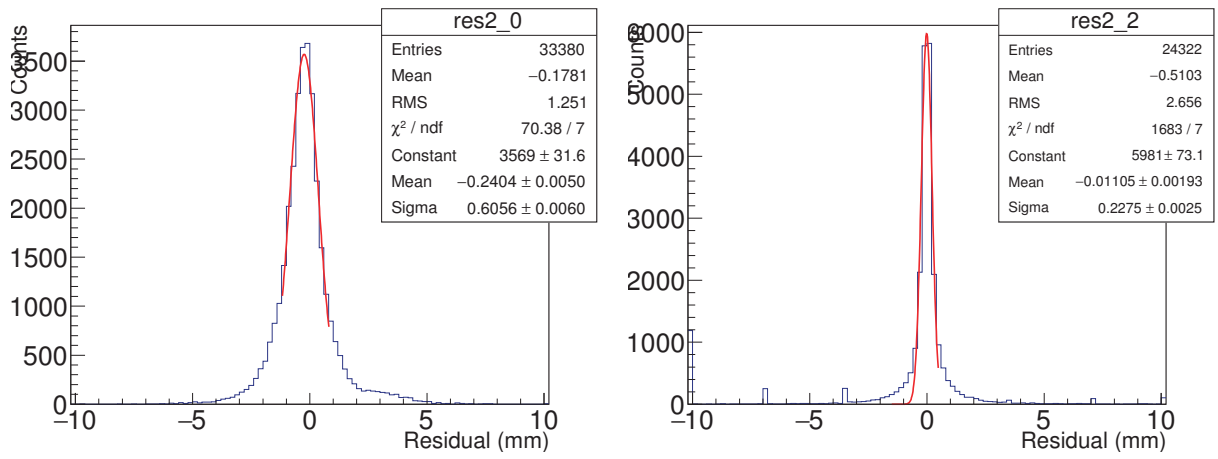


Fig.6. Residual distribution of PAD 4 $\times$ 15 mm$^2$ (left) and 3 $\times$ 10 mm$^2$ (right).

## §4. Summary

LAMPS is one of the experimental facility for nuclear physics at RAON. We have been developing the LAMPS TPC which is a main tracking detector of the LAMPS spectrometer. The LAMPS TPC

prototype was developed to study a design of the LAMPS TPC with triple GEM system. We have tested the LAMPS TPC prototype with positron beam at ELPH. The maximum drift velocity of P-10 gas is 5.26 cm/$\mu$s at 155 V/cm electric filed and $ArCO_2$ gas is 1.07 cm/$\mu$s at 170 V/cm. The drift velocity was tested using a P-20 gas in order to achieve a requirement of the TPC elctronics and is obtained with 6.7 cm/$\mu$s. Transverse diffusion coefficient is 426 $\mu$m/$\sqrt{\text{cm}}$ with P-10 gas. Position resolutions are 605.6 $\mu$m for $4 \times 15$ mm$^2$ PAD and 227.5 $\mu$m for $3 \times 10$ mm$^2$, respectively.

## Acknowledgment

The authors would like to thank ELPH accelerator staff for providing the stable beam. We deeply appreciate M. Miyabe and H. Shimizu for supporting beam test. This work was supported by the Rare Isotope Science Project and by the Institute for Basic Science, with funding provided by the Ministry of Science and the National Reference Foundation (NRF) of Korea (2013M7A1A1075765).

## References

[1] F. Sauli : Nucl. Instrum. Methods. **A805** (2016) 2.

[2] R.K. Carnegie *et al.*: Nucl. Instrum. Methods. **A538** (2005) 372.

(ELPH Experiment : #2864)

# Performance study of prototype hodoscope for new photon tagging system STB TaggerIIs

M.Iwasa[1], M.Sasaki[1], Y.Inoue[2], T.Ishikawa[2], H.Kanda[3], J.Kashiwagura[1], M.Miyabe[2], N.Muramatsu[2], T.Ono[1], M.Sasagawa[2], Y.Seki[1], R.Shirai[2], H.Shimizu[2], Y.Sugihara[1], Y.Tajima[1], A.O.Tokiyasu[2], H.Wauke[1], and H.Y.Yoshida[1]

[1]*Department of Physics, Yamagata University, Yamagata, 990-8560*
[2]*Research Center for Electron Photon Science, Tohoku University, Sendai, 982-0826*
[3]*Research Center for Nuclear Physics, Osaka University, Ibaraki, 567-0047*

A new photon tagging system that called STB TaggerIIs, is developed in progress at ELPH for FOREST experiments. STB TaggerIIs consists of MWDC and hodoscope. The hodoscope can specify the generated time of photons with good resolution. We made a prototype hodoscopes and measured the time resolution using positron beam in December 2016 and February 2017. The time resolutions of all prototypes with amplifier were less than 190 ps. From this results, we decide to use the single-sided readout system of the STB TaggerIIs hodoscope.

## §1. Introduction

We are developing a new photon tagging system (STB TaggerIIs) for FOREST experiments. FOREST experiments are used photon beam. When inserting carbon fiber into the circulating electrons in BST electron ring, bremsstrahlung radiation occurs and photon beam are generated. The photon tagging system is used to identify a photon and and determines the energy. Fig. 1 is a illustration of STB TaggerIIs. Recoil electrons are bent inwards by the bending magnet. STB TaggerIIs detects recoil electrons and tags a photon beam. The energy of a photon is given by the following equation. [1].

$$E_\gamma = e - e_{recoil} \tag{1}$$

Here, $e$, $e_{recoil}$, and $E_\gamma$ are the energy of the circulating electrons, recoil electrons and photons.

STB TaggerIIs consists of a MWDC and a hodoscope. The MWDC is worked to detect recoil electron trajectories and calculates momentum with high accuracy. The hodoscope is worked to separate a bunch of photon beams with good time resolution. The interval time of the beam bunch is 2 ns, and in order to identify the beam bunch, the time resolution of the hodoscope is less than 200 ps. To archive the requirement, we made prototypes of the hodoscope and measured the time resolution.

### 1.1 Hodoscope

The prototype hodoscopes are combination of Multi Pixel Photon Counter (MPPC) and plastic scintillator. The hodoscope must not be affected by the magnetic field, because it is installed in the bending

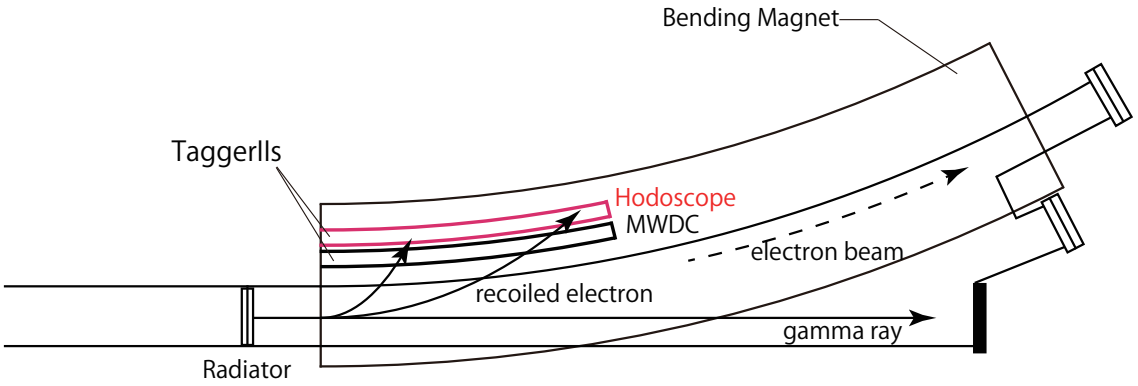


Fig.1. Illustration of TaggerIIs.

magnet. The hodoscope has 60 scintillators. The size of the scintillators are 5–30 mm width, 30 mm height, 5 mm thickness. In order to make the same counting rate and below 500kHz, the width of scintillators were decided from 5 mm to 30 mm at intervals of 5 mm. Therefore the width of scintillator to detect high energy recoil electron is 5 mm, and to detect low energy is 30 mm. The height of the scintillators are 30 mm, these are as same as the window height of the MWDC. The reflection sheets of the scintillators are used Teflon.

## §2. Measurement of time resolutions

### 2.1 Experimental condition

The experiment was carried out at ELPH positron beam line in December 2016 and February 2017. We studied 5 mm and 30 mm width scintillator. We compared with single-sided and dual-sided readout. 5 mm width scintillators were studied single-sided readout, dual-sided individual readout, and dual–sided sum readout.(Fig.2) 30 mm width scintillator was studied dual-sided individual readout with and without amplifier. The readout modules were one MPPC for 5 mm width scintillators, and parallel connected six MPPCs for 30 mm width scintillators. Applied voltage of MPPC were changed from 55.5 V (break down voltage + 3 V) to 60.5 V at intervals of 1 V. Threshold were studied 10 mV (without amplifier) , 50 and 100 mV ( with amplifier).

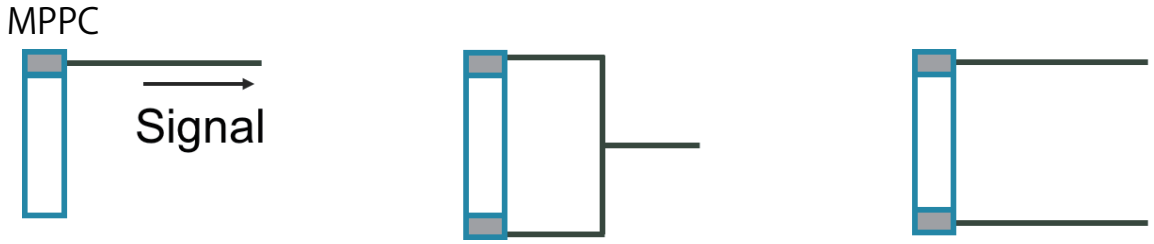


Fig.2. Left : single–sided readout. Middle : Dual–sided sum readout. Right : dual–sided individual readout.

### 2.2 Setup

Fig. 3 shows the experiment set up. T0 is 5 mm × 20 mm × 20 mm plastic scintillator with single photomultiplier readout to use for trigger start counter. T1 is 5 mm × 50 mm × 50 mm plastic scintillator with dual-sided photomultiplier readout to measure time. The prototype hodoscopes are set between T0 and T1. The signal from hodoscope divided into two lines. One enters into an ADC module through a cable delay, the other enters into TDC module. The trigger is coincidence of T0 and T1. Fig. 4 shows logic data taking system for the measurement and Tabel 1 shows the specification of counters.

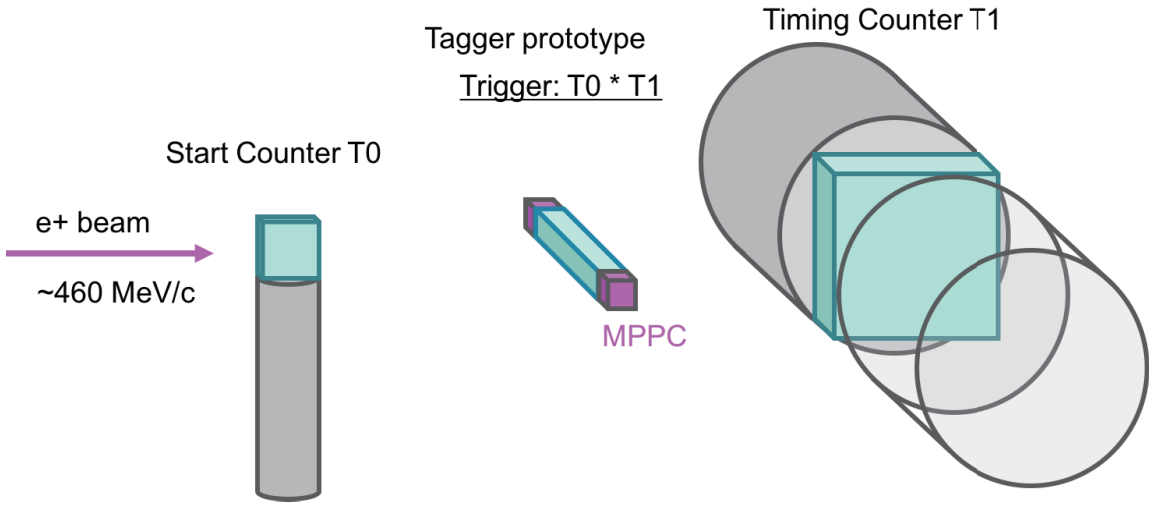


Fig.3. Set up of the measurement.

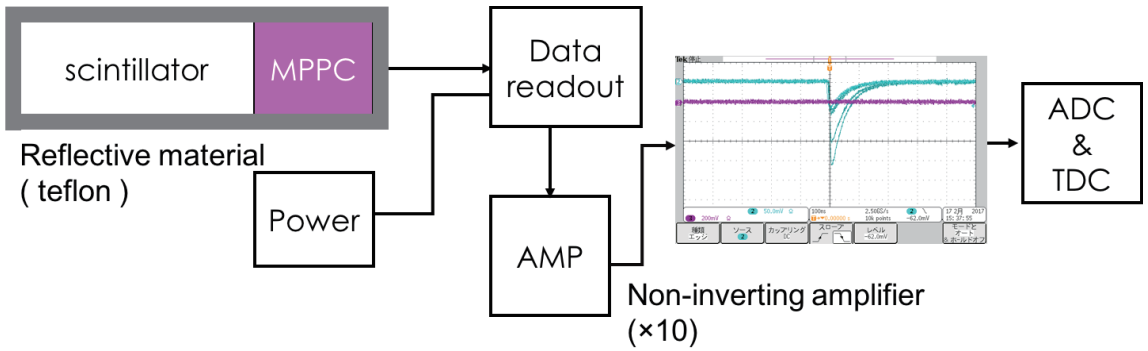


Fig.4. Schematic illustration of the data taking system.

Table 1. Characteristics of the counters.

| Counter | Type number | Operating voltage(max) [V] | Scintillator size [mm$^3$] |
|---|---|---|---|
| Start Counter T0 | R4125DMOD | 1500 (1800) | 5(W)×20(H)×20(T) |
| Timing Counter T1 | H6410 | 2000(2700) | 5(W)×50(H)×50(T) |
| MPPC | S13360-3050PE | 55.5 | 5(W)×30(H)×5(T) , 30(W)×30(H)×5(T) |

# §3. Results

## 3.1 ADC correcion

For ADC correction, the mean and error of TDC data is made by each bin of ADC, and fitted with correction function. The correction function is as follows.

$$T = p_0 + \frac{p_1}{\sqrt{ADC}} \tag{2}$$

Fig. 5 shows results of that.

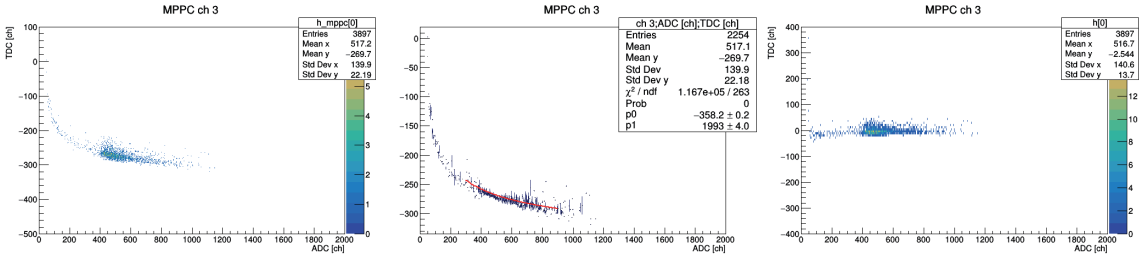


Fig.5. A correlation plot of TDC and ADC. Left: Before correction. Middle : Profile plot and fitting result. Right : After correction.

## 3.2 Time resolutions

After time correction, the time resolutions of prototype scintillators are obtained. Fig. 6 shows the results of 5 mm wide scintillator.

Table 2 and 3 show the time resolution with same bias voltage 56.5 V. The time resolutions of dual–sided sum readout are about 150 ps, better than single–sided readout. But both results are less than 190 ps, and lower than required resolution 200 ps. The time resolutions without amplifier, does not change in any readout method.

These are around 170 ps, and are shown in Fig. 7.

Without AMP, the sum read out in parallel from both sides and the average for each read and time are the same time resolution. Both time resolutions are around 170 ps. Figre 7 represents it.

Table 2 shows the rime resolution with the same bias. Here, we show data of 56.5 V (operating voltage +1 V) where fitting worked well for any data.

Table 2. The time resolution of 5 mm width scintillator with amplifier (bias voltage=56.5 V)

| Threshold [mV] | 100 | | 50 | |
|---|---|---|---|---|
| Readout | single–sided | dual–sided sum | single–sided | dual–sided sum |
| Time resolution [ps] | 186±4 | 149±6 | 172±4 | 157±6 |

## 3.3 Bias voltage dependence of time resolution

Fig.8–10 shows the the bias voltage dependency of the time resolution. Fig.8 shows the results of 5mm width scintillator with amplifier, and Fig.9 shows without amplifier. The time resolutions are worse

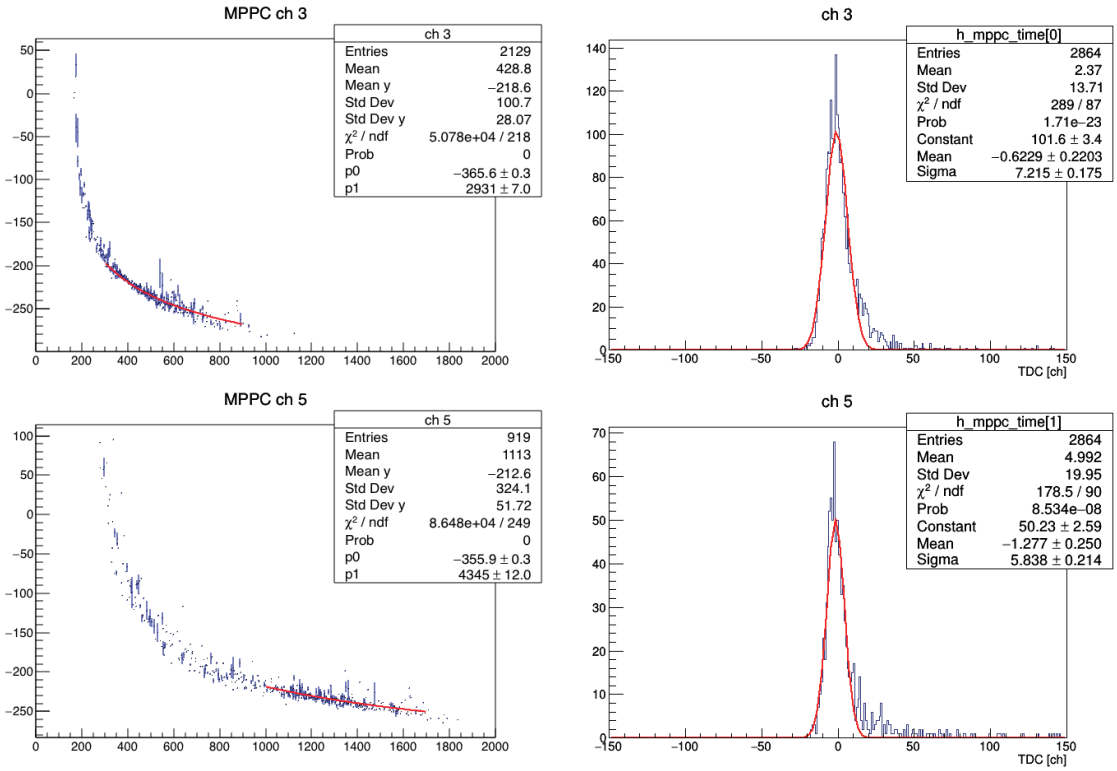


Fig.6. Left 2D histograms are the profile plot, and right histograms are time resolution. Uppers are the results of single–sided readout, and lowers are dual–sided sum readout. (Uppers : TDC 1 ch = 25.59 ps. Lowers : TDC 1 ch = 25.56 ps)

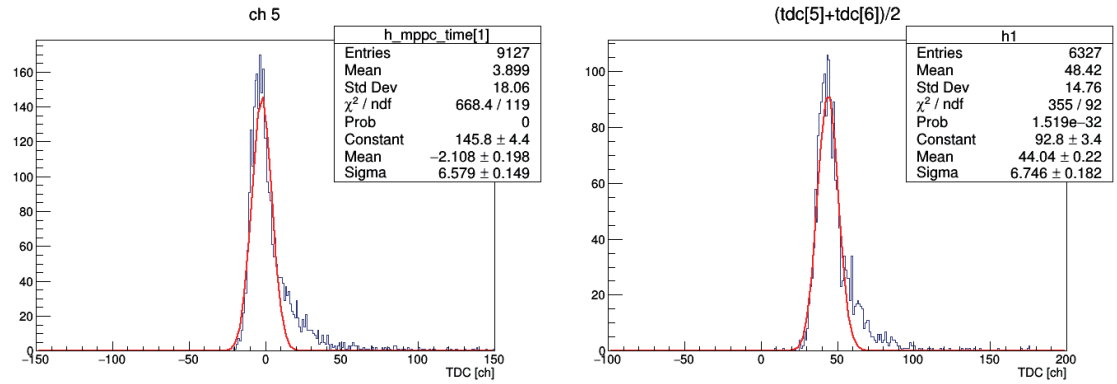


Fig.7. The time resolutions of dual-sided sum readout (left) and individual readout average (right) without amplifier, the thresholds are 10 mV.

Table 3. The time resolution of 5 mm width scintillator without amplifier (bias voltage=56.5 V)

| Threshold [mV] | 10 | | | | |
|---|---|---|---|---|---|
| Readout | single–sided | dual–sided | | | |
| | | sum | individual | | |
| | | | average | right | left |
| Time resolution [ps] | 161±2 | 168±4 | 172±5 | 203±6 | 236±6 |

Table 4. The time resolution of 30 mm width scintillator.

| Threshold [mV] | 100 | 10 |
|---|---|---|
| amplifier | with amplifier | without amplifier |
| Time resolution [ps] | 165±4 | 233±6 |

near the operating voltage (breakdown voltage +3 V = 55.5 V) . The other side, the time resolutions are slightly worse that the bias voltage is over the operating voltage + 3 V. FIg.10 shows the time resolution of 30 mm width scintillator. To satisfy the requirement, the readout of 30 mm width scintillator is needed amplifier.

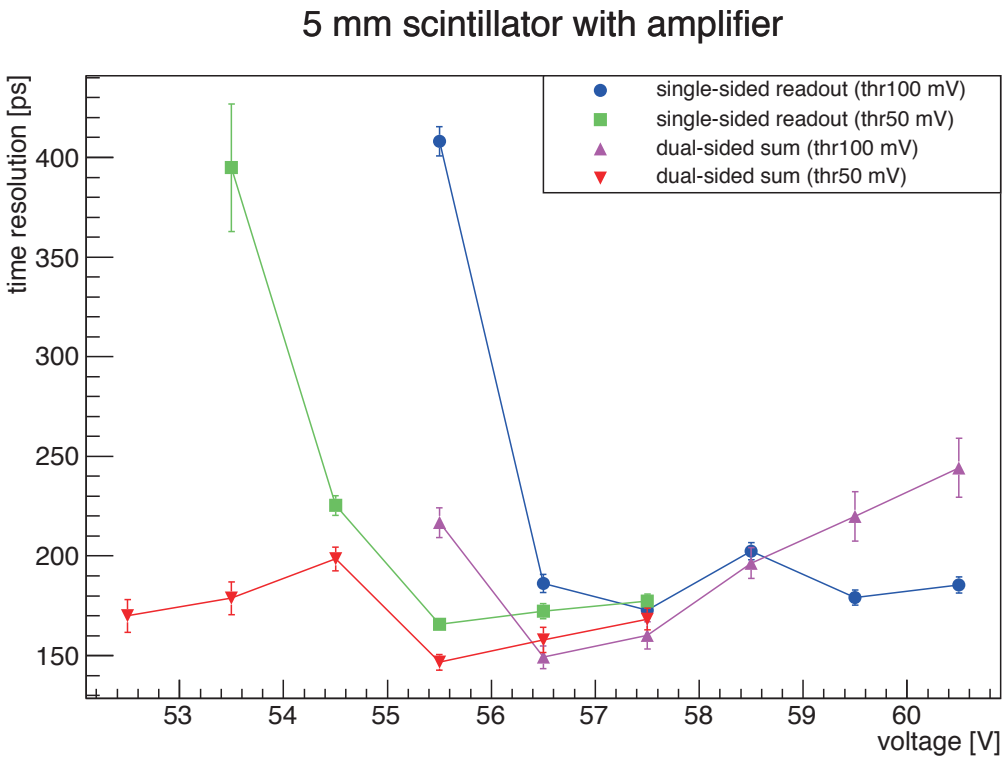


Fig.8. The bias voltage dependence of 5 mm width scintillator with amplifier.

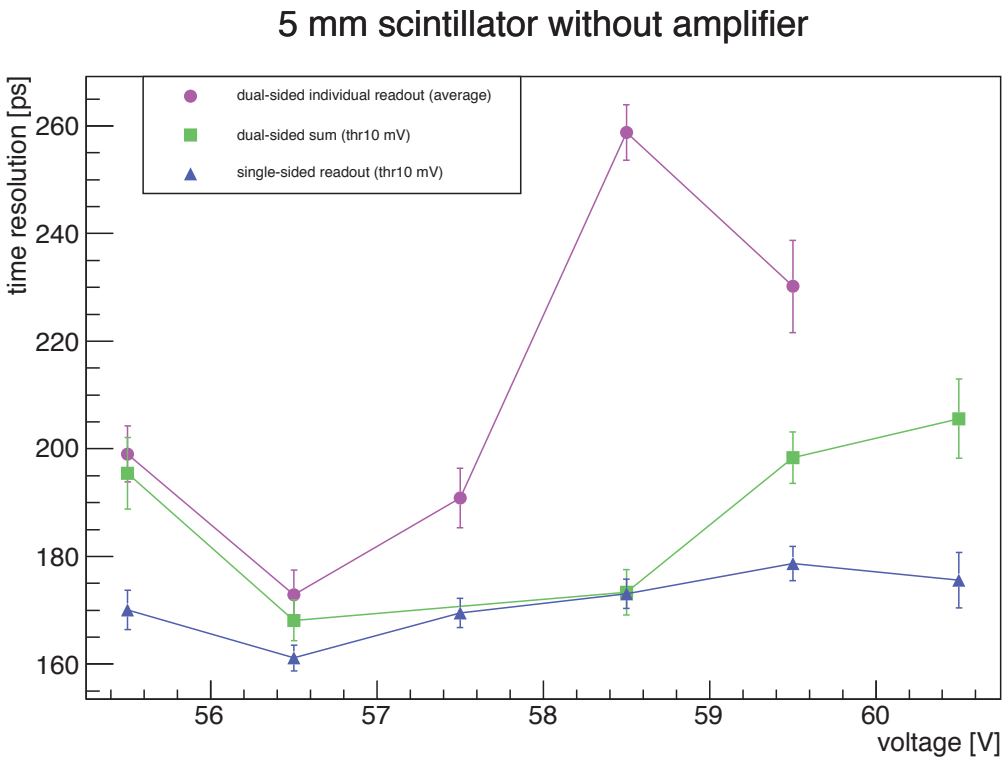


Fig.9. The bias voltage dependence of 5 mm width scintillator without amplifier.

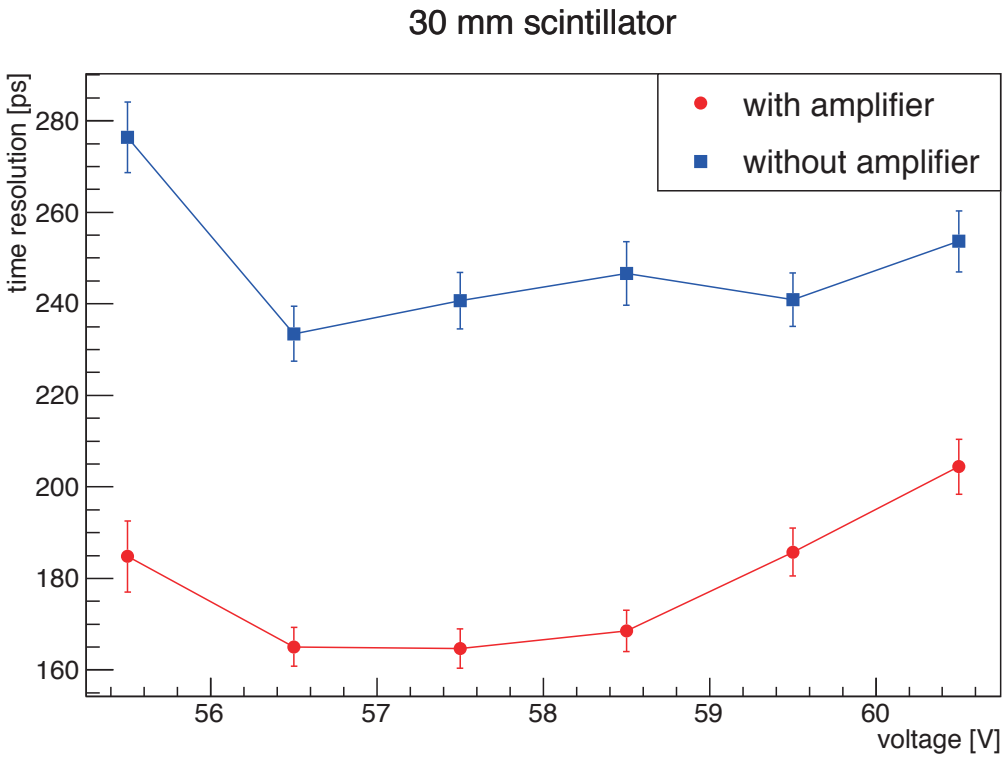


Fig.10. The bias voltage dependence of 30 mm width scintillator.

## §4. Summary

The new photon tagging device, STB TaggerIIs is developed in ELPH. This device consists of MWDC and hodoscope. The requirement of the hodoscope is that the time resolution is less than 200 ps. We made prototype hodoscope from plastic scintillator and MPPC. We studied three types of signal readout methods, single–sided readout, dual–sided individual readout, and dual–sided sum readout. And we compared each readout method with and without amplifier. The time resolution with dual–sided sum readout is equivalent to dual–sided individual readout. In addition, we compared the time resolution with AMP present and without AMP. The time resolutions of all situation with amplifier are less than required resolution, 200 ps. As a result, we decide the readout system of STB TaggerIIs hodoscope is used single–sided readout.

## Acknowledgment

The authors would like to thank our collaborators in ELPH for technical assistance with the experiments.

## References

[1] M. Sasaki *et al.*: ELPH Annual Report 2015 (2016) 45.

# Photon beam asymmetry measurement for the $\eta$ photoproduction at SPring-8 BGOegg experiments

Norihito Muramatsu[1], Toshikazu Hashimoto[2], Jung Keun Ahn[13], Wen-Chen Chang[5], Jia-Ye Chen[6], Schin Daté[4], Toshiyuki Gogami[3], Hiroya Goto[3], Hirotomo Hamano[3], Qing Hua He[1], Kenneth Hicks[7], Toshihiko Hiraiwa[3], Yuki Honda[1], Tomoaki Hotta[3], Hiroyuki Ikuno[3], Yosuke Inoue[1], Takatsugu Ishikawa[1], Igal Jaegle[8], Ja Min Jo[13], Yuuto Kasamatsu[3], Hitoshi Katsuragawa[3], Satoshi Kido[1], Yukiyoshi Kon[3], Shinichi Masumoto[9], Yuji Matsumura[1], Katsumasa Miki[12], Manabu Miyabe[1], Keigo Mizutani[2], Taiki Nakamura[12], Takashi Nakano[3], Masayuki Niiyama[2], Yuki Nozawa[2], Yuji Ohashi[4], Haruo Ohkuma[4], Hiroaki Ohnishi[10,3], Takeshi Ohta[3], Masaya Oka[3], Kyoichiro Ozawa[11], Mizuki Sasagawa[1], Takuya Shibukawa[9], Hajime Shimizu[1], Rintaro Shirai[1], Ken'ichiro Shiraishi[1], Yorihito Sugaya[3], Mizuki Sumihama[12], Shinsuke Suzuki[4], Shintaro Tanaka[3], Atsushi Tokiyasu[3], Natsuki Tomida[2], Nam Tran[3], Yusuke Tsuchikawa[1], Hirohito Yamazaki[1], Ryuji Yamazaki[1], Yuka Yanai[3], Tetsuhiko Yorita[3], and Masaru Yosoi[3]

[1]*Research Center for Electron Photon Science, Tohoku University, Sendai, Miyagi 982-0826, Japan*
[2]*Department of Physics, Kyoto University, Kyoto 606-8502, Japan*
[3]*Research Center for Nuclear Physics, Osaka University, Ibaraki, Osaka 567-0047, Japan*
[4]*Japan Synchrotron Radiation Research Institute (SPring-8), Sayo, Hyogo 679-5198, Japan*
[5]*Institute of Physics, Academia Sinica, Taipei 11529, Taiwan*
[6]*National Synchrotron Radiation Research Center, Hsinchu 30076, Taiwan*
[7]*Department of Physics and Astronomy, Ohio University, Athens, OH 45701, USA*
[8]*University of Hawaii at Manoa, Honolulu, HI 96822, USA*
[9]*Department of Physics, University of Tokyo, Tokyo 113-0033, Japan*
[10]*RIKEN Nishina Center, Wako, Saitama 351-0198, Japan*
[11]*Institute of Particle and Nuclear Studies, High Energy Accelerator Research Organization (KEK), Tsukuba, Ibaraki 305-0801, Japan*
[12]*Department of Education, Gifu University, Gifu 501-1193, Japan*
[13]*Department of Physics, Korea University, Seoul 02841, Republic of Korea*

The single $\eta$ photoproduction from a proton target is a good probe to study the $N^*$ resonances which include $s\bar{s}$ content. Since the isospin of the $\eta$ meson is zero, it does not couple with $\Delta^*$ resonances. Usually the $N^*$ resonance search is done by measuring the total cross section. However, the excited resonance states typically have large widths, and they may be overlapped with the possible influence of

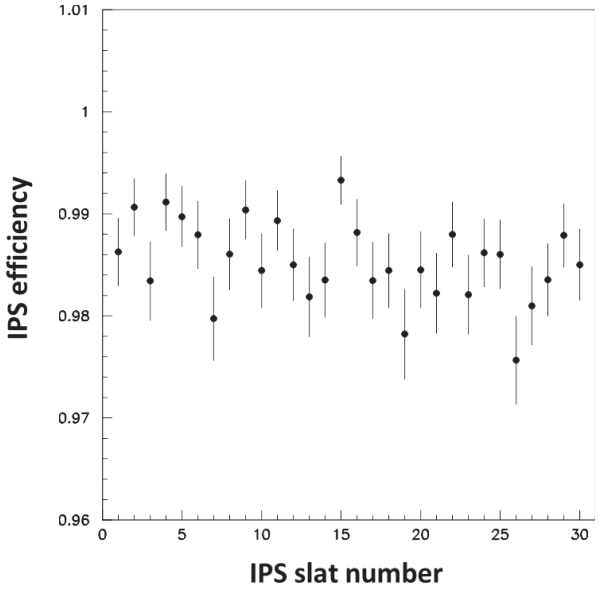


Fig.1. The slat number dependence of the IPS efficiency for proton detection. The IPS slat number corresponds to the azimuthal angle around the $LH_2$ target.

interferences. Therefore, the measurement of the photon beam asymmetry, which is represented by the interferece terms of helicity amplitudes, is a strong tool to decompose the $N^*$ resonances.

The $\eta \to \gamma\gamma$ decay is detected at the BGOegg electromagnetic calorimeter, which is composed of 1,320 BGO crystals covering the polar angle range from 24 to 144 degrees [1, 2]. The proton in the final state is detected at the planar drift chamber (DC) or the BGOegg calorimeter with the charge identification by the inner plastic scintillators (IPS). The DC is placed in the forward acceptance hole corresponding to the polar angles less than 21 degree. The experimental data was collected in the latter half of 2014 (2014B cycle) by irradiating the 1.3–2.4 GeV tagged photon beam [3] onto the liquid hydrogen ($LH_2$) target [4] at the SPring-8 LEPS2 beamline.

The event selection has been done in two ways: One is the simple selection by the combination of mass spectra and kinematical cuts [5]. The $\eta$ meson and the proton are identified by the $2\gamma$ invariant mass and the p($\gamma$,$\eta$) missing mass, respectively. The kinematical angle consistency between the detected proton track and the missing momentum calculated from the 4-momentum of the $\eta$ meson was also required to reduce backgrounds. The other method of the event selection was done by removing low $\chi^2$ probability events after the kinematical fit with the constraints of the 4-momentum coservation and the $\eta$ mass.

The photon beam asymmetry $\Sigma$ is defined from the production rate modulation depending on the azimuthal angle difference between the reaction plane and the linear polarization vector of the photon beam. In order to obtain the information about the $N^*$ resonance decomposition, the photon beam asymmetry was measured in 5 bins of the CM energy and 4 bins of the $\eta$ emission polar angle at the CM frame. During the measurement of the photon beam asymmetry, various checks were performed for systematics confirmations. For example, Figure 1 shows the efficiencies of IPS, which is segmented into 30 long slats in the azimuthal direction. It has been confirmed that there is no azimuthal dependence

for the charge identification, which can possibly make an artificial asymmetry. The data collection was done with the two perpendicular directions of photon beam linear polarization, so that any geometrical effect to the photon beam asymmetry can be found. Such effect has not been observed.

Figure 2 shows the azimuthal distribution of the $\eta$ meson signal counts, measured based on the event selection by the mass spectra and kinematical cuts. In order to extract the $\eta$ signal counts, the signal and background template shapes were simultaneously fitted to the $2\gamma$ invariant mass and missing mass spactra. The photoproduction processes of $\pi^0\pi^0 p$, $\eta\pi^0 p$, and $\omega p$ final states were taken into account as backgrounds. Even after reducing backgrounds enough with the tight cut making the signal acceptance one third, the strength of azimuthal asymmetry was confirmed to be unchanged.

Figure 3(a) shows the result of the beam asymmetry measurement at the lowest energy bin. In this energy region, the CB-ELSA collaboration has reported a comparable result [6], showing the good consistency with the BGOegg measurement. In contrast, the results in the higher energy region are new. Here we show the beam asymmetries for the highest energy bin in Fig. 3(b). Apparently, the polar angle dependence is different from the lowest energy bin, and this information must provide a strong constraint on the $N^*$ decomposition. The final results will be shown with the differential cross section measurement.

## References


[1] N. Muramatsu, ELPH Report 2044-13 (2013) or arXiv:1307.6411.

[2] T. Ishikawa *et al.*, Nucl. Instr. Meth. **A837**, 109 (2016).

[3] N. Muramatsu *et al.*, Nucl. Instr. Meth. **A737**, 184 (2014).

[4] N. Muramatsu *et al.*, ELPH Annual Report Vol.5, 106 (2015).

[5] T. Hashimoto *et al.*, Oral presentation, JPS meeting (Osaka), 19 Mar 2017.

[6] D. Elsner *et al.*, Euro. Phys. J. **A33**, 147 (2007).

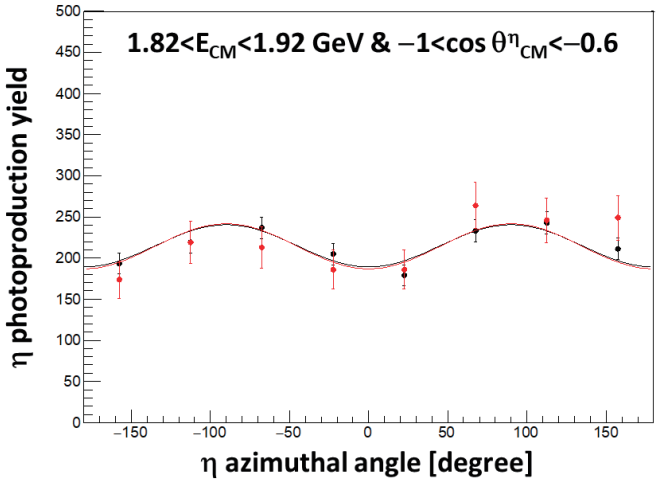


Fig.2. The yields of $\gamma p \to \eta p$ depending on the azimuthal angle of the $\eta$ meson relative to the linear polarization vector of the photon beam. The case of the lowest energy bin and the most backward bin is plotted here. The black data points show the result of the standard template fit, while the red points indicate the yields after the very tight cuts on the invariant and missing masses. The tight cut result is scaled to the standard cut measurement.

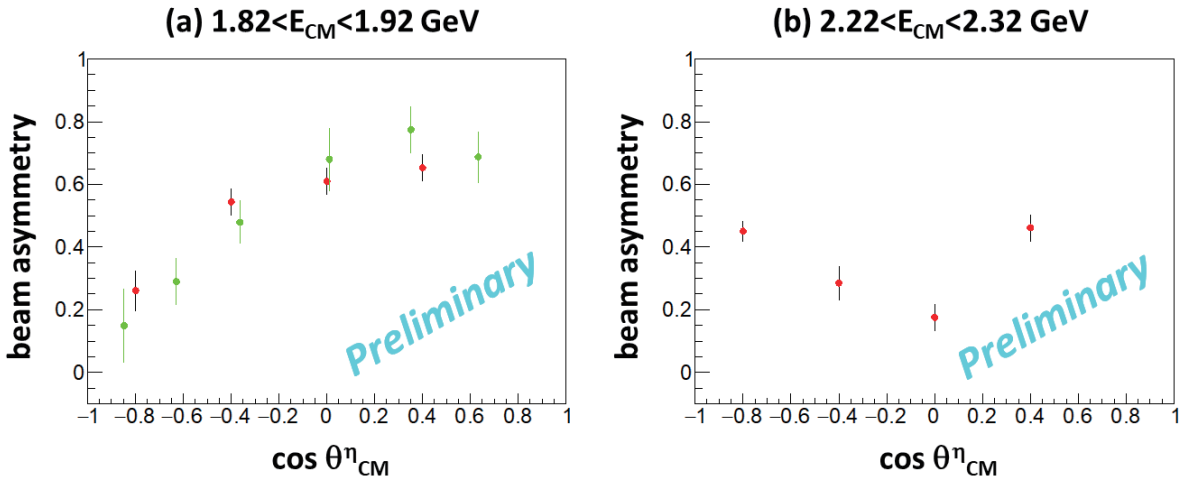


Fig.3. The photon beam asymmetries for $\gamma p \to \eta p$ at (a) the lowest and (b) the highest energy bins. The red (green) points indicate the result of BGOegg (CB-ELSA) experiments.

# Pulse laser test for the backward Compton scattering at the SPring-8 LEPS beamline

Norihito Muramatsu[1], Hitoshi Katsuragawa[2], Takashi Nakano[2], Yuji Ohashi[3], Schin Daté[3], and Yosuke Orii[4]

[1]*Research Center for Electron Photon Science, Tohoku University, Sendai, Miyagi 982-0826, Japan*
[2]*Research Center for Nuclear Physics, Osaka University, Ibaraki, Osaka 567-0047, Japan*
[3]*Japan Synchrotron Radiation Research Institute (SPring-8), Sayo, Hyogo 679-5198, Japan*
[4]*Spectronix Corp., Suita, Osaka 564-0062, Japan*

High energy photon beams are available at SPring-8 LEPS and LEPS2 beamlines by the backward Compton scattering of ultraviolet laser light from 8 GeV electrons in the storage ring [1]. They are used to produce various hadrons and to investigate their natures. Currently, the intensity of the tagged photon beam in the energy range below 2.4 GeV reaches a few MHz by the simultaneous injection of a few laser beams. While the photon beam has several specific features as a hadron beam, there is a disadvantage for the low interaction rate with a target material to produce hadrons. Therefore, the method to increase the beam intensity up to 5–10 MHz has been strongly desired.

One way to upgrade the beam intensity is the use of the pulse laser whose output timing is forced to be synchronized with the electron beam bunches. While the electron beam bunch exists at 1.966 nsec-each RF packets with various filling patterns, the lasers are currently operated in the CW or quasi-CW mode, emitting the laser light even at the time periods when the electron bunches do not exist at the interaction region. Recently, the pulse laser whose emission timing pattern can be generated intentionally with external trigger inputs is being available from Spectronix Corp. By using this pulse laser, the output power corresponding to a few tens W in the CW mode can be concentrated only at the moments when the electron bunches exist.

In December 2016, we temporarily installed a demonstration machine of 355 nm ultraviolet pulse laser with a few hundreds mW output at the LEPS beamline. The external trigger signal was generated from the accelerator RF signals with prescaling. Pulsed laser light was emitted with a set frequency after accepting the trigger signal. We chose the SPring-8 beam cycle whose electron filling pattern was so-called “A-mode”, so that the laser was emitted at every 23.6 nsec, corresponding to the electron beam bunch interval. The delay time of the external trigger signal input was also adjusted because the pulsed light must meet with an electron beam bunch optimally at the laser focus point or the interaction region. Therefore, the NIM-standard circuit for the time delay with a 0.5 nsec precision was set at the external trigger signal line.

Figure 1 shows the result of photon beam intensity measurement with the pulse laser. The horizon-

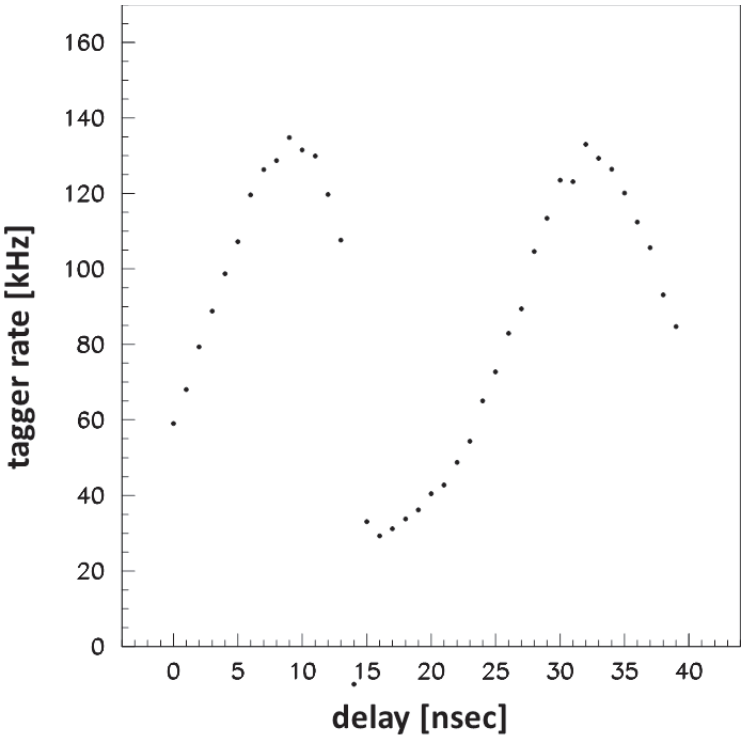


Fig.1. The intensity modulation of the tagged photon beam depending on the delay time of the external trigger signal for the pulse laser. The sudden change at 14 nsec corresponds to the edges of the straight section of the storage ring.

tal axis represents the amount of delay. Here, the photon beam intensity was measured by the tagging counter, which detected recoil electrons from the backward Compton scattering. The intensity modulation depending on the delay time was observed as expected. In order to compare with the beam intensity in the case of CW laser injection, the emission frequency was slightly changed from the rate of 23.6 nsec intervals for asynchronous scattering, while the laser output power was kept. The asynchronous scattering did not show the intensity modulation pattern with the variation of delay. From the comparison of the two injection methods, we observed the pulse laser injection with the optmized frequency and delay provided about two times larger beam intensity compared with the CW laser case.

Based on the test with the demonstration machine, the effectiveness of the pulse laser injection was confirmed well. It has been found that the enhancement factor of $\sim$2 can be improved by achieving the ideal laser focus. In addition, the pulse laser emission can be suitably arranged even for the complicated electron filling patterns by programming the external trigger signal timings at a function generator. Further tests will continue for practical application.

## References

[1] N. Muramatsu *et al.*, Nucl. Instr. Meth. **A737**, 184 (2014).

# Electron scattering with stable nuclear targets at SCRIT electron scattering facility

K. Tsukada[1], K. Adachi[3], A. Enokizono[3], T. Fujita[3], M. Hara[2], M. Hori[3], T. Hori[2], S. Ichikawa[2], K. Kurita[3], T. Ohnishi[2], T. Suda[1], T. Tamae[1], M. Togasaki[3], N. Uchida[3], M. Wakasugi[2], M. Watanabe[2], and K. Yamada[3]

[1]*Research Center for Electron Photon Science, Tohoku University, Sendai, 982-0826*
[2]*RIKEN Nishina Center for Accelerator-Based Science, Wako, 351-0198*
[3]*Department of Physics, Rikkyo University, Tokyo, 171-8501*

Electron scattering off stable nuclei, $^{132}$Xe and $^{208}$Pb were performed at SCRIT electron scattering facility as commissioning of the facility in 2016. For both targets, the diffraction pattern on the reaction cross section were successfully measured and information of the charge density distributions were extracted. Here, some results for $^{132}$Xe and $^{208}$Pb targets are reported.

## §1. Introduction

The SCRIT (Self-Confining Radioactive Isotope Target) [1] electron scattering facility have been constructed at RIKEN to realize electron scattering off unstable nuclei as reported in previous reports [2, 3]. This year, commissioning studies of spectrometers and target ion transportation systems have been performed with several stable targets. Note that the results for the $^{132}$Xe target is already published [4].

## §2. Experimental Apparatus

### 2.1 overview of the facility

Figure 1 illustrates the SCRIT electron scattering facility. The facility consists of a 150-MeV race-track microtron (RTM), an electron storage ring (SR2) equipped with the SCRIT, an electron-beam driven RI separator for SCRIT (ERIS) [5], a fringing-RF-field-activated ion beam compressor (FRAC) [6], and a window-frame spectrometer for electron scattering (WiSES), and a luminosity monitor (LMON). The 150 MeV-electrons from RTM are stored and accelarated in SR2. During the electrons circulating, target ions are mass-separated and delivered into SCRIT by ERIS and FRAC, and then scattered electrons are measured by WiSES. Details of the facility are found elsewhere [7, 8].

### 2.2 Target

For the commissioning experiment, the target nuclei were not provided from the ISOL system of ERIS but extracted from natural materials. The natural xenon gas from a gas bottle was introduced at an entrance branch of the ERIS system, and $^{132}$Xe ions were extracted by a function of ERIS. For the

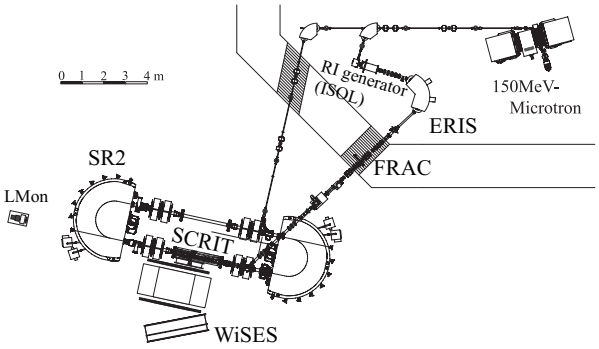


Fig.1. Overview of the SCRIT electron scattering facility.

lead target, natural lead was installed at the head of the ERIS and heated up to 300°. Then, $^{208}$Pb ions were separated from the vapor of the lead by ERIS.

Since $^{208}$Pb is one of the most extensively investigated stable nuclei and the form factor is precisely derived by electron scattering [9], it is the best target to check the spectrometer performance. On the other hand, although $^{132}$Xe is a stable nucleus and the root-mean-square radius is evaluated from the measurement of X-rays from muonic atoms [10], electron scattering has never been performed. This work is, therefore, the first to determine the charge density distribution of $^{132}$Xe.

The target ions were stored in the SCRIT for a few hundred ms and ejected to refresh the target quality because the amount of the residual gas ions also increased due to the ionization and trapping by the electron beam. The SCRIT operation with and without target ions (IonIN/IonOUT) were alternated for the comparative measurement and the background subtraction. The trapping times were 240 msec for the $^{132}$Xe target and 990 msec for the $^{208}$Pb target experiment. In the present analysis, however, the first 240 msec to the 990 msec trapping time was used even for the $^{208}$Pb target because it was found that the time evolution of the amount of residual gas ions was influenced by the amount of the target ions and the background subtraction method did not work correctly for the rest of the time. The interval among the trapping times was fixed to be 10 ms.

## §3. Run summary

Table 1 shows run summaries for the series of the commissioning with $^{132}$Xe and $^{208}$Pb targets in 2016. Achieved averaged-luminosities are also listed in the table. The number of ions introduced was about $10^8$ particles/pulse, and the achieved lumionsities were around $10^{27}$ cm$^{-2}$s$^{-1}$ on average.

## §4. Data analysis

Details of the data analysis are explained elsewhere [2–4]. Figure 2 shows the differential cross sections multiplied by luminosity for elastic electron scattering off $^{208}$Pb. By changing the electron beam energy, a wide range of momentum transfer can be covered. The line represents a phase shift calculation [11] with the nuclear charge density distribution modeled as a sum-of-Gaussian function [9].

Table 1. Run Summary Table. The irradiation time corresponds to the total time of IonIN conditions. The duty is defined as, $duty = T_{IonIN}/(T_{IonIN} + T_{IonOut} + 2 * T_{Interval})$. The luminosities are averaged values evaluated by WiSES assuming a nuclear charge density distribution.

| Ee [MeV] | target | Date | Irradiation time [sec] | Duty [%] | Luminosity [/cm$^2$/s] |
|---|---|---|---|---|---|
| 151 | $^{132}$Xe | 19-22/Jan | $1.9\times10^4$ | 49.5 | $8.7\times10^{26}\pm2.0\%$ |
| | $^{132}$Xe | 8-10/Feb | $7.8\times10^3$ | 48.0 | $1.1\times10^{27}\pm2.5\%$ |
| 201 | $^{132}$Xe | 6-14/Apr | $1.3\times10^5$ | 48.0 | $1.1\times10^{27}\pm1.8\%$ |
| 301 | $^{132}$Xe | 2-13/Jun | $1.9\times10^5$ | 48.0 | $1.6\times10^{27}\pm8.1\%$ |
| 151 | $^{208}$Pb | 19-23/Jul, 1-2/Aug,6/Aug | $6.7\times10^3$ | 49.5 | $2.5\times10^{27}\pm5.7\%$ |
| 201 | $^{208}$Pb | 23-25/Jul, 2-4/Aug | $5.0\times10^4$ | 49.5 | $1.0\times10^{27}\pm5.9\%$ |
| 301 | $^{208}$Pb | 25/Jul-1/Aug, 4-5/Aug | $1.7\times10^5$ | 49.5 | $1.3\times10^{27}\pm6.8\%$ |

The luminosity is considered as a fitting parameter in the present analysis because the study of the LMon to determine the absolute value of luminosity is underway. The momentum-transfer dependence is well reproduced by the calculation.

Figure 3 shows the plot for elastic electron scattering off $^{132}$Xe. The number of introduced target ions and the achieved luminosity were similar to those for $^{208}$Pb. The parameters of a two-parameter Fermi distribution are determined by comparing our data and a calculation. The lines for elastic scattering are calculated with the best values of a two-parameter Fermi distribution. The contamination of inelastic scattering which is calculated with a distorted wave Born approximation code FOUBES [12, 13] using a transition density distribution of the ground state to the first $2^+$ state [14] is negligibly small, as shown in the figure. By changing parameters, radius C and diffuseness t, of the two-parameters Fermi distribution, the most probable values are firstly extracted to be $C$=5.42$^{+0.11}_{-0.08}$ fm and $t$=2.71$^{+0.28}_{-0.38}$ fm , and resulting $\langle r^2\rangle^{1/2}$=4.79$^{+0.12}_{-0.10}$ fm [4].

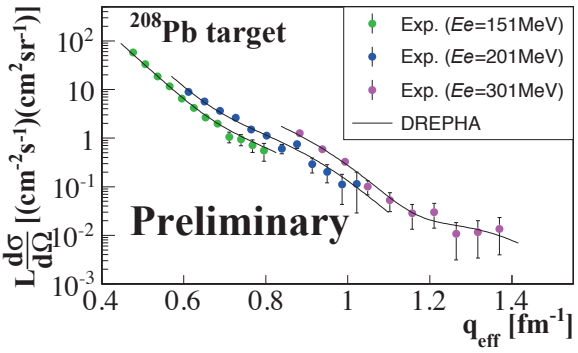


Fig.2. Differential cross sections of $^{208}$Pb(e,e) multiplied by the luminosity for the effective momentum transfer at $E_e$=151, 201, and 301 MeV. The line is a phase shift calculation with the nuclear charge density distribution modeled as a sum-of-Gaussian function [9].

## §5. Conclusion and future prospects

The SCRIT electron scattering facility has been constructed to realize electron scattering off unstable nuclei. In 2016, several commissioning experiments with stable nuclear targets have been preformed.

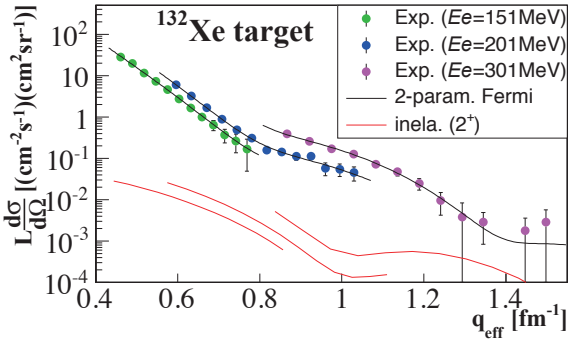


Fig.3. Differential cross sections of $^{132}$Xe(e,e) multiplied by the luminosity for the effective momentum transfer at $E_e$=151, 201, and 301 MeV. The lines are a phase shift calculation with the nuclear charge density distribution modeled as a two-parameter Fermi distribution (solid) and contributions of inelastic scattering calculated by a beyond relativistic mean field theory [14] (dashed).

The momentum transfer distributions of $^{208}$Pb were well reproduced by a calculation with the charge density distribution which was precisely determined ever. Furthermore, from the momentum transfer distribution of $^{132}$Xe, nuclear charge density distribution is firstly extracted by changing parameters of the two-parameters Fermi distribution.

Following this successful experiments, elastic electron scattering experiment for $^{138}$Xe nucleus which is an unstable nucleus will be performed this year.

## References


[1] M. Wakasugi *et al.*: Nucl. Instr. Meth. B**317**, 668 (2013).

[2] K. Tsukada *et al.*: ELPH Annual Report 2014 Vol. 5, Tohoku University, 125 (2014).

[3] K. Tsukada *et al.*: ELPH Annual Report 2015 Vol. 6, Tohoku University, 99 (2015).

[4] K. Tsukada *el.*: Phys. Rev. Lett. **118**, 262501 (2017)

[5] T. Ohnishi *et al.*: Nucl.Instrum.Meth. B317, 357-360 (2013).

[6] M. Togasaki *et al.*: Proceedings of HIAT2015, WEPB25 (2015).

[7] T. Suda *et al.*: ELPH Annual Report 2011-2013 Vol. 2, Tohoku University, 201 (2013).

[8] T. Ohnishi *et al.*: Phys. Scripta, T166, 014071 (2015)

[9] B. Frois *et al.*: Phys. Rev. Lett. **38**, 152 (1977).

[10] G. Fricke *et al.*: Atomic Data and Nuclear Data Tables **60**, 177 (1995).

[11] J. Friedrich: *A phase-shift calculation code for elastic electron scattering, communicated by J. Friedrich.*

[12] J. Heisenberg: Advances in Nuclear Physics, 12, 61 (1981)

[13] J. Heisenberg and H. P. Blok: Annual Review of Nuclear and Particle Science, 33, 569 (1983)

[14] M. Hua, K. Hagino: private communication.

(ELPH Experiment : #2836)

# RI Production for the synthesis of Promethium Endohedral Metallofullerenes by Photon Activation Method

K. Akiyama[1], S. Miyauchi[1], and H. Kikunaga[2]

[1]*Department of Chemistry, Tokyo Metropolitan University, Hachioji, 192-0397 Japan.*
[2]*Research Center for Electron Photon Science, Tohoku University, Sendai, 982-0826 Japan.*

The production of **Pm** metallofullerenes were retried using chemically separated $^{143}$**Pm** with higher specific radioactivity than that of previous work. As the results of HPLC analysis, two elution peaks were found in the dominant peak observed in the previous work and the HPLC retention time of these two peaks were evaluated to be 61.2 **min** and 64.6 **min**, respectively, by the least square fit of data. The evaluated HPLC retention time of the first peak was found to be little later than that of La metallofullerene.

## §1. Introduction

Endohedral metallofullerenes (EMFs) are known as a clathrate compound and are attracting interest of the expectation for the potential application brought from their unique physical and chemical properties. The large number of studies about the EMFs have been reported, so far. Especially for the EMFs of lanthanide, it has been studied for a variety of encapsulated elements from the dawn of metallofullerene research. However, only metallofullerene of promethium (**Pm**) has been still missing [1]. It is well known that **Pm** is one of the artificial elements belonging to lanthanide elements and do not have any naturally occurred stable isotope. The chemical property of **Pm** is considered to be almost same as those of other neighboring lanthanides, actually most stable oxidation state in water is +3 similar to neighboring element of **Nd**. In general, **Pm** is produced from processing nuclear fuel and neutron irradiation of **Nd** in High Flux Isotope Reactor. However, $^{143}$**Pm** produced by these methods is not suitable for the metallofullerene research because of their small $\gamma$-ray emission rate and their long half life.

Recently, we reported the production of **Pm** metallofullerenes using $^{143}$**Pm** produced by photon activation of natural samarium and their properties such as oxidation state of **Pm** in fullerene cage [2]. Though the oxidation state of **Pm** in fullerene cage and main species of **Pm** metallofullerenes were clarified, there are some problems to investigate detailed information about the properties of **Pm** metallofullerenes. These problems is caused by the lower specific radioactivity of $^{143}$**Pm** in irradiated **Sm** targets. Previously, we tried to purify $^{143}$**Pm** from irradiated **Sm** targets by cation exchange chromatography and succeeded to remove more than 90% of **Sm**.

Here, we report the resutls of re-investigated HPLC elution behavior of **Pm** metallofullerenes produced by above mentioned purified $^{143}$**Pm**.

*Correspondance: Graduate School of Science and Engineering, Tokyo Metropolitan University, Hachioji, 192-0397 Japan.

## §2. Experimental

### 2.1 Synthesis of Promethium Endhedral Metallofullerenes

About 1.0 **g** of **Sm** oxide were wrapped by **Al** foil and sealed into quarts tubes. These targets were irradiated by 50 **MeV** photon at Research Center for Electron Photon Science in Tohoku University. Irradiated **Sm** targets were dissolved to conc. **HCl** and then evaporated to dryness to make **Sm** and **Pm** to chloride form. Chlorinated target materials were dissolved to 3 **mL** of 2 **M HCl**. Accurate 10 $\mu$**L** of 2 **M HCl** solution was added to 9.990 **mL** of $\mathbf{H_2O}$ for dilution. **Pm** was separated from this diluted **Pm**/**Sm** solution by cation exchange chromatography previously reported [3].

This separated **Pm** was dissolved into concentrated nitric acid together with about 0.5 **g** of $\mathbf{La_2O_3}$ as a carrier. This solution was heat to dryness and then EtOH was added for dissolving resultant nitrate salts. This EtOH solution was dropped on a porous carbon rod with 10 **mm** diameters and 60 **mm** length to adsorb the nitrate salts and then dried. This porous carbon rod was placed in an electric tubular furnace and sintered at 700 $^o$**C** under $\mathbf{N_2}$ gas flow. After the sintering, this rod was set into the fullerene generator as an anode for the arc discharge. The promethium EMFs were produced by the arc discharge method [2] with DC 100 **A** under 60 **kPa** of He atmosphere. The produced soot containing **Pm** EMFs was dissolved to $\mathbf{CS_2}$ and then filtered to remove insoluble substance. After filtration, $\mathbf{TiCl_4}$ was added in this solution for the pre-separation of EMFs [4]. This pre-separated EMFs solution was evaporated to dryness and then toluene was added to dissolve fullerene species for the HPLC analysis.

### 2.2 HPLC Elution Behavior of Pm@$C_{82}$

The EMFs toluene solution was injected into HPLC system (Pump: Hitachi L-7110, flow rate: 3.2 **mL/min**, UV detector: GL-Science GL-7450, $\lambda$ = 340 **nm**) with a HPLC column of Buckyprep (Nakarai tesque inc., size: 10 $\phi$**mm** $\times$ 250 **mm**). The eluate from HPLC was collected for every 20 **sec** with the range from 50 to 70 **min** of the retention time and other fractions were collected for every 5 **min** up to 100 **min** of the retention time. The $\gamma$-ray from each fractionated sample was determined by a germanium semiconductor detector (SEIKO EG&G, GEM25P4).

## §3. Results and Discussion

In the previous work, we found that the main species of Pm metallofullerenes was **Pm@C**$_{82}$ similar to other light lanthanide metallofullerenes [2]. Figure 1 shows the HPLC chromatogram of **Pm** metallofullerenes investigated in this study and the HPLC chromatogram of **Pm** metallofullerenes obtained in the previous work is shown in the inset. The radioactivity observed in the samples collected for 5 **min** plotted in this figure were averaged to be same volume as the samples collected for 20 **sec**. The dominant elution peak was only observed around 60 **min**. This tendency is correspond to that observed in the previous work.

Figure 2 shows the detailed HPLC chromatogram around the dominant elution peak. For comparison, separately obtained chromatogram of **La** metallofullerenes asigned as a **La@C**$_{82}$ was also plotted. Although the only one elution peak was observed in the chromatogram of **La** metallofullerene, two elu-

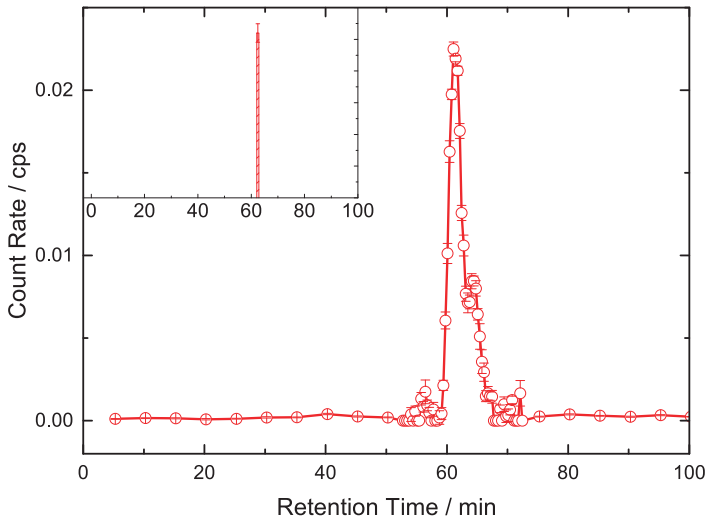


Fig.1. HPLC elution behavior of **Pm** metallofullerenes. HPLC chromatogram of **Pm** metallofullerenes obtained in the previous work is shown in the inset.

tion peaks were observed in that of **Pm** metallofullerenes. To determine the exact retention time of the peaks, least square fit was performed for the obtained data using "extreme" function as shown in the following.

$$y = y_0 + Ae^{(-e^{(-\frac{(t-t_c)}{(w)} - \frac{(t-t_c)}{(w)}+1)})} \quad (1)$$

Here, $y_0$, $A$, $t_c$, and $w$ indicate the base line, the peak area, the retention time at the peak top, and the width of the peak, respectively.

The HPLC retention time of observed elution peaks between 50 to 70 **min** were found to be 61.2 **min** for the first peak and 64.6 **min** for the second peak as the result of least square fitting. For the first peak, the retention time of the **Pm** metallofullerene is little later than that of the **La** metallofullerene and differences from that of **La** metallofullerene was 1.05 **min**. It is considered that the electronic state of cage surface is slightly affected by the encapsulated lanthanide ion as shown in the UV/vis/NIR absorption spectra of a series of lanthanide **M@C**$_{82}$, so this trend in the peak retention time is expected to be caused by the differences of encapsulated metal ion. [5] The differences in HPLC retention time between **La@C**$_{82}$ and the second elution peak was 4.45 **min**. This value is too large to identify that the second peak is derived from **Pm@C**$_{82}$ with similar electronic state of **La@C**$_{82}$.

## Conclusion

**Pm** metallofullerenes were re-produced using chemically separated $^{143}$**Pm**. As the results of HPLC analysis, two elution peaks were found in the dominant peak observed in the previous work and the HPLC retention time of these two peaks were evaluated to be 61.2 **min** and 64.6 **min**, respectively, by the least square fit of data. The evaluated HPLC retention time of the first peak was found to be little

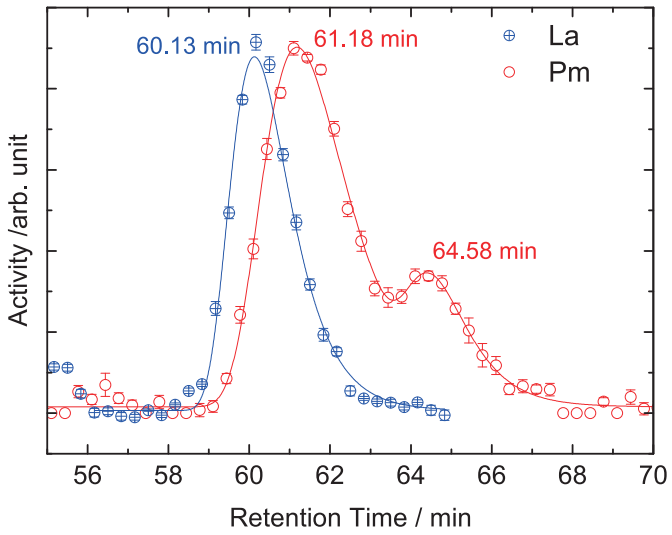


Fig.2. Detailed HPLC chromatogram around the dominant elution peak of **Pm** metallofullerenes. Separately obtained HPLC chromatogram of **La** metallofullerene is also plotted for comparison.

later than that of La metallofullerene.

## Acknowledgment

We deeply thank to the facility staffs of research center for electron photon science at Tohoku University for supplying the high-quality electron beam. And also we thank to Doctor Kyo Tsukada for helping us in the sample irradiation.

## References

[1] H. Shinohara: Rep. Prog. Phys. **63** (2000) 843.

[2] K. Akiyama *et al.*: ELPH Annual Rep. (2014) 135.

[3] K. Akiyama *et al.*: ELPH Annual Rep. (2015) 112.

[4] K. Akiyama *et al.*: J. Am. Chem. Soc. **134** (2012) 9762.

[5] K. Akiyama *et al.*: J. Phys. Chem. A **104** (2000) 7224.

# III. Status Report

# Status of Accelerator Facilities in FY2016

Accelerator group

*Research Center for Electron Photon Science, Tohoku University, Sendai, 982-0826*

The electron accelerator complex: high intensity 60 MeV linac, 90 MeV injector linac and 1.3 GeV BST (booster-storage ring), had been regularly operated for user time in FY 2016, however some minor troubles occurred. In this report, machine status and some improvements are presented.

## §1. High Intensity Linac

### 1.1 Overview of machine operation

For the 60 MeV high intensity linac, the operating beam time reached 252 hours in FY 2016. Beam energy with 50 and 30 MeV were used most often, and the average current was 120 $\mu$A and 80 $\mu$A, respectively. Usually beam users bring samples to be irradiated and place them on our irradiation system. However we also accept some users who need to use their own irradiation stand to mount their sample. In such case, the sample location and required beam size, etc. can be different from the regular operation, so that we performed a machine study to meet the required condition prior to the user operation. This had taken place successfully and then such specially required operations have been also well managed.

### 1.2 Installation of an AC regulated power supply in the cathode heater line

Since the recovery from the damage caused by the great earthquake in March 2011, it has become possible to operate the BST ring and the high intensity linac independently and simultaneously. Both machines share a common electrical ground with the same high voltage transformer, therefore some power supplies like gun cathode heater tend to interfere with their stable operation each other during the simultaneous operation of both accelerators. Indeed, a drift more than 10 % has been observed in the emission current from the cathode of the high intensity linac during the BST operation. Since the heater voltage of the cathode is particularly sensitive to the emission current from the gun, we first introduced an AC regulated power supply for the cathode heater. There are still some power supplies to be stabilized, so that further improvement work is underway toward the higher stability.

### 1.3 Replacement of insulating oil and rectifier elements in klystron modulators

Although there was no major trouble in the klystron modulators over the past decade, it had been found that insulating oil of some of the tanks in the modulators was considerably deteriorated with respect to electrical insulation (Fig. 1). It turned out that many electronic components for rectifier

circuit in the oil tanks such as diodes, capacitors and resisters had been also damaged due to the aging degradation (Fig. 2). We have already replaced the degraded oil and the damaged electronic components at some oil tanks, but there are still tanks that need to replace the oil and possibly some electronic components, so that those replacements will be carried out in the next year.


Fig.1. Voltage transformer extracted from insulation oil tank. It was cleaned and refilled with new oil.

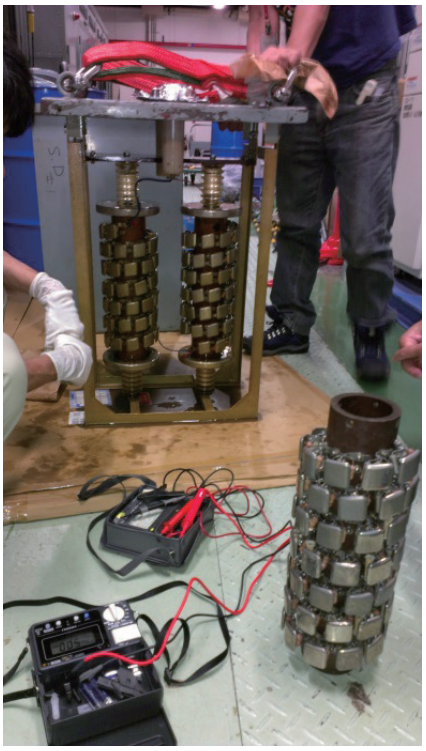

Fig.2. Voltage rectifier units extracted from insulation oil tank. The assembly which some elements fails (back), and re-assembled unit (front).

### 1.4 Preparation of a display of operating status for beam user

Since the some beam users have to complete their own tasks, such as separation of irradiated RI products and preparation of samples to be irradiated, during the interval of beam irradiations for their sample, they need to manage time for the tasks. As a convenience for such users, we have been preparing a status display of the accelerator operation. Several items: the operation status, a history of average beam current and the irradiation logs etc., are presented in a monitor display as shown in Fig. 3. Beam position at the target location and cooling water temperature for the target are also displayed in the same information monitor.

### 1.5 Beam profiling at the dispersion section

Replacement of beam monitoring system has been continued from 2015, and optical transport for the screen at the dispersion section had installed in this year (Fig. 4). Digital video camera, BASLER acA1300-30gm, was used and triggered by a signal synchronized with 1 Hz beam repetition. Camera resolution at focal point is about 110 ($\mu m$ / pixel) in position. It corresponds to the energy resolution of 7


Fig.3. Operation status display. Current state in the operation sequence (red). History of the average beam current for 3 hours (cyan). Irradiation log in chronological order (yellow). Irradiation-position-monitor (magenta). Temperature indicator of water used for target cooling (green).

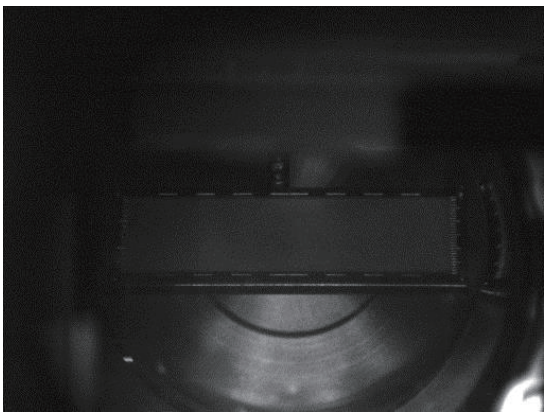

Fig.4. SM3 profile monitor. 9030 mm alumina screen with its thickness 0.2 mm where the dispersion function is 0.8 m.

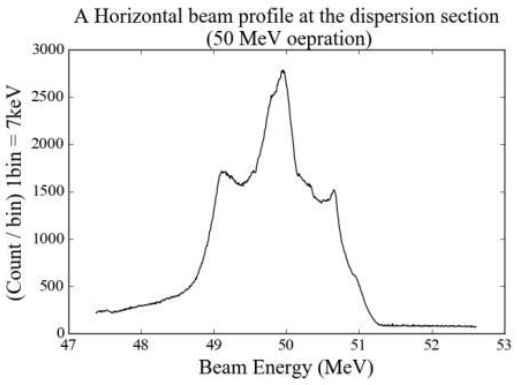


Fig.5. The intensity plot of light emitted at the SM3 screen.

keV/pixel at the screen position with the dispersion function of 0.8 m. The profile on this screen will be used to check the beam response to the linac parameters such as the phases in accelerating structures (Fig. 5).

## §2. 90 MeV Injector Linac for BST

At the end of FY2015, the thermionic rf gun had a problem that a discharge at the cathode cell in the gun was frequently observed due to the deposition of carbon-like matter between the cathode and

the cavity wall. There was no such discharge so far in the same rf gun installed in the test accelerator t-ACTS. In order to improve the vacuum pressure in the gun cavity an additional ion pump was installed at the same time as replacing the $CeB_6$ cathode, but the similar discharge phenomenon was nonetheless observed again. After replacing the cathode on the end of FY2016, the injector linac has operated stably, but the reason for the deposition is still under investigation.

## §3. Beam transport line to BST

There are sixteen power supplies for two dipole magnets, seven quadrupoles and four steering magnets in the beam transport line to the BST ring. Those power supplies had been used for about twenty years and frequently stopped abnormally during the user operation time due to an aging degradation. In the FY2015, we had already replaced the power supplies for dipole magnets, and the remained power supplies for the other magnets were replaced in the FY2016. The original power supplies were controlled by GPIB via Ethernet, but replaced new power supplies can be controlled by Ethernet directly. Thus we developed control software for new power supplies, so that reliability and maintainability are also improved significantly. An old power supply for DC septum magnet will be also replaced in next year.

## §4. 1.3 GeV BST ring

In recent years, the user operation had been occasionally interrupted due to the unknown interlock in a power supply for BST klystron. This power supply had already passed twenty years and could be having the aging degradation as a whole. Since there is no cause related to this interlock, it was speculated that some noise signal might be acting on the interlock circuit. During the maintenance work in summer shutdown, indeed, as it turned out that some capacitors on the control circuit were damaged in the power supply, therefore those were exchanged. Although no further interruption caused by the unknown interlock has occurred after the capacitor replacements, we schedule overall maintenance work of this power supply for the next year. The other improvements performed in FY2016 are presented in the following sections.

### 4.1 Replacement of pumping cells in ion pumps

In the BST ring, there are 24 ion pumps and 8 NEG pumps installed to evacuate residual gas in the beam line. All NEG pumps and some ion pumps were recently added, however, a lot of ion pumps had passed long time of about twenty years. Some of those old ion pumps have already lost the capability to evacuate the gas, so that the vacuum pressure had exceeded over $10^{-5}$ Pa under the beam circulation of about 20 mA. In order to improve the vacuum pressure in the ring, it was required to replace the old pumps (150 litter, diode type, Varian Inc.) to new one. Fortunately, we have kept several stocks of old ion pumps, and also pumping cells for those old pumps can be still obtained from Agilent Technologies Inc. Therefore we decided to replace the old pumps with the cell-replaced pumps. Partitioning the whole ring into four areas, the pump replacement was performed for each area with step by step to minimize the

exposure time of vacuum chamber to the air. Figure 6 shows the pictures of inside of the old ion pump and removed pumping cells. It was found that the inside wall of the pumps had spattering vestige of titanium but no other dirt, so that we didnt wash the inside of the pumps. The cell-replaced pumps were baked with 250 degree for 24 hours prior to their installation into the ring. Then all ion pumps in the partitioned area were baked with 250 degree for 24 hours again, and NEG pumps were also activated. Figure 7 shows a trend graph of the base pressure in BST ring. On the summer shutdown in FY2015, one NEG pump was additionally installed and some ion pumps in the injection beam line were baked. Apparent improvement of vacuum pressure was observed at the gauge (CIG5) where the NEG pump was additionally installed, but the effect of baking the ion pumps was not clear. Therefore it is deduced that ion pumps cannot be revived by the baking anymore. On the summer shutdown in FY2016, twelve ion pumps were replaced with the cell-replaced pumps. As shown in Fig. 7, the base pressure seems to have been improved except for CIG7 and CIG8, where ion pumps were not replaced. Remained four ion pumps will be replaced on a shutdown in FY2017.

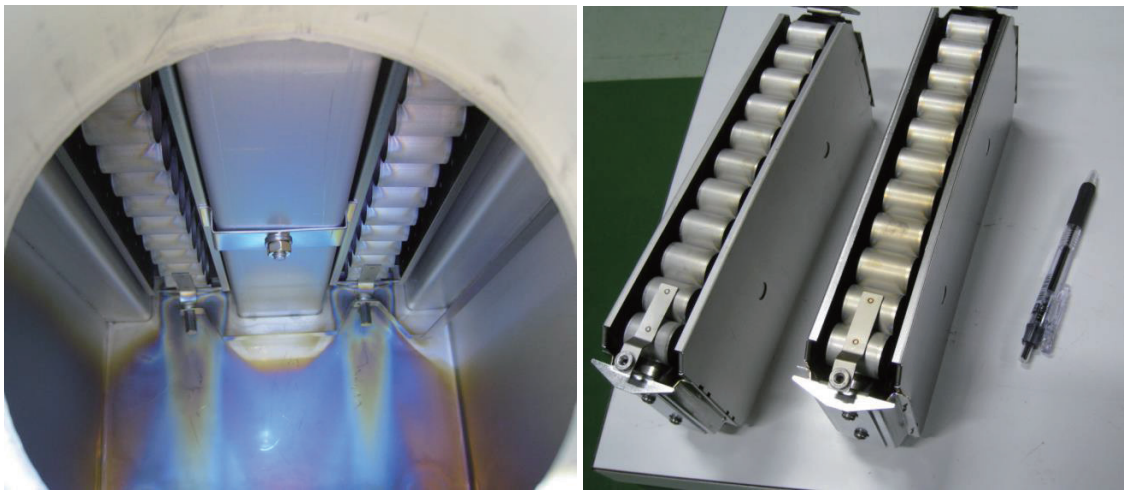

Fig.6. Inside of the old ion pump (left), and removed old pumping cells (right).

## §5. Control system and Utility

As known well, Git [1] is widely used as a version control system in software development. We have employed Git for a backup framework in our control system to improve the availability of the control system. Distributed repositories have been allocated on a network by Git. Those repositories include a history of file modifications. Our system is composed of a Git server and client computers. If files or data on the client computer are lost, those can be restored from the Git server's repository. If the Git server crashes, we can rebuild it from the client computer's repository as well.

The control method of the BST steering magnets had been changed to improve a tracking accuracy of their output current since FY2014. In the new system the power supplies of steering magnets are operated as the current amplifiers driven by an external ramping pattern, compared to the previously used method employing pattern operation with the own pattern memory installed on the power supply

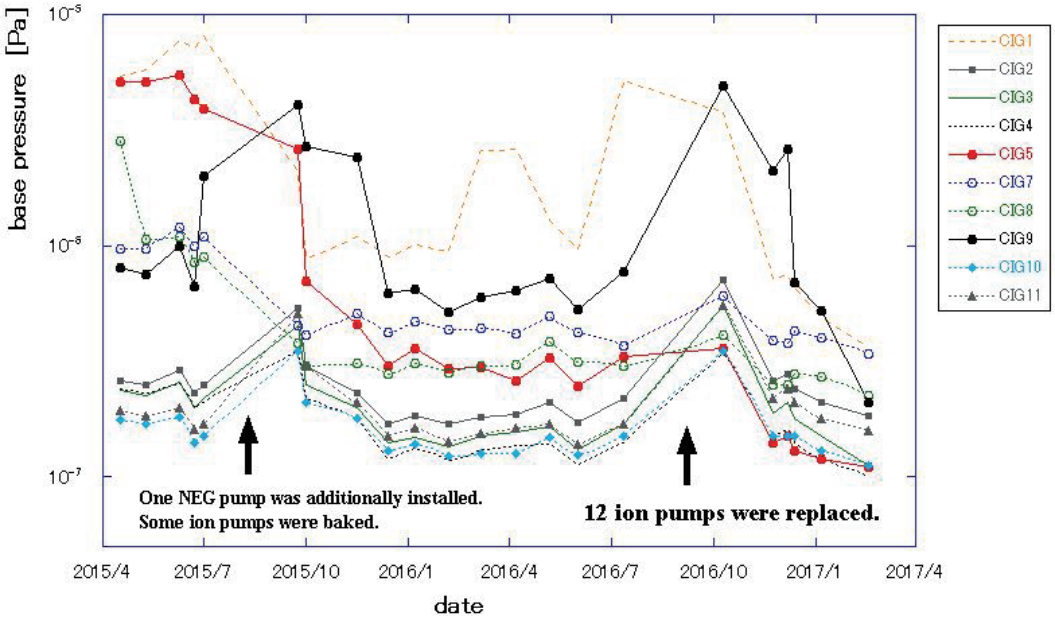


Fig.7. Trend graph of the base pressure in BST ring.

itself. It turned out that the master clock frequency of the external ramping pattern for the steering power supply is slightly higher than the required one in the actual operation, so that it caused a time lag in the steering magnet. As a result this time lag had made it difficult to accurately correct the beam orbit during the ramping process. Since this difference might affect the beam orbit in BST-ring, we had fixed up the problem by tuning the master clock frequency to secure the synchronous operation.

In order to stabilize the temperature of cooling water, the rotation speed of the cooling fan have been already controlled by the inverter drive depending on the ambient temperature, but temperature stability was insufficient at a specific condition like winter season. In order to improve the temperature stability of the primary cooling water, the control system of the cooling tower fan was changed so as to also control the number of cooling fans to be operated depending on the ambient temperature in addition to the inverter drive. As a result of this modification, the stability was improved to one degree comparing to the deviation of about 10 degrees for the previous condition.

## References

[1] https://git-scm.com/

# User Support Office Report in FY2016

M. Miyabe[1] and The user support office[1]

[1]*Research Center for Electron Photon Science, Tohoku University, Sendai, 982-0826, Japan*

The User Support Office coordinate across the users and our facility for management of the beamtime. In 2016 financial year, we had provided the electron, photon and positron beam without apparent problems except for Photon beamline I.

## §1. Introduction

ELPH has three accelerators for Joint Usage/Research. Our facility could provide several beams with following three beam lines,

- 70 MeV electron linear accelerator (linac) at the first irradiation lab (For Radiochemistry)
- Tagged photon beam from 1.3 GeV electron synchrotron called BST ring with 93 MeV injector at the second irradiation lab (For Hadron Physics, **Photon beamline I**)
- Tagged photon beam at the GeV-$\gamma$ irradiation room (For Hadron Physics, **Photon beamline II**)

In addition, positron/electron beam line for testing detectors is located at the GeV-$\gamma$ irradiation room. The 70 MeV electron linear accelerator was utilized for the Radiochemistry experiments by photonuclear reactions. It could produce radio active source with its high intensity. Both tagged photon beam line was used for Hadron physics experiments. NKS2 and FOREST experiment have bean held in recent years.

## §2. Beamtime operated

The total radiation time was 252 hours for the RI linac operation and 1178 hours for the BST operation, and it was 1431 hours in total. The beam provided time (user beamtime) was 252 and 1198 hours for the RI linac and BST operations, and it was 1450 hours in total. Table 1 summarizes the radiation times, and user beam times in fiscal.

Many experiments for testing detectors were made by positron beam line. Positron beam was produced by bremsstrahlung photon beams from the synchrotron. Total XX shift experiments are performed using this positron beam in this financial year.

A Next generation FOREST experiments is planned by GeV-$\gamma$ group in ELPH. New bending magnet will be installed on the downstream of FOREST detectors and it covers the most forward angle. These new experimental setup enable the zero degree proton detection for the $\gamma d \to p\eta n$ reaction at $E_\gamma \sim 0.9$ GeV. This reaction gives the zero relative momentum between the $\eta$ and $n$. This situation will enable to determine the $\eta n$ scattering length. In this financial year, New Dipole Magnet (BLC) was installed in the downstream of FOREST detectors.

Photon beam line I (NKS2) cannot be stably produced, because of the trouble at the radiator system inside the synchrotron. The photon beam was recovered after temporary repairs for the radiator driving system, but full repair will carry out in next financial year.

Two experiments were proposed, and carried out for the undergraduate students. The first one (#2857: T. Ishikawa, ELPH, Tohoku University) is for the third school for giving an opportunity using an accelerator to young undergraduate students (Y. Sakemi) [1], which was supported by High Energy Accelerator Research Organization (KEK) for the corporations between Tohoku University and KEK (H. Tamura). The second one (#2855: K. Tsukada, ELPH, Tohoku University) is for the education of the undergraduate students in ELPH.

Table 1. Radiation times, and user beamtimes in financial year 2016. They are given by the sum of the times that the beam is coming to the beamline, and that the beam is provided to the users.

| | RI Linuac | | BST Ring | |
|---|---|---|---|---|
| Month | radiation (h) | user (h) | radiation (h) | user (h) |
| April | 8 | 8 | 54 | 74 |
| May | 11 | 11 | 64 | 64 |
| Jun | 49 | 49 | 356 | 356 |
| July | 45 | 45 | 0 | 0 |
| August | 0 | 0 | 0 | 0 |
| September | 0 | 0 | 0 | 0 |
| October | 27 | 27 | 104 | 104 |
| November | 29 | 29 | 187 | 187 |
| December | 19 | 19 | 65 | 65 |
| January | 24 | 24 | 103 | 103 |
| February | 19 | 19 | 71 | 71 |
| March | 21 | 21 | 174 | 174 |
| Sum | 252 | 252 | 1178 | 1198 |

## §3. ELPH workshops and ELPH seminars

In this fiscal year, ELPH supported two ELPH workshops. The first one is hadron physics (C015: H. Fujioka, Kyoto University), the second is SNP school 2016 (C016: S. N. Nakamura, Tohoku University). 14 ELPH seminars were held in this fiscal year. Seminars title and talker are listed below.

- Shuo Wang, Shandong University, China JinPing underground Laboratory for Nuclear Astrophysics"
- Jatuporn Saisut, Plasma and beam Physics Research Facility, Chiang Mai University Research Status of PBP - CMU - Linac Group"
- C. Rangacharyulu, Univ. of Saskatchewan, "Gray as an impractical radiation dose unit"
- T. Sekihara, JAEA, "Coupling constant vs. compositeness: a case of N(1535) in the eta N channel"
- Peter von-Neuman-Cosel, Technische Universitat Darmstadt "Nuclear Structure Studies with Virtual Photons"
- K. Umemori, KEK, "High current CW superconductive accelerator. (proposal for RI production from cEBL)"

- Marie-Emmanuelle Couprie, SOLEIL France COXINEL, ”Europian Laser Prasma Accelerator Project for X-Ray Free Electron Laser”
- K. Itahashi, Riken, ”Complex structure of vacuum and precision spectroscopy of $\pi$ meson atom.”
- S. Hirenzaki, Nara, Women’s University ”Recent topic and Physics in mesic nuclei systems”
- H. Ohnishi, Riken, ”Kaon and phi meson in nucleus”
- S. Nakamura, Osaka University, ”Study for the $\eta$n interaction with $\gamma d \to \eta np$ reaction.”
- H. Nagahiro, Nara Women’s University ”The production of eta mesic nuclei and the property of $N^*(1535)$ in nuclear medium.”
- S. Sasaki, Tohoku University ”Recent result of lattice QCD at the physical point simulation for nuclear structure.”
- Y. Kino, Tohoku University ”Precision calculation for an exotic atom and molecular. - Connection radiochemistry with nuclear physics -”

## References

[1] Y. Sakemi, Web site < http://cycgw1.cyric.tohoku.ac.jp/~sakemi/cyric2016.html >

# Radiation Safety Report 2016

Radiation Safety Office

放射線安全管理室より、2016 年度（平成 28 年 4 月 ～ 平成 29 年 3 月）の報告を以下の通り行う。

## §1. 許認可申請

H28 年 6 月 6 日　変更承認申請
H28 年 7 月 28 日　承認
（変更の内容）
1. 様式第一中別紙様式イ，ハにおける使用の目的の変更
2. 加速装置 1 台のエネルギー変更
3. GeV ガンマ線照射室ビームダンプの変更
4. 使用核種の見直し
5. 放射化物保管設備の設定
6. 保管廃棄設備の変更
7. 作業室グローブボックスの変更
8. 下限数量以下 RI の管理区域外使用
9. インターロック動作の変更

H28 年 9 月 26 日　放射線障害予防規程の変更（H28 年 10 月 21 日届出）
H28 年 9 月 28 日　規制庁による立入検査（指摘事項　なし）

## §2. 個人管理

### 2.1 放射線業務従事者登録

221 人（ 東北大 77 人 学外 128 人 研究者以外 16 人）

### 2.2 個人被ばく管理

1 年間の個人被ばく線量　　5 mSv 以下　221 人

### 2.3 教育訓練

定期講習

平成 28 年 8 月 5 日　登録前教育 8 人　再教育 62 人

特別講演の内容:

高エネルギー加速器研究機構　准教授　山崎 寛仁 氏

「大強度陽子加速器施設の放射線安全管理」

不定期の講習

再教育　24 回　51 人

登録前教育（新規教育）　31 回　105 人

## §3. 自主点検

年 2 回実施　　平成 28 年 9 月 21 日、平成 29 年 3 月 15 日

## §4. 放射性同位元素製造記録

2016 年度に本加速器施設で製造され，共同研究に使用された放射性同位元素は次の通りである。

| 核種 | 数量 (kBq) |
|---|---|
| Be-7 | 420 |
| C-11 | 10000 |
| F-18 | 1000 |
| Na-22 | 112.01 |
| Na-24 | 3005 |
| K-42 | 1400 |
| K-43 | 17000 |
| Ca-45 | 0.2 |
| Sc-46 | 6000 |
| Sc-47 | 3000 |
| V-48 | 400 |
| Cr-51 | 10020 |
| Ni-56 | 1000 |
| Ni-57 | 7500 |
| Co-58 | 20 |
| Cu-64 | 1000 |
| Zn-65 | 2 |
| Ga-67 | 1000 |
| Ga-68 | 3000 |
| Br-80 | 2000 |
| Rb-84 | 1000 |
| Sr-85 | 310 |
| Rb-86 | 1000 |
| Y-88 | 100 |
| Nb-95 | 500 |
| Mo-99 | 3504236.83 |
| Cd-115 | 20 |
| Cs-136 | 1000 |
| Cs-137 | 6000 |
| Pm-143 | 200 |
| Ta-182 | 1000 |
| Pb-203 | 70 |
| 全 32 核種 | 計 3583316.04 kBq |

# IV. List of Publication

# List of Publication (論文リスト) (2016)

## Papers Published in Refereed Journals

Proof-of-Principle Experiment of Velocity Bunching for Ultra-short Electron Pulse Production

S. Kashiwagi, S. Nagasawa, F. Hinode, T. Muto, H. Saito, T. Abe, K. Nanbu, I. Nagasawa, K. Takahashi, C. Tokoku, E. Kobayashi and H. Hama

Energy Procedia 89 (2016) 346–352.

High voltage threshold for stable operation in a dc electron gun

M. Yamamoto and N. Nishimori

Applied Physics Letters 109 (2016) 014103.

Enhanced diffraction of MeV $\gamma$-rays by mosaic crystals

S. Matsuba, T. Hayakawa, T. Shizuma, N. Nishimori, R. Nagai, M. Sawamura, C.T. Angell, M. Fujiwara, R. Hajima

Japanese Journal of Applied Physics 55 (2016) 112402.

Prospoects for Electron Scattering on Unstable, Exotic Nuclei (Review paper)

T. Suda and H. Simon

Progress of Particle and Nuclear Physics 96 (2017) 1–31.

極低運動量領域での電子・陽子弾性散乱による陽子荷電半径の精密決定

須田利美, 塚田暁

原子核研究 61 (2017) 87–98.

Spectroscopy of the neutron-rich hypernucleus ${}^{7}_{\Lambda}$He from electron scattering

T. Gogami, C. Chen, D. Kawama, P. Achenbach, A. Ahmidouch, I. Albayrak, D. Androic, A. Asaturyan, R. Asaturyan, O. Ates, P. Baturin, R. Badui, W. Boeglin, J. Bono, E. Brash, P. Carter, A. Chiba, E. Christy, S. Danagoulian, R. De Leo, D. Doi, M. Elaasar, R. Ent, Y. Fujii, M. Fujita, M. Furic, M. Gabrielyan, L. Gan, F. Garibaldi, D. Gaskell, A. Gasparian, Y. Han, O. Hashimoto, T. Horn, B. Hu, Ed. V. Hungerford, M. Jones, H. Kanda, M. Kaneta, S. Kato, M. Kawai, H. Khanal, M. Kohl, A. Liyanage, W. Luo, K. Maeda, A. Margaryan, P. Markowitz, T. Maruta, A. Matsumura, V. Maxwell, A. Mkrtchyan, H. Mkrtchyan, S. Nagao, S.N. Nakamura, A. Narayan, C. Neville, G. Niculescu, M.I. Niculescu, A. Nunez, Nuruzzaman, Y. Okayasu, T. Petkovic, J. Pochodzalla, X. Qiu, J. Reinhold, V.M. Rodriguez, C. Samanta, B. Sawatzky, T. Seva, A. Shichijo, V. Tadevosyan, L. Tang,, N. Taniya, K. Tsukada, M. Veilleux, W. Vulcan, F.R. Wesselmann, S.A. Wood, T. Yamamoto, L. Ya, Z. Ye, K. Yokota, L. Yuan, S. Zhamkochyan, and L. Zhu

Phys. Rev. C 94 (2016) 021302.

Ground-state binding energy of ${}^{4}_{\Lambda}$H from high-resolution decay-pion spectroscopy

F. Schulz, P. Achenbach, S. Aulenbacher, J. Beričič, S. Bleser, R. Böhm, D. Bosnard, L. Correa,

M.O. Distler, A. Esser, H. Fonvieille, I. Friščič, Y. Fujii, M. Fujita, T. Gogami, H. Kanda, M. Kaneta, S. Kegel, Y. Kohl, W. Kusaka, A. Margaryan, H. Merkel, M. Mihovilovič, U. Müller, S. Nagao, S.N. Nakamura, J. Pochodzalla, A. Sanchez Lorente, B.S. Schlimme, M. Schoth, C. Sfienti, S. Širca, M. Steinen, c, Y. Takahashi, L. Tang, M. Thiel, K. Tsukada, A. Tyukin, A. Weber

Nucl. Phys. A954 (2016) 149–160.

Structure near the $K^- + p + p$ threshold in the in-flight $^3$He($\boldsymbol{K}^-$,$\Lambda\boldsymbol{p}$)n reaction

Y. Sada, S. Ajimura, M. Bazzi, G. Beer, H. Bhang, M. Bragadireanu, P. Buehler, L. Busso, M. Cargnelli, S. Choi, C. Curceanu, S. Enomoto, D. Faso, H. Fujioka, Y. Fujiwara, T. Fukuda, C. Guaraldo, T. Hashimoto, R.S. Hayano, T. Hiraiwa, M. Iio, M. Iliescu, K. Inoue, Y. Ishiguro, T. Ishikawa, S. Ishimoto, T. Ishiwatari, K. Itahashi, M. Iwai, M. Iwasaki, Y. Kato, S. Kawasaki, P. Kienle, H. Kou, Y. Ma, J. Marton, Y. Matsuda, Y. Mizoi, O. Morra, T. Nagae, H. Noumi, H. Ohnishi, S. Okada, H. Outa, K. Piscicchia, A. Romero Vidal, A. Sakaguchi, F. Sakuma, M. Sato, A. Scordo, M. Sekimoto, H. Shi, D. Sirghi, F. Sirghi, K. Suzuki, S. Suzuki, T. Suzuki, K. Tanida, H. Tatsuno, M. Tokuda, D. Tomono, A. Toyoda, K. Tsukada, O. Vazquez Doce, E. Widmann, B.K. Wuenschek, T. Yamaga, T. Yamazaki, H. Yim, Q. Zhang, J. Zmeskal

Prog. Theor. Exp. Phys. 2017, 051D01.

Studies of high density baryon matter with high intensity heavy-ion beams at J-PARC

H. Sako, H. Harada, T. Sakaguchi, T. Chujo, S. Esumi, T. Gunji, S. Hasegawa, S.H. Hwang, Y. Ichikawa, K. Imai, K. Itakura, M. Kaneta, B.C. Kim, M. Kinsho, M. Kitazawa, Y. Liu, H. Masui, S. Nagamiya, K. Nishio, M. Okamura, K. Oyama, K. Ozawa, P.K. Saha, A. Sakaguchi, S. Sato, K. Shigaki, H. Sugimura, K. Tanida, J. Tamura, H. Tamura, Y. Nara, T.R. Saito (J-PARC Heavy-Ion Collaboration)

Nucl. Phys. A956 (2016) 850–853.

Limonene enhances the cAMP response element (CRE)-dependent transcriptional activity activated via adenosine A2A receptor in a neural-crest derived cell line, PC-12

J. Takito, M. Ota, C. Oba, H. Fujiwara, K. Murata, K. Yamaguchi, N. Uozumi, M. Nakamura, H. Inomata and Y. Ohizumi

Planta Medica International Open 2016, 3:e60–e62.

The topogenic function of S4 promotes membrane insertion of the voltage-sensor domain in the KvAP channel

E. Mishima, Y. Sato, K. Nanatani, N. Hoshi, J-K. Lee, N. Schiller, G. von Heijne, M. Sakaguchi, and N. Uozumi

Biochem. J. 473 (2016) 4361–4372.

Ion channels in plant bioenergetic organelles chloroplast and mitochondria: from molecular identification to function

L. Carraretto, E. Teardo, V. Checchetto, G. Finazzi, N. Uozumi, and I. Szabo

Mol. Plant 9 (2016) 371–395.

Involvement of potassium transport systems in the response of Synechocystis PCC 6803 cyanobactria to external pH change, high-intensity light sress and heavy metal stress

V. Checchetto, A. Sgalla, Y. Sato, E. Bergantine, I. Szabo and N. Uozumi

Plant Cell Physiol. 57 (2016) 862–877.

Nerve growth factor enhances the CRE-dependent transcriptional activity activated by nobiletin in PC-12 cells

J. Takito, J. Kimura, K. Kajima, N. Uozumi, M. Watanabe, A. Yokosuka, Y. Mimaki, M. Nakamura, and Y. Ohizumi

Can. J. Physiol. Pharm. 94 (2016) 728–733.

Calculation of resonance states of positronic lithium atom

T. Yamashita, Y. Kino

Eur. Phys. J. D 70 (2016) 190–198.

Analysis of plasma protein concentrations and enzyme activities in cattle within the ex-evacuation zone of the Fukushima Daiichi Nuclear Plant accident

Y. Urushihara, K. Kawasumi, S. Endo, K. Tanaka, Y. Hirakawa, G. Hayashi, T. Sekine, Y. Kino, Y. Kuwahara, M. Suzuki, M. Fukumoto, H. Yamashiro, Y. Abe, T. Fukuda, H. Shinoda, E. Isogai, T. Arai, M. Fukumoto

PLoS ONE 11 (2016) e0155069.

$^{90}$Sr in teeth of cattle abandoned in evacuation zone: Record of pollution from the Fukushima-Daiichi Nuclear Power Plant accident

K. Koarai, Y. Kino, A. Takahashi, T. Suzuki, Y. Shimizu, M. Chiba, K. Osaka, K. Sasaki, T. Fukuda, E. Isogai, H. Yamashiro, T. Oka, T. Sekine, M. Fukumoto, H. Shinoda

Scientific Reports, 6 (2016) 24077.

Software development for estimating the concentration of radioactive cesium in the skeletal muscles of cattle from blood samples

T. Fukuda, M. Hiji, Y. Kino, Y. Abe, H. Amashiro, J. Kabayashi, Y. Shimizu, A. Takahashi, T. Suzuki, M. Chiba, K. Inoue, Y. Kuwahara, M. Morimoto, M. Katayama, K. Donai, H. Shinoda, T. Sekine, M. Fukumoto, E. Isogai

Animal Science Journal, 87 (2016), 842–847.

陽電子が拓く物質の科学 第 2 回 陽電子・原子間相互作用と陽電子原子

木野康志, 山下琢磨

しょうとつ 13 (2016) 37-46.

相対論効果を含む陽電子アルカリ原子の弱束縛状態の高精度計算

山下琢磨, 木野康志

陽電子科学 6 (2016) 35-44.

Evolution of fusion hindrance for asymmetric systems at deep sub-barrier energies

A. Shrivastava, K. Mahata, S.K. Pandit, V. Nanal, T. Ichikawa, K. Hagino, A. Navin, C.S. Palshetkar, V.V. Parkar, K. Ramachandran, P.C. Rout, Abhinav Kumar, A. Chatterjee, and S. Kailas

Phys. Lett. B755 (2016) 332–336.

Low-energy hypernuclear spectra with microscopic particle-rotor model with relativistic point coupling hyperon-nucleon interaction

H. Mei, K. Hagino, J.M. Yao, and T. Motoba

Phys. Rev. C 93 (2016) 044307.

Investigating mult-channel quantum tunneling in heavy-ion fusion reactions with Bayesian spectral deconvolution

K. Hagino

Phys. Rev. C 93 (2016) 061601(R).

Anharmonicity of multi-octupole-phonon excitations in $^{208}$Pb: analysis with multi-reference covariant density functional theory and subbarrier fusion of $^{16}$O+$^{208}$Pb

J.M. Yao and K. Hagino

Phys. Rev. C 94 (2016) 011303(R).

New concept for pairing anti-halo effect as a localized wave packet of quasi-particle

K. Hagino and H. Sagawa

Phys. Rev. C 95 (2017) 024304.

The FOREST detector for meson photoproduction experiments at ELPH

T. Ishikawa, H. Fujimura, H. Fukasawa, R. Hashimoto, T. Ishida, S. Kaida, J. Kasagi, A. Kawano, S. Kuwasaki, K. Maeda, F. Miyahara, K. Mochizuki, T. Nakabayashi, A. Nakamura, K. Nawa, S. Ogushi, Y. Okada, K. Okamura, Y. Onodera, Y. Saito, Y. Sakamoto, M. Sato, H. Shimizu, H. Sugai, K. Suzuki, S. Takahashi, Y. Tsuchikawa, H. Yamazaki, H. Yonemura

Nucl. Instr. Meth. A832 (2016) 108–143.

Testing a prototype BGO calorimeter with 100–800 MeV positron beams

T. Ishikawa, H. Fujimura, D.N. Grigoriev, R. Hashimoto, S. Kaida, R. Kitazawa, G.N. Kuznetsov, A. Nakamura, H. Shimizu, K. Suzuki, S. Takahashi, Y. Tsuchikawa, Ya.V. Vasiliev, H. Yamazaki

Nucl. Instr. Meth. A837 (2016) 109–122.

An event mixing technique for Bose-Einstein correlations of two pions in photoproduction around 1 GeV

Q. He, H. Fujimura, H. Fukasawa, R. Hashimoto, Y. Honda, T. Ishikawa, T. Iwata, S. Kaida, J. Kasagi, A. Kawano, S. Kuwasaki, K. Maeda, S. Masumoto, M. Miyabe, F. Miyahara, K. Mochizuki, N. Muramatsu, A. Nakamura, K. Nawa, S. Ogushi, Y. Okada, Y. Onodera, K. Ozawa, Y. Sakamoto, M. Sato, H. Shimizu, H. Sugai, K. Suzuki, Y. Tajima, S. Takahashi, Y. Taniguchi, Y. Tsuchikawa, H. Yamazaki, R. Yamazaki, H.Y. Yoshida

Chinese Phys. C40 (2016) 114002.

Interference Effect between $\phi$ and $\Lambda(1520)$ Production Channels in the $\gamma p \to K^+K^-p$ Reaction near Threshold

S.Y. Ryu, J.K. Ahn, T. Nakano, D.S. Ahn, S. Ajimura, H. Akimune, Y. Asano, W.C. Chang, J.Y. Chen, S. Date, H. Ejiri, H. Fujimura, M. Fujiwara, S. Fukui, S. Hasegawa, K. Hicks,

K. Horie, T. Hotta, S.H. Hwang, K. Imai, T. Ishikawa, T. Iwata, Y. Kato, H. Kawai, K. Kino, H. Kohri, Y. Kon, N. Kumagai, P.J. Lin, Y. Maeda, S. Makino, T. Matsuda, N. Matsuoka, T. Mibe, M. Miyabe, M. Miyachi, Y. Morino, N. Muramatsu, R. Murayama, Y. Nakatsugawa, S.I. Nam, M. Niiyama, M. Nomachi, Y. Ohashi, H. Ohkuma, T. Ohta, T. Ooba, D.S. Oshuev, J.D. Parker, C. Rangacharyulu, A. Sakaguchi, T. Sawada, P.M. Shagin, Y. Shiino, H. Shimizu, E.A. Strokovsky, Y. Sugaya, M. Sumihama, A.O. Tokiyasu, Y. Toi, H. Toyokawa, T. Tsunemi, M. Uchida, M. Ungaro, A. Wakai, C.W. Wang, S.C. Wang, K. Yonehara, T. Yorita, M. Yoshimura, M. Yosoi, R.G.T. Zegers (LEPS Collaboration)

Phys. Rev. Lett. 116 (2016) 232001.

A study of event mixing for two-pion Bose-Einstein correlations in the $\gamma p \to \pi^0\pi^0 p$ reaction

Q. He, J. Ai, T. Ishikawa, T. Li, L. Ma, J. Ma, M. Miyabe, N. Muramatsu, H. Shimizu, Y. Tsuchikawa, Y. Xiang, H. Yamazaki, Y. Zhang

Prog. Theor. Exp. Phys. 2017, 033D02.

Virtual Institute for Quark Nuclear Physics at SPring-8/LEPS2

H. Shimizu and N. Muramatsu

Nuclear Physics News 27:1 (2017) 19–22.

Near threshold angular distributions for the $^2$H($\gamma$,$\Lambda$)X reaction

B. Beckford, P. Bydzovsky, A. Chiba, D. Doi, T. Fujii, Y. Fujii, K. Futatsukawa, T. Gogami, O. Hashimoto, Y.C. Han, K. Hirose, R. Honda, K. Hosomi, T. Ishikawa, H. Kanda, M. Kaneta, Y. Kaneko, S. Kato, D. Kawama, C. Kimura, S. Kiyokawa, T. Koike, K. Maeda, K. Makabe, M. Matsubara, K. Miwa, S. Nagao, S.N. Nakamura, A. Okuyama, K. Shirotori, K. Sugihara, K. Suzuki, T. Tamae, H. Tamura, K. Tsukada, F. Yamamoto, T.O. Yamamoto, F. Yonemoto, and H. Yamazaki

Prog. Theor. Exp. Phys. 2016, 063D01.

High resolution spectroscopic study of $^{10}_{\Lambda}$Be

T. Gogami, C. Chen, D. Kawama, P. Achenbach, A. Ahmidouch, I. Albayrak, D. Androic, A. Asaturyan, R. Asaturyan, O. Ates, P. Baturin, R. Badui, W. Boeglin, J. Bono, E. Brash, P. Carter, A. Chiba, E. Christy, S. Danagoulian, R. De Leo, D. Doi, M. Elaasar, R. Ent, Y. Fujii, M. Fujita, M. Furic, M. Gabrielyan, L. Gan, F. Garibaldi, D. Gaskell, A. Gasparian, Y. Han, O. Hashimoto, T. Horn, B. Hu, E.V. Hungerford, M. Jones, H. Kanda, M. Kaneta, S. Kato, M. Kawai, H. Khanal, M. Kohl, A. Liyanage, W. Luo, K. Maeda, A. Margaryan, P. Markowitz, T. Maruta, A. Matsumura, V. Maxwell, A. Mkrtchyan, H. Mkrtchyan, S. Nagao, S.N. Nakamura, A. Narayan, C. Neville, G. Niculescu, M.I. Niculescu, A. Nunez, Nuruzzaman, Y. Okayasu, T. Petkovic, J. Pochodzalla, X. Qiu, J. Reinhold, V.M. Rodriguez, C. Samanta, B. Sawatzky, T. Seva, A. Shichijo, V. Tadevosyan, L. Tang, N. Taniya, K. Tsukada, M. Veilleux, W. Vulcan, F.R. Wesselmann, S.A. Wood, T. Yamamoto, L. Ya, Z. Ye, K. Yokota, L. Yuan, S. Zhamkochyan, and L. Zhu (HKS(JLab E05-5) Collaboration)

Phys. Rev. C 93, (2016), 034314.

High precision momentum calibration of the magnetic spectrometers at MAMI for hypernuclear binding energy determination

A. Margaryan, J.R.M. Annand, P. Achenbach, R. Ajvazyan, H. Elbakyan, R. Montgomery, S.N. Nakamura, J. Pochodzalla, F. Schulz, Y. Toyama, S. Zhamkochyan

Nucl. Instr. Meth. A846 (2017) 98–105.

ストレンジネス核物理

中村哲

原子核研究 60 supp.1 (2016 夏の学校特集号) 17-21.

Transverse energy production and charged-particle multiplicity at midrapidity in various systems from $\sqrt{s_{NN}} = 7.7$ to 200 GeV

A. Adare, et al. (PHENIX Collaboration)

Phys. Rev. C 93 (2016) 024901.

Scaling properties of fractional momentum loss of high-pT hadrons in nucleus-nucleus collisions at $\sqrt{s_{NN}}$ from 4 GeV to 6 TeV

A. Adare, et al. (PHENIX Collaboration)

Phys. Rev. C 93 (2016) 024911.

凝縮系核反応研究の現状と今後 ～ 革新的放射性元素変換技術の開発に向けて ～

岩村康弘

電気評論 2016 年 7 月号 42-46.

Screening energy of the D+D reaction in an electron plasma deduced from cooperating colliding reaction

J. Kasagi and Y. Honda

J. Condensed Matter Nucl. Sci. 19 (2016) 127–134.

Astrophysical S factor for the $^{6}$Li($d$,$\alpha$)$^{4}$He and $^{6}$Li($d$,$p0/p1$)$^{7}$Li reactions and their astrophysical implications

K. Fang, J. Zou, H. He, Q. Wang, J. Zhao, T. Wang, and J. Kasagi

Phys. Rev. C 94 (2016) 054602.

## Papers Published in International Conference Proceedings

Status of the 1.3 GeV Booster Synchrotron for Generating High Energy Gamma Rays at Tohoku University

F. Hinode, H. Hama, S. Kashiwagi, T. Muto, I. Nagasawa, K. Nanbu, Y. Shibasaki, K. Takahashi, C. Tokoku

Proc. of IPAC2016 (2016) 701–703.

Generation of Coherent Undulator Radiation using Extremely Short Electron Bunch at t-ACTS, Tohoku University

S. Kashiwagi, T. Abe, H. Hama, F. Hinode, T. Muto, I. Nagasawa, K. Nanbu, H. Saito, Y. Shibasaki, K. Takahashi, C. Tokoku

Proc. of IPAC2016 (2016) 1760–1762.

Production of Ultra-short Electron Pulse and Observation of Coherent Transition Radiation at t-ACTS, Tohoku University

T. Abe, H. Hama, F. Hinode, S. Kashiwagi, T. Muto, I. Nagasawa, K. Nanbu, H. Saito, Y. Shibasaki, K. Takahashi, C. Tokoku

Proc. of IPAC2016 (2016) 1763–1765.

Profile Measurements of Bremsstrahlung Gamma-Rays from Tungsten Plates for Radioactive Isotope Production via Photonuclear Reaction using a 60 MeV Electron Linac

K. Takahashi, H. Hama, F. Hinode, S. Kashiwagi, H. Kikunaga, T. Muto, I. Nagasawa, K. Nanbu, Y. Shibasaki, T. Suda, C. Tokoku, K. Tsukada

Proc. of IPAC2016 (2016) 1766–1768.

Development Status of Linear Focal Cherenkov Ring Camera

K. Nanbu, T. Abe, H. Hama, F. Hinode, S. Kashiwagi, T. Muto, I. Nagasawa, H. Saito, K. Takahashi, C. Tokoku

Proc. of IPAC2016 (2016) 152–154.

Generation of Coherent Undulator Radiation at ELPH, Tohoku University

S. Kashiwagi, T. Abe, H. Hama, F. Hinode, T. Muto, K. Nanbu, I. Nagasawa, H. Saito, Y. Saito, Y. Shibasaki, K. Takahashi

Proc. of LINAC2016 (2016) 316–318.

ELECTRON DRIVEN ILC POSITRON SOURCE WITH A LOW GRADIENT CAPTURE LINAC

M. Kuriki, T. Kakita, T. Takahashi, K. Negishi, T. Okugi, T. Omori, M. Satoh, Y. Seimiya, J. Urakawa, K. Yokoya, S. Kashiwagi

Proc. of LINAC2016 (2016) 430–433.

SIX-DIMENSIONAL PHASE-SPACE ROTATION AND ITS APPLICATIONS

M. Kuriki, K. Negishi, H. Hayano, R. Kato, K. Ohmi, M. Satoh, Y.Seimiya, J. Urakawa and S. Kashiwagi

Proc. of IPAC2016 (2016) 1754–1756.

DC Photoemission Gun Upgrade at the Compact ERL

N. Nishimori, R. Hajima, R. Nagai, M. Mori, M. Yamamoto, Y. Honda, T. Miyajima, T. Uchiyama

Proc. of IPAC2016, Busan, Korea, THPOW008, 3944–3946.

Recent Developments and Operational Status of the Compact ERL at KEK

T. Obina, M. Adachi, S. Adachi, T. Akagi, M. Akemoto, D.A. Arakawa, S. Araki, S. Asaoka, M. Egi, K. Enami, K. Endo, S. Fukuda, T. Furuya, K. Haga, K. Hara, K. Harada, T. Honda, Y. Honda, H. Honma, T. Honma, K. Hosoyama, K. Hozumi, A. Ishii, X.J. Jin, E. Kako, Y. Kamiya, H. Katagiri, R. Kato, H. Kawata, Y. Kobayashi, Y. Kojima, Y. Kondo, T. Konomi, A. Kosuge, T. Kume, T. Matsumoto, H. Matsumura, H. Matsushita, S. Michizono, T. Miura, T. Miyajima, H. Miyauchi, S. Nagahashi, H. Nakai, H. Nakajima, N. Nakamura, K. Nakanishi, K. Nakao, K.N. Nigorikawa, T. Nogami, S. Noguchi, S. Nozawa, T. Ozaki, F. Qiu, H. Sagehashi, H. Sakai, S. Sakanaka, S. Sasaki, K. Satoh, Y. Seimiya, T. Shidara, M. Shimada,

K. Shinoe, T. Shioya, T. Shishido, M. Tadano, T. Tahara, T. Takahashi, R. Takai, H. Takaki, T. Takenaka, O. Tanaka, Y. Tanimoto, N. Terunuma, M. Tobiyama, K. Tsuchiya, T. Uchiyama, A. Ueda, K. Umemori, J. Urakawa, K. Watanabe, M. Yamamoto, N. Yamamoto, Y. Yamamoto, Y. Yano, M. Yoshida, R. Hajima, M. Mori, R. Nagai, N. Nishimori, M. Sawamura, T. Shizuma, M. Kuriki

Proc. of IPAC2016, Busan, Korea, THPOW036, 1835–1838.

Spectroscopic Experiment of Λ(1405) via the In-flight d($K^-$,$n$) Reaction at J-PARC K1.8BR

S. Kawasaki, S. Ajimura, G. Beer, H. Bhang, M. Bragadireanu, P. Buehler, L. Busso,, M. Cargnelli, S. Choi, C. Curceanu, S. Enomoto, D. Faso,, H. Fujioka, Y. Fujiwara, T. Fukuda, C. Guaraldo, T. Hashimoto, R. Hayano, T. Hiraiwa, M. Iio, M. Iliescu, K. Inoue, T. Ishikawa, S. Ishimoto, K. Itahashi, M. Iwai, M. Iwasaki,, P. Kienlep, H. Kou, Y. Ma, J. Marton, Y. Matsuda, H. Mizoi, O. Morra, T. Nagae, H. Noumi, H. Ohnishi,, S. Okada, H. Outa, D. Pietreanu, Y. Sada, A. Sakaguchi, F. Sakuma, M. Sato, M. Sekimoto, H. Shi, K. Shirotori, D. Sirghi,, F. Sirghi, K. Suzuki, S. Suzuki, T. Suzuki, K. Tanida, H. Tatsuno, M. Tokuda, M. Tomono, A. Toyoda, K. Tsukada, E. Widmann, T. Yamaga, K. Yoshida, T. Yamazaki,, H. Yim, Q. Zhang, and J. Zmeskal

JPS Conf.Proc. 13 (2017) 020018.

Study of the elementary ($K^-$,$n$) reactions to search for the K$^-$NN bound state via the $^3$He($K^-$,$n$) reaction at J-PARC

T. Yamaga, S. Ajimura, G. Beer, C. Berucci, H. Bhang, M. Bragadireanu, P. Buehler, L. Busso, M. Cargnelli, S. Choi, C. Curceanu, S. Enomoto, D. Faso, H. Fujioka, Y. Fujiwara, T. Fukuda, C. Guaraldo, T. Hashimoto, R.S. Hayano, T. Hiraiwa, M. Iio, M. Iliescu, K. Inoue, Y. Ishiguro, T. Ishikawa, S. Ishimoto, T. Ishiwatari, K. Itahashi, M. Iwai, M. Iwasaki,, K. Kanno, K. Kato, Y. Kato, S. Kawasaki1, P. Kienle, T. Kim, H. Kou, Y. Ma, J. Marton, Y. Matsuda, Y. Mizoi, O. Morra, T. Nagae, H. Noumi, H. Ohnishi, S. Okada, H. Outa, K. Piscicchia, A. Romero Vidal, Y. Sada, A. Sakaguchi1, F. Sakuma, M. Sato, A. Scordo, M. Sekimoto, H. Shi, K. Shirotori, D. Sirghi,, F. Sirghi,, K. Suzuki, S. Suzuki, T. Suzuki, K. Tanida, H. Tatsuno, M. Tokuda, D. Tomono, A. Toyoda, K. Tsukada, O. Vazquez Doce, E. Widmann, B.K. Wuenschek, T. Yamazaki, H. Yim, Q. Zhang, and J. Zmeskal

AIP Conf. Proc. 1735 (2016) 040007.

Study of the K$^-$-Nucleus Interaction by Using the $^{12}$C($K^-$,$p$) Reaction at J-PARC

Y. Ichikawa, J.K. Ahn, Y. Akazawa, K. Aoki, E. Botta, H. Ekawa, P. Evtoukhovitch, A. Feliciello, M. Fujita, T. Gogami, S. Hasegawa, T. Hasegawa, S. Hayakawa, T. Hayakawa, R. Honda, K. Hosomi, K. Imai, W.S. Jung, S. Kanatsuki, S.H. Kim, S. Kinbara, K. Kobayashi, J.Y. Lee, S. Marcello, K. Miwa, T.J. Moon, T. Nagae, Y. Nakada, M. Nakagawa, T. Nanamura, M. Naruki, A. Sakaguchi, H. Sako, S. Sato, Y. Sasaki, K. Shirotori, H. Sugimura, T. Takahashi, H. Tamura, K. Tanida, Z. Tsamalaidze, M. Ukai, and T.O. Yamamoto

JPS Conf. Proc. 13 (2017) 020007.

Present status of coupled-channels calculations for heavy-ion subbarrier fusion reactions

K. Hagino and J.M. Yao

EPJ Web of Conferences 117 (2016) 08003.

Recent developments in heavy-ion fusion reactions around the Coulomb barrier

K. Hagino, N. Rowley, and J.M. Yao

EPJ Web of Conferences 122 (2016) 07002.

Fission life-time calculation using a complex absorbing potential

G. Scamps and K. Hagino

EPJ Web of Conferences 122 (2016) 01004.

Three-body model for nuclei near and beyond drip line

H. Sagawa and K. Hagino

Acta Phys. Polon. Supp. 10 (2017) 211–224.

The basic performance of the TOF-RPC for the BGOegg experiment

N. Tomida, N. Tran, M. Niiyama, H. Ohnishi and N. Muramatsu

Proc. of RPC2016; J. of Instr. 11 (2016) C11037.

$\eta$n Scattering Length from the $\gamma d \to p\eta n$ Reaction at $E_\gamma \sim 0.9$ GeV

T. Ishikawa, H. Fujioka, Y. Honda, T. Hotta, Y. Inoue, K. Itahashi, H. Kanda, H. Kawai, K. Maeda, M. Miyabe, S. Miyata, Y. Matsumura, N. Muramatsu, H. Ohnishi, K. Ozawa, M. Sasagawa, H. Shimizu, K. Shiraishi, M. Tabata, A.O. Tokiyasu, and Y. Tsuchikawa

Proc. of 14th International Conference on Meson-Nucleon Physics and the Structure of the Nucleon (MENU2016), JPS Conf. Proc. 13 (2017) 020031.

Simultaneous Photoproduction Of Neutral And Charged Pions On The Deuteron At ELPH

T. Ishikawa, A. Nakamura, H. Fujimura, R. Hashimoto, Q. He, S. Kaida, M. Miyabe, N. Muramatsu, H. Shimizu, K. Suzuki, Y. Tschikawa, H. Yamazaki, R. Yamazaki, S. Masumoto, Y. Obara, K. Maeda, K. Ozawa

Proc. of the 26th International Nuclear Physics Conference (INPC), PoS(INPC2016)267.

$\eta$n scattering length from $\gamma d \to p\eta n$ at $E_\gamma \sim 0.93$ GeV

T. Ishikawa, H. Fujioka, Y. Honda, T. Hotta, Y. Inoue, K. Itahashi, H. Kanda, H. Kawai, K. Maeda, M. Miyabe, S. Miyata, Y. Matsumura, N. Muramatsu, H. Ohnishi, K. Ozawa, M. Sasagawa, H. Shimizu, K. Shiraishi, M. Tabata, A.O. Tokiyasu, Y. Tsuchikawa

Proc. of the international symposium on Neutron Star Matter 2016 (NSMAT2016).

Application of an X-Ray Flat Panel Sensor to a GeV Region Gamma-Ray Beam Profile Monitor

H. Kanda, K. Honda, T. Ishikawa, M. Kaneta, K. Maeda, M. Miyabe, Y. Muroi, S.N. Nakamura, A. Ninomiya, Y. Obara, K. Ozawa, K. Ozeki, T. Sasaki, H. Shimizu, A.O. Tokiyasu

Conference Record of IEEE Nuclear Science Symposuim & Medical Imaging Conference 2016.

Development of a high-intensity photon-beam profile monitor

T. Ishikawa, H. Fujimura, R. Hashimoto, Y. Honda, T. Ishida, H. Kanda, S. Kido, Y. Matsumura, M. Miyabe, I. Nagasawa, K. Nanbu, H. Shimizu, K. Suzuki, K. Takahashi, A.O. Tokiyasu, Y. Tsuchikawa, H. Yamazaki

Conference Record of IEEE Nuclear Science Symposuim & Medical Imaging Conference 2016.

Study of the d($\gamma$,$K^+$)$\Sigma\pi$N Reaction at LEPS

A.O. Tokiyasu

JPS Conf. Proc. 13 (2017) 020017.

Near Threshold $K^0\Lambda$ Photoproduciton on the Neutron Studied with an Electromagnetic Calorimeter FOREST

Y. Tsuchikawa, H. Fujimura, H. Fukasawa, R. Hashimoto, Q. He, Y. Honda, T. Ishikawa, T. Iwata, S. Kaida, J. Kasagi, A. Kawano, S. Kuwasaki, K. Maeda, S. Masumoto, M. Miyabe, F. Miyahara, K. Mochizuki, N. Muramatsu, A. Nakamura, K. Nawa, S. Ogushi, Y. Okada, Y. Onodera, K. Ozawa, Y. Sakamoto, M. Sato, H. Shimizu, H. Sugai, K. Suzuki, Y. Tajima, S. Takahashi, Y. Taniguchi, H. Yamazaki, R. Yamazaki, and H. Y. Yoshida

JPS Conf. Proc. 10 (2016) 032010.

Meson Photoproduction Experiments at ELPH, Tohoku University

T. Ishikawa, H. Fujimura, H. Fukasawa, R. Hashimoto, Q. He, Y. Honda, T. Iwata, S. Kaida, J. Kasagi, A. Kawano, S. Kuwasaki, K. Maeda, S. Masumoto, M. Miyabe, F. Miyahara, K. Mochizuki, N. Muramatsu, A. Nakamura, K. Nawa, S. Ogushi, Y. Okada, Y. Onodera, K. Ozawa, Y. Sakamoto, M. Sato, H. Shimizu, H. Sugai, K. Suzuki, Y. Tajima, S. Takahashi, Y. Taniguchi, Y. Tsuchikawa, H. Yamazaki, R. Yamazaki, and H.Y. Yoshida (the FOREST Collaboration)

JPS Conf. Proc. 10 (2016) 031001.

Double neutral pion photoproduction off the proton with FOREST at ELPH

Q. He, H. Fujimura, H. Fukasawa, R. Hashimoto, Y. Honda, T. Ishikawa, T. Iwata, S. Kaida, J. Kasagi, A. Kawano, S. Kuwasaki, K. Maeda, S. Masumoto, M. Miyabe, F. Miyahara, K. Mochizuki, N. Muramatsu, A. Nakamura, K. Nawa, S. Ogushi, Y. Okada, Y. Onodera, K. Ozawa, Y. Sakamoto, M. Sato, H. Shimizu, H. Sugai, K. Suzuki, Y. Tajima, S. Takahashi, Y. Taniguchi, Y. Tsuchikawa, H. Yamazaki, R. Yamazaki and H.Y. Yoshida

EPJ Web Conf. 109 (2016) 04004.

Experimental investigations of the hypernucleus ${}^{4}_{\Lambda}$H

P. Achenbach, F. Schulz, S. Aulenbacher, J. Beričič, S. Blese, R. Böhm, D. Bosnar, L. Correa, M.O. Distler, A. Esser, H. Fonvieille, I. Friščič, Y. Fujii, M. Fujita, T. Gogami, H. Kanda, M. Kaneta, S. Kegel, Y. Kohl, W. Kusaka, A. Margaryan, H. Merkel, M. Mihovilovič, U. Müller, S. Nagao, S.N. Nakamura, J. Pochodzalla, A. Sanchez Lorente, B.S. Schlimme, M. Schoth, C. Sfienti, S. Širca, M. Steinen, Y. Takahashi, L. Tang, M. Thiel, K. Tsukada, A. Tyukin and A. Weber (A1 Collaboration)

Proc. of FB21; EPJ Web of Conferences 113 (2016) 07001.

The Launch of a New Plan on Condensed Matter Nuclear Science at Tohoku University

Y. Iwamura, J. Kasagi, H. Kikunaga, H. Yoshino, T. Itoh, M. Hattori and T. Mizuno

J. Condensed Matter Nucl. Sci. 19 (2016) 119–126.

Anomalous Excess Heat Generated by the Interaction between Nano-structured Pd/Ni surface and $D_2$

gas

T. Itoh, Y. Iwamura, J. Kasagi, H. Shishido

Proc. of The 20th International Conference on Condensed Matter Nuclear Science (2017) 179–190.

## Invited Talk and Oral Presentations at International Conferences

SLiT-J, a high brilliant compact 3 GeV light source project in Japan (Oral presentation)

H. Hama

Canadian Light Source Laboratory, Saskatoon, Saskatchewan, Canada, Mar. 22, 2016.

Variable polarized narrowband THz source based on undulator super-radiant (Invited oral presentation)

H. Hama

Energy Materials Nanotechnology (EMN) Meeting on Teraherts, Donostia, Spain, May 16, 2016.

Expected performance of SLiT-J – at a glance – (Oral presentation)

H. Hama

International Review Committee Meeting of the SLiT-J project, Sendai, Japan, June 21, 2016.

Status of SLiT-J – a high brilliant compact 3 GeV light source project in Japan – (Oral presentation)

H. Hama

Low Emittance Rings Workshop 2016, Synchrotron SOLEIL, Gif-sur-Yvette Cedex, France, Oct. 26, 2016.

Demonstration of coherent radiation generation up to 3 THz from femtosecond electron pulses (Oral presentation)

H. Hama

13th Eco-Energy and Materials Science and Engineering Symposium (EMSES2016), Udorn Thani, Thailand, Dec. 2, 2016.

Latest beam physics activities at t-ACTS, Tohoku University (Oral presentation)

H. Hama

Plasma and Beam Physics Research Facility, Chiang Mai University, Chiang Mai, Thailand, Dec. 6, 2016.

Status of test-Accelerator as Coherent THz Source (t-ACTS) at ELPH, Tohoku University (Oral presentation)

S. Kashiwagi, T. Abe, F. Hinode, K. Kanomata, T. Muto, K. Nanbu, I. Nagasawa, H. Saito, Y. Saito, K. Takahashi and H. Hama

Workshop on THz FEL, Hefei, China, Dec. 22, 2016.

Implementation of an electron storage ring for GeV-gammma beam production via Bremsstrahlung in an internal target wire (Oral presentation)

T. Muto

The 1st International Workshop on CSR and free electron lasers from ultra short bunch elec-

tron beam, Uji Kyoto, Japan, Sep. 2, 2016.

Study of Cherenkov radiation from thin silica-aerogel (Oral presentation)

K. Nanbu, S. Kashiwagi, F. Hinode, T. Muto, I. Nagasawa, K. Takahashi, H. Saitoh, T. Abe, Y. Saitoh and H. Hama,

13th Eco-Energy and Materials Science and Engineering Symposium, Udonthani, Thailand, Dec. 2, 2016.

Demonstration of coherent radiation generation up to 3 THz from femtosecond electron pulses (Oral presentation)

T. Abe, S. Kashiwagi, F. Hinode, T. Muto, K. Nanbu, K. Takahashi, I. Nagasawa, K. kanomata, H. Saito, Y. Saito and H. Hama

13th Eco-Energy and Materials Science and Engineering Symposium, Udonthani, Thailand, Dec. 2, 2016.

Observation of coherent transition radiation from extremely short electron beam (Oral presentation)

T. Abe, S. Kashiwagi, F. Hinode, K. Kanomata, T. Muto, K. Nanbu, I. Nagasawa, H. Saito, Y. Saito, K. Takahashi and H. Hama

Workshop on THz FEL, Hefei, China, Dec. 22, 2016.

Coherent THz wave observed by a Michelson interferometer (Oral presentation)

T. Abe

The 1st International Workshop on CSR and free electron lasers from ultrashort bunch electron beam, Uji Kyoto, Japan, Sep. 1, 2016.

e+p project at ultra-low $Q^2$ in Japan (Invited oral)

T. Suda

ECT* workshop on the Proton Radius Puzzle, ECT*, Trento, Italy, June 20–24, 2016.

Future perspectives of the SCRIT facility (Invited oral)

T. Suda

Electron-radioactive ion collisions : theoretical and experimental challenges, Gif-sur-Yvette, France, Apr. 25–27, 2016.

SCRIT electron scattering facility : present status and future perspectives (Invited oral)

T. Suda

Neutron Skin of Nuclei, Mainz, Germany, May 17–27, 2016.

Electron scattering experiment off proton at ultra-low $Q^2$ (Invited oral)

T. Suda

Meson in Nuclei 2016, Kyoto, Japan, Aug. 1–3, 2016.

Electron scattering experiment off proton at ultra-low $Q^2$ (Invited oral)

T. Suda

Strangeness Nuclear Physics School 2016, Sendai, Japan, Nov. 18–20, 2016.

Electron scattering activities for nuclear physics in Japan (Seminar)

T. Suda

Seminar at Peking University, China, Mar. 20, 2016.

Electron scattering experiment off proton at ultra-low $Q^2$ (Seminar)

T. Suda

Seminar at Shandong University, China, Mar. 28, 2016.

Electron scattering off short-lived nuclei at SCRIT facility (Seminar)

T. Suda

Seminar at GANIL, CAEN, France, Apr. 29, 2016.

Electron scattering activities for nuclear physics in Japan (Seminar)

T. Suda

Seminar at IBS, Daejeon, Korea, Mar. 6, 2017.

Electron scattering activities for nuclear physics in Japan (Seminar)

T. Suda

Seminar at Seoul University, Seoul, Korea, Mar. 8, 2017.

First result from SCRIT electron scattering facility: Charge density distribution of $^{132}$Xe (Oral presentation)

K. Tsukada

International Nuclear Physics Conference, Adelaide Convention Centre, Australia, Sep. 11–16, 2016.

Experimental Approaches to Strangeness in Neutron Stars (Invited oral)

H. Tamura

14th International Symposium on Nuclei in the Cosmos (NIC14), Toki Messe, Niigata, Japan, June 19–24, 2016.

Recent Progress in Hypernuclear Physics (Invited oral)

H. Tamura

25th International Nuclear Physics Conference (INPC2016), Adelaide, Australia, Sep. 11–16, 2016.

Strangeness nuclear physics and neutron stars (Invited oral)

H. Tamura

Conference in the YIPQS long-term and Nishinomiya-Yukawa memorial workshop ”Compact stars and gravitational waves”, Yukawa Institute, Kyoto University, Kyoto, Japan, Oct. 31–Nov. 4, 2016.

Welcome address and the Neutron Star Matter project (Invited oral)

H. Tamura

International Symposium on Neutron Star Matter (NSMAT2016) − Recent Progress in Observations, Experiments and Theories −, Tohoku University, Sendai, Japan, Nov. 21–24, 2016.

Oxidative degradation of polyethylene studied by positron annihilation lifetime spectroscopy (Oral presentation)

T. Oka, K. Onodera, Y. Kino, T. Sekine

The 12th International symposium on Ionizing Radiation and Polymers (IRaP2016), Peninsula of Giens, France, Sep. 25–30, 2016.

Reactions with heavy nuclei (Invited oral)

K. Hagino

FRIB Theory Alliance Inaugural meeting, Michigan State University, U.S.A., Mar. 31–Apr. 1, 2016.

Di-neutron correlation and two-neutron decay of the $^{26}$O nucleus (Invited oral)

K. Hagino

YITP one-day workshop on NN and quartet correlations in nuclei, Yukawa Institute for Theoretical Physics, Kyoto, Japan, June 27, 2016.

Theoretical challenges in fusion reactions relevant to superheavy elements (Invited oral)

K. Hagino

RIBF Users meeting, RIKEN, Wako, Japan, Sep. 8–9, 2016.

Role of nn-correlations in the two-neutron decay of the $^{26}$O nucleus (Invited oral)

K. Hagino

ECT$^*$ workshop on Physics beyond the limits of stability: exploring the continuum, ECT$^*$, Trento, Italy, Oct. 17–21, 2016.

Di-neutron correlation and BCS-BEC crossover in the structure and decay of light neutron-rich nuclei (Oral presentation)

K. Hagino

International symposium on neutron star matter (NSMAT2016), Tohoku University, Sendai, Japan, Nov. 21–23, 2016.

Beyond-mean-field theory for multi-octupole excitations in $^{208}$Pb and subbarrier fusion of $^{16}$O+$^{208}$Pb (Invited oral)

K. Hagino

Tsukuba CCS-RIKEN joint workshop, RIKEN, Wako, Japan, Dec. 12–16, 2016.

Application of beyond-mean-field approach to hypernuclei and heavy-ion fusion reactions (Invited oral)

K. Hagino

YITP Molecule workshops on recent progress in nuclear structure physics 2016, Kyoto University, Kyoto, Japan, Dec. 5–23, 2016.

Semi-microscopic modelling of heavy-ion fusion reactions (Invited oral)

K. Hagino

Workshop on Low-Energy Nuclear Reaction Theory (LENRT), Australian National University, Canberra, Australia, Feb. 15–17, 2017.

Evolving theoretical descriptions of heavy-ion fusion: from phenomenlogical to microscopic approaches (Keynote speech)

K. Hagino

International conference on Fusion17, Hobart, Australia, Feb. 20–24, 2017.

BGOegg experiments at LEPS2 (Invited oral)

H. Shimizu

YITP Workshop – Meson in Nucleus, Yukawa Institute, Kyoto, Japan, Jul. 31–Aug. 2, 2016.

$\eta$n Scattering Length from the $\gamma d \to p\eta n$ Reaction at $E_\gamma \sim 0.9$ GeV (Oral presentation)

T. Ishikawa

14th International Conference on Meson-Nucleon Physics and the Structure of the Nucleon (MENU2016), Kyoto, Japan, July 25–30, 2016.

Simultaneous Photoproduction Of Neutral And Charged Pions On The Deuteron At ELPH (Oral presentation)

T. Ishikawa

The 26th International Nuclear Physics Conference (INPC), Adelaide, Australia, Sep. 11–16, 2016.

$\eta$n scattering length from $\gamma d \to p\eta n$ at $E_\gamma \sim 0.93$ GeV (Oral presentation)

T. Ishikawa

The international symposium on Neutron Star Matter 2016 (NSMAT2016), Sendai, Japan, Nov. 21–24, 2016.

Development of a high-intensity photon-beam profile monitor (Keynote speech)

T. Ishikawa

IEEE Nuclear Science Symposuim & Medical Imaging Conference, Strasbourg, France, Oct. 29–Nov. 5, 2016.

Study of baryon resonances and meson-nucleon interactions using photoproduction reactions at ELPH (Invited oral)

T. Ishikawa

2016 JAEA/ASRC Reimei Workshop: New exotic hadron matter at J-PARC, Inha University, Incheon, Korea, Oct. 24–26, 2016.

Recent status and futre prospect at the LEPS/LEPS2 experiment in Japan (Invited oral)

A.O. Tokiyasu

Many manifestations of nonperturbative QCD, Illhabela , Sao paulo, Brazil, May 1–7, 2016.

Study of the $d(\gamma, K^+)\Sigma\pi N$ reaction at LEPS (Oral presentation)

A.O. Tokiyasu

The 14th International conference on Meson-Nucleon Physics and the Structrue of the Nucleon, Kyoto, Japan, Jul 25–30, 2016.

$K^-pp$ bound state search at LEPS2 experiment (Oral presentation)

A.O. Tokiyasu

International Symposium on Neutron Star Matter, Sendai, Japan, Nov. 21–24, 2016.

Hypernuclear spectroscopy via the real photo-induced reaction (Oral presentation)

A.O. Tokiyasu

International workshop on Strangeness Nuclear Physics 2017, Osaka, Japan, Mar. 12–14, 2017.

The Hypernuclear Experimental Program (Invited oral)

S.N. Nakamura

ELBA XIV Workshop Lepton-Nucleus Scattering, Marciana Marina, Isola d'Elba, Italy, June 27–July 1, 2016.

Spectroscopy of Lambda Hypernuclei (Keynote speech)

S.N. Nakamura

Strangeness Nuclear Physics 2017, Osaka, Japan, Mar. 12–14, 2016.

The $\pi\pi$ and $\pi$d system in $\gamma d \to \pi^+\pi^- d$ measured with the NKS2 (Oral presentation)

H. Kanda

YITP workshop, Meson in Nuclei 2016 (MIN2016), Kyoto, Japan, Jul. 31–Aug. 2, 2016.

Application of an X-Ray Flat Panel Sensor to a GeV Region Gamma-Ray Beam Profile Monitor (Oral presentation)

H. Kanda

2016 IEEE Nuclear Science Symposium, Strasbourg, France, Oct. 29–Nov. 6, 2016.

Anomalous Heat Generation and Nuclear Transmutation Experiments at Condensed Matter Nuclear Reaction Division of Tohoku University (Invited oral)

Y. Iwamura

The Satellite Symposium of 20th International Conference on Condensed Matter Nuclear Science (SSICCF20), Xiamen University, Fujian, China, Sep. 27–30, 2016.

Replication Experiments at Tohoku University on Anomalous Heat Generation Using Nickel-Based Binary Nanocomposites and Hydrogen Isotope Gas (Oral presentation)

Y. Iwamura

The 20th International Conference on Condensed Matter Nuclear Science (ICCF20), Sendai, Japan, Oct 2–7, 2016.

Anomalous Heat Generation Experiments Using Metal Nanocomposites and Hydrogen Isotope Gas (Oral presentation)

Y. Iwamura

The 17th Japan CF-Research Society Meeting, National Institute of Technology, Tokyo College, Tokyo, Japan, Mar. 19–20, 2017.

Anomalous Excess Heat Generated by the Interaction between Nano-structured Pd/Ni surface and $D_2/H_2$ gas (Oral presentation)

T. Itoh

The 20th International Conference on Condensed Matter Nuclear Science (ICCF20), Sendai, Japan, Oct. 2–7, 2016.

Anomalous Excess Heat Generation by the Interaction between Nano-structured Pd/Ni surface and $D_2/H_2$ gas (Oral presentation)

T. Itoh

The 17th Meeting of Japan CF-Research Society, National Institute of Technology, Tokyo College, Tokyo, Japan, Mar. 19–20, 2017.

Observation of $^{141}$Pr by $^{40}$Ar scattering (RBS) on Cs implanted Pd/CaO multi-layer foil with $D_2$ gas permeation (Oral presentation)

J. Kasagi

The 20th International Conference on Condensed Matter nuclear Science (ICCF20), Sendai, Japan, Oct. 2–7, 2016.

Low-energy cooperative DD collision in liquid metal and electron screening effect (Oral presentation)

Y. Honda

The 20th International Conference on Condensed Matter nuclear Science (ICCF20), Sendai, Japan, Oct. 2–7, 2016.

## 学位論文 (電子光理学研究センター所属)

博士論文「Study of the low-energy d + d reaction in liquid metals」

本多 佑記，平成 28 年度，東北大学

修士論文 「極短電子ビームによるコヒーレントテラヘルツ放射の研究」

阿部 太郎, 平成 28 年度, 東北大学

修士論文 「電磁カロリメータと前方磁気スペクトロメータによる $\gamma d \to d\pi^0\pi^0$ 反応の研究」

井上 陽介, 平成 28 年度, 東北大学

修士論文 「FOREST Upgrade 実験のための MPPC を用いた位置検出器の開発」

白石 健一郎, 平成 28 年度, 東北大学

修士論文 「ラザフォード後方散乱法による Pd/CaO 多層膜票の質量分析」

田島 龍, 平成 28 年度, 東北大学

## 学位論文 (他機関所属)

修士論文「細分化された鉛ガラスを用いるカロリメータの電磁シャワーによる性能評価」

神崎 伊織,　平成 28 年度，信州大学

修士論文「鉛ガラスを吸収層とするストリップ型カロリメータの性能評価」

井藤 隼人,　平成 28 年度，信州大学

修士論文「SPring-8/LEPS2 のための MPPC Array を用いた beam profile の測定」

三木 克眞,　平成 28 年度，岐阜大学

修士論文「ニュートリノ反応測定実験に用いる高位置分解能 Scintillating Fiber Tracker の開発」

平本 綾美,　平成 28 年度，京都大学

修士論文「ハイパー核崩壊パイ中間子分光実験の系統誤差改善に向けた精密磁場測定」

冨田 翔子,　平成 28 年度，東北大学

修士論文「$^{3}_{\Lambda}$H の寿命測定実験のデザイン」

外山 裕一,　平成 28 年度，東北大学

修士論文「シグマ陽子散乱実験のための BGO カロリメータシステムの構築」
池田 迪彦, 平成 28 年度，東北大学
修士論文「Σp 散乱実験用エアロゲルチェレンコフ検出器の開発」
小林 和矢, 平成 28 年度，大阪大学

# V. Members of Committees

# Steering Committee

## 2016

| | |
|---|---|
| Hiroyuki HAMA* | ELPH |
| Hajime SHIMIZU | ELPH |
| Toshimi SUDA | ELPH |
| Fujio HINODE | ELPH |
| Shigeru KASHIWAGI | ELPH |
| Norihito MURAMATSU | ELPH |
| Hidetoshi KIKUNAGA | ELPH |
| Hirokazu TAMURA | Graduate School of Science |
| Satoshi NAKAMURA | Graduate School of Science |
| Kazushige MAEDA | Graduate School of Science |
| Kouichi HAGINO | Graduate School of Science |
| Fuminori MISAIZU | Graduate School of Science |
| Yasushi KINO | Graduate School of Science |
| Nobuyuki Uozumi | Graduate School of Engineering |
| Atsuki TERAKAWA | Graduate School of Engineering |
| Masaki FUJITA | Institute for Materials Research |
| Yuji TAKAKUWA | Institute of Multidisciplinary Research for Advanced Materials |
| Takeo EJIMA | Institute of Multidisciplinary Research for Advanced Materials |
| Keiichi EDAMATSU | Research Institute of Electrical Communication |
| Yasuhiro SAKEMI | Cyclotron and Radioisotope Center (until July 31) |
| Masatoshi ITOH | Cyclotron and Radioisotope Center (from Aug. 1) |
| Kenji TSUDA | Frontier Research Institute for Interdisciplinary Sciences |

* Chairperson

# General Advisory Committee

## 2016

| | |
|---|---|
| Hiroyuki HAMA* | ELPH |
| Hajime SHIMIZU | ELPH |
| Toshimi SUDA | ELPH |
| Hidetoshi KIKUNAGA | ELPH |
| Hirokazu TAMURA | Graduate School of Science, Tohoku University |
| Yasushi KINO | Graduate School of Science, Tohoku University |
| Yasuhiro SAKEMI | CYRIC, Tohoku University → CNS, University of Tokyo |
| Kenji TSUDA | Frontier Research Institute for Interdisciplinary Sciences, Tohoku University |
| Takahiro IWATA | Faculty of Science, Yamagata University |
| Daisuke JIDO | Graduate School of Science and Engineering, Tokyo Metropolitan University |
| Takashi NAKANO | RCNP, Osaka University |
| Tomohumi NAGAE | Graduate School of Science, Kyoto University |
| Hideaki OHGAKI | IAE, Kyoto University |
| Shigemi SASAKI | HSRC, Hiroshima University |
| Akihiko YOKOYAMA | College of Science and Engineering, Kanazawa University |
| Yasuji OURA | Graduate School of Science and Engineering, Tokyo Metropolitan University |

* Chairperson

# Program Advisory Committee

## 2016

| | |
|---|---|
| Hajime SHIMIZU | ELPH |
| Toshimi SUDA | ELPH |
| Satoshi Nakamura | Graduate School of Science, Tohoku University |
| Shigeru KASHIWAGI | ELPH |
| Hidetoshi KIKUNAGA | ELPH |
| Asao YAMAMURA | Institute for Materials Research, Tohoku University |
| Yasuhisa TAJIMA | Institute of Arts and Sciences, Yamagata University |
| Hiroaki OHNISHI | RIKEN Nishina Center |
| Toshiyuki TAKAHASHI * | IPNS, KEK |
| Yoshihiko SHOJI | LASTI, University of Hyogo |
| Yasuji OURA | Graduate School of Science and Engineering, Tokyo Metropolitan University |
| Koichi TAKAMIYA | Research Reactor Institute, Kyoto University |

* Chairperson

# VI. Approved Experiments

# 平成28年度前期採択課題一覧

| 課題番号 | 課　　題　　名 | 申込責任者 |
|---|---|---|
| 2836 | 光量子放射化法によるプロメチウム (Pm) 内包金属フラーレンの合成を目的とした RI 製造 II | 秋山和彦 |
| 2837 | シンチレーションファイバー検出器の性能評価のためのテスト実験 | 南野彰宏 |
| 2838 | J-PARC シグマ陽子散乱実験のためのエアロゲルチェレンコフカウンターの性能評価 | 三輪浩司 |
| 2839 | 光量子放射化分析のための光核反応収率の測定 (III) | 大浦泰嗣 |
| 2840 | Large Acceptance Multi-Purpose Spectrometer (LAMPS) Time Projection Chamber (TPC) Prototype Beam Test | Kim, Young Jin |
| 2841 | FOREST アップグレード実験のための位置検出型シンチレーション検出器の性能評価 | 時安敦史 |
| 2842 | SOI を用いた粒子軌跡測定用ピクセルセンサーの評価 | 坪山透 |
| 2843 | PWO ガンマ線検出器の性能評価 | 宮部学 |
| 2844 | FOREST 超前方荷電粒子検出で拓く物理 | 石川貴嗣 |
| 2845 | コンパクト BPM の開発 II | 石川貴嗣 |
| 2846 | 電子ライナックを用いた有用放射性トレーサー製造法の開発 | 菊永英寿 |
| 2847 | 第 4 周期元素の原子核半減期精密測定 | 菊永英寿 |
| 2848 | Photo-production of a Neutral Kaon and/or a Lambda Hyperon on a deuteron near the threshold | 金田雅司 |
| 2849 | イメージングプレートを用いた Ni-57 放射能強度分布測定による制動放射線プロファイル計測と分布測定補正用試料の作製 | 高橋健 |
| 2850 | NKS2 用標識化光子ビームの調整と標識化装置の改善 | 神田浩樹 |
| 2851 | $440 < E_\gamma < 720$ MeV における重水素原子核標的での $\pi^+\pi^-$ 光生成反応の研究 | 神田浩樹 |
| 2852 | J-PARC・E21 実験 (COMET) のための電子スペクトロメータの開発 | 西口創 |

# 平成28年度後期採択課題一覧

| 課題番号 | 課　　題　　名 | 申込責任者 |
|---|---|---|
| 2853 | 吸収体も読み出すサンドイッチ型カロリメータの性能検証 | 竹下徹 |
| 2854 | ニュートリノ実験のためのシンチレーションファイバー検出器の位置分解能評価 | 南野 彰宏 |
| 2855 | 4 年生学生実験：電子ビームによる放射化物生成及び放射線測定 | 塚田暁 |
| 2856 | ラジエータ挿入による BST リングのパラメータ測定 | 石川貴嗣 |
| 2857 | BST リングのビーム診断、および電子の速度と運動量 (第 5 回加速器ビームを使った原子核・素粒子実験実習スクール) | 石川貴嗣 |
| 2858 | J-PARC シグマ陽子散乱実験のためのエアロゲルチェレンコフカウンターの性能評価（２） | 三輪浩司 |
| 2859 | NKS2 電磁石中での Multi-gap Resistive Plate Chamber の性能評価 | 金田雅司 |
| 2860 | A Direct Lifetime Measurement of The Lambda Hypertriton | 永尾翔 |
| 2861 | ハイパー核直接寿命測定に向けた Λ 粒子寿命測定実験 | 永尾翔 |
| 2863 | 非標識化領域光子を用いた重水素原子核標的での $\pi^+\pi^-$ 生成反応の研究 | 神田浩樹 |
| 2864 | 新光子標識化装置 Taggers の性能評価 | 田島靖久 |
| 2865 | COMET 実験用電磁カロリメータの開発 | 東城順治 |
| 随時申込 | | |
| 2866 | PWO ビームモニターの性能評価 | 宮部学 |
| 2867 | MPPC-Array を用いたビームプロファイルモニターの開発 | 時安 敦史 |

# ELPH ANNUAL REPORT 2016

December 2017

Research Center for Electron Photon Science, Tohoku University
1-2-1, Mikamine, Taihaku, Sendai 982-0826, Japan

印刷所　株式会社　東北プリント
仙台市青葉区立町24番24号
TEL　022（263）1166㈹